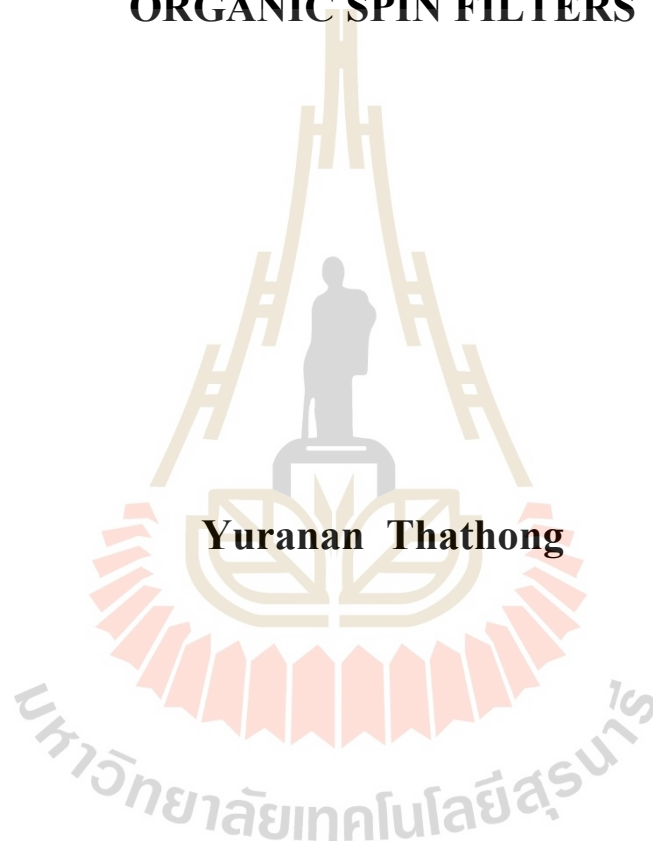


**SYNTHESIS AND CHARACTERIZATION OF NOVEL  
ORGANIC MATERIALS FOR ORGANIC  
LIGHT-EMITTING DIODES AND  
ORGANIC SPIN FILTERS**



**A Thesis Submitted in Partial Fulfillment of the Requirements for the  
Degree of Doctor of Philosophy in Chemistry  
Suranaree University of Technology  
Academic Year 2017**

การสังเคราะห์และพิสูจน์เอกลักษณ์วัสดุอินทรีย์ชนิดใหม่สำหรับใช้ในไดโอด  
เรืองแสงอินทรีย์และตัวกรองสปีนอินทรีย์



นางสาวยุระนันท์ ทาทอง

วิทยานิพนธ์นี้เป็นส่วนหนึ่งของการศึกษาตามหลักสูตรปริญญาวิทยาศาสตรดุษฎีบัณฑิต

สาขาวิชาเคมี

มหาวิทยาลัยเทคโนโลยีสุรนารี

ปีการศึกษา 2560

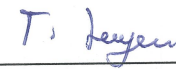
**SYNTHESIS AND CHARACTERIZATION OF NOVEL ORGANIC  
MATERIALS FOR ORGANIC LIGHT-EMITTING  
DIODES AND ORGANIC SPIN FILTERS**

Suranaree University of Technology has approved this thesis submitted in partial fulfillment of the requirements for the Degree of Doctor of Philosophy.

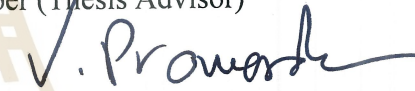
Thesis Examining Committee

  
(Prof. Dr. James R. Ketudat-Cairns)

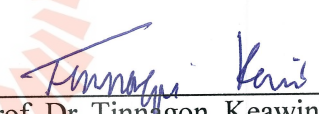
Chairperson

  
(Asst. Prof. Dr. Thanaporn Manyum)

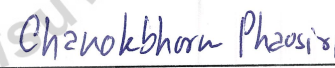
Member (Thesis Advisor)

  
(Prof. Dr. Vinich Promarak)

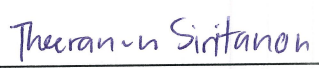
Member

  
(Asst. Prof. Dr. Tinnagon Keawin)

Member

  
(Asst. Prof. Dr. Chanokbhorn Phaosiri)

Member

  
(Asst. Prof. Dr. Theeranun Siritanon)

Member

  
(Asst. Prof. Dr. Worawat Meevasana)

  
(Prof. Dr. Santi Maensiri)

Vice Rector for Academic Affairs  
and Internationalization

Dean of Institute of Science

ยุระนันท์ ทาทอง : การสังเคราะห์และพิสูจน์เอกลักษณ์วัสดุอินทรีย์ชนิดใหม่  
สำหรับใช้ในไดโอดเรืองแสงอินทรีย์และตัวกรองสปินอินทรีย์ (SYNTHESIS AND  
CHARACTERIZATION OF NOVEL ORGANIC MATERIALS  
FOR ORGANIC LIGHT-EMITTING DIODES AND ORGANIC SPIN FILTERS)  
อาจารย์ที่ปรึกษา : ผู้ช่วยศาสตราจารย์ ดร.ธนพร แม่นยำ, 138 หน้า

ไดโอดเรืองแสงอินทรีย์ชนิดเรืองแสงฟอสฟอเรสเซนซ์ การเรืองแสงสีน้ำเงิน คาร์บาโซลเดนดรอน  
โมเลกุลไครัล

งานวิจัยนี้เป็นงานที่เกี่ยวข้องกับการสังเคราะห์และพิสูจน์เอกลักษณ์วัสดุอินทรีย์ชนิดใหม่  
จำนวน 3 ชุด ได้แก่ ชุดของสารไดโอดอินทรีย์ชนิดที่มีตัวส่งผ่านประจุในตัวเองที่เรืองแสงฟอสฟอ  
เรสเซนซ์ (PhOLED) ชุดของสารไดโอดอินทรีย์ที่เรืองแสงสีน้ำเงินของดีเลย์ฟลูออเรสเซนซ์ที่ถูก  
กระตุ้นด้วยความร้อน (TADF) และชุดของสารไครัลที่ใช้เป็นตัวกรองสปินในอุปกรณ์ด้านทาน  
สนามแม่เหล็ก

สารแต่ละตัวในชุดแรก (IrG0-IrG3) มีโครงสร้างประกอบด้วยสารเชิงซ้อนที่มีเอริเดียม  
เป็นแกนกลาง เชื่อมต่อกับคาร์บาโซลเดนดรอนด้วยตัวเชื่อมชนิดนอนคอนจูเกต เพื่อให้ได้ระบบ  
ตัวส่งผ่านประจุในตัวเองที่มีประสิทธิภาพ และใช้เทคนิคโปรตอนเอ็นเอ็มอาร์ เอพทีไออาร์ และ  
มัลติทอพเอ็มเอสในการพิสูจน์เอกลักษณ์ของสาร จากการศึกษาสมบัติเชิงแสงพบว่าสารเชิงซ้อนใน  
ชุดนี้แสดงการดูดกลืนแสงในช่วงยูวี-วิสิเบิล และแสดงการเรืองแสงที่มีความเข้มสูงสุดที่ความยาว  
คลื่น 580-590 นาโนเมตร และคาดว่าจะสามารถขึ้นรูปเป็นฟิล์มอสัณฐานบาง ๆ ที่เสถียร เนื่องจากมี  
ค่าอุณหภูมิการเกิดเกล็ดสเฟรนชันที่สูง โดยมีค่ามากกว่า 218 องศาเซลเซียส

สารในกลุ่มที่ 2 (FSG1-FSG3) มีสมบัติเป็นสารเรืองแสงสีน้ำเงินของดีเลย์ฟลูออเรสเซนซ์  
ที่ถูกกระตุ้นด้วยความร้อน (TADF) และส่งผ่านโฮลในไดโอดเรืองแสงอินทรีย์ มีโครงสร้าง  
ประกอบด้วยไดฟีนิลซัลโฟนซึ่งทำหน้าที่เป็นหมู่ดึงอิเล็กตรอน และคาร์บาโซลเดนดรอนซึ่งทำ  
หน้าที่เป็นหมู่ให้อิเล็กตรอนและตัวส่งผ่านโฮล จากการศึกษาสมบัติเชิงแสงพบว่าสารในกลุ่มนี้มี  
การเรืองแสงที่มีความเข้มสูงสุดที่ความยาวคลื่น 403-452 นาโนเมตร และจากการศึกษาสมบัติทาง  
ความร้อนพบว่า สารมีเสถียรภาพทางความร้อนเพิ่มขึ้นเมื่อเพิ่มจำนวนของคาร์บาโซลเดนโดรเมอร์

สารแต่ละตัวในกลุ่มสุดท้าย (M, P-Cis 21 และ M, P-Trans 21) ประกอบด้วยโมเลกุลไครัล  
เชื่อมต่อกับพันธะไพที่คอนจูเกตกัน สำหรับใช้เป็นตัวกรองสปินอินทรีย์ในอุปกรณ์ด้านทาน  
สนามแม่เหล็ก และใช้เทคนิคโปรตอนเอ็นเอ็มอาร์ คาร์บอนเอ็นเอ็มอาร์ และ แอลซีเอ็มเอสในการ

พิสูจน์เอกลักษณ์ของสาร นอกจากนี้ ลักษณะการบิดเป็นเกลียวของ โมเลกุล ไครัล ได้รับการยืนยัน  
จากการศึกษาด้วยเทคนิคเซอคูลาร์ไดโครอิซึม (ซีดี)



สาขาวิชาเคมี  
ปีการศึกษา 2560

ลายมือชื่อนักศึกษา Yuranan

ลายมือชื่ออาจารย์ที่ปรึกษา T. Juejue

ลายมือชื่ออาจารย์ที่ปรึกษาร่วม V. Promade

YURANAN THATHONG : SYNTHESIS AND CHARACTERIZATION  
OF NOVEL ORGANIC MATERIALS FOR ORGANIC LIGHT-EMITTING  
DIODES AND ORGANIC SPIN FILTERS. THESIS ADVISOR : ASST.  
PROF. THANAPORN MANYUM, Ph.D. 138 PP.

PHOSPHORESCENT OLEDs/ BLUE LIGHT EMITTING/ CARBAZOLE-  
DENDRON/ CHIRAL MOLECULE

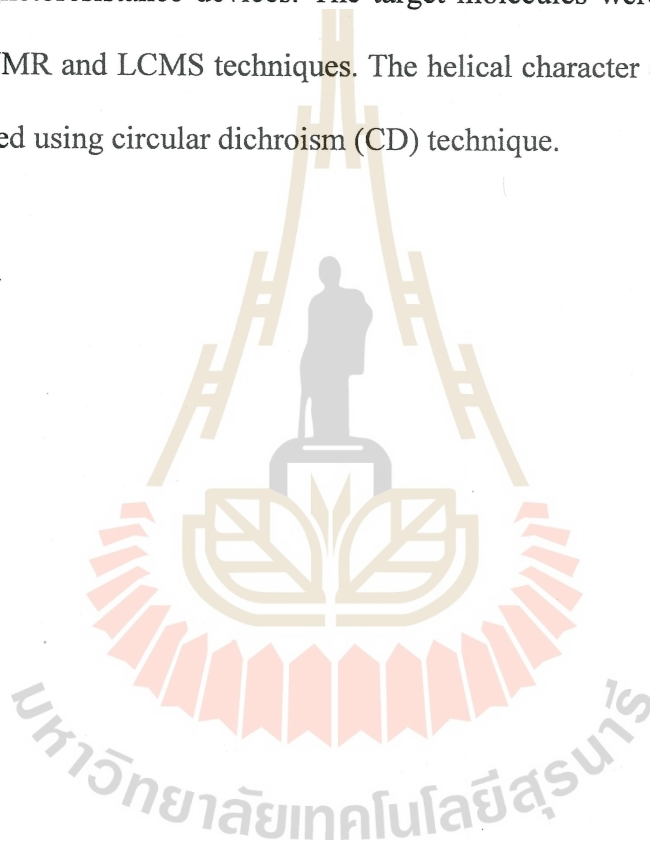
This research work involved the synthesis and characterization of the three series of novel organic materials, including self-hosting phosphorescent organic light emitting diode (PhOLED) materials, blue thermally activated delayed fluorescent (TADF) materials for organic light emitting diodes (OLEDs), and chiral molecules for using as spin filters in magnetoresistance devices.

Each of the materials in the first series (**IrG0-IrG3**) contained iridium core complexes and a non conjugated link with carbazole dendrons to form an efficient self-host system. The target complexes were characterized by <sup>1</sup>H-NMR, FTIR and MALDI-TOF MS techniques. It was found that each of the complexes displayed an absorption band in the UV-Visible region and photoluminescence with  $\lambda_{\text{max}}$  at 580-590 nm. Moreover, these compounds are expected to form stable amorphous thin films due to their high glass transition temperature of more than 218 °C.

The second series (**FSG1-FSG3**) is blue TADF emitter with hole transporting properties for OLEDs. The compounds contained diphenylsulfone as accepting blue emissive core and carbazole dendron as electron donating and hole moiety. It was found from the optical study that the compounds exhibited photoluminescence with

$\lambda_{\max}$  at 403-452 nm. Furthermore, from the thermal study, the thermal stability of the compounds was found to improve with increasing numbers of carbazole dendrimers in the molecules.

Each of the materials in the last series (*M*, *P*-Cis **21** and *M*, *P*-Trans **21**) consisted of chiral molecules with a  $\pi$ -conjugated linkage for using as an organic spin filter in magnetoresistance devices. The target molecules were characterized by  $^1\text{H}$ -NMR,  $^{13}\text{C}$ -NMR and LCMS techniques. The helical character of chiral molecule was also confirmed using circular dichroism (CD) technique.



School of Chemistry

Academic Year 2017

Student's Signature Yuranan

Advisor's Signature T. Kijpan

Co-advisor's Signature V. Pramerde

## ACKNOWLEDGEMENTS

First and foremost, I would like to deeply express my appreciation to my advisor and co-advisor, Asst. Prof. Dr. Thanaporn Manyum and Prof. Dr. Vinich Promarak for their excellent guidance and advice during conducting and writing this thesis. Without them, I would never have started and finished this thesis.

I would like to give a special thanks to Asst. Prof. Dr. Tinnagon Keawin and Asst. Prof. Dr. Chanokbhorn Phaosiri for their excellent suggestions, as well as Prof. Dr. James R. Ketudat-Cairns and Asst. Prof. Dr. Theeranun Siritanon for their constructive comments and valuable suggestion for this thesis. I am thankful to Prof. Dr. Yoshiro Yamashita for excellent guidance with organic spin filter synthesis part and also to Dr. Supawadee Namuangruk who performed quantum chemical calculation for phosphorescent and TADF molecules.

I would like to thank all Smart Organic Materials and Semiconductor Device (SMS) group members for their helpful advices. I am especially grateful to Science Achievement Scholarship of Thailand for the scholarship and Suranaree University of Technology for financial support.

Lastly, and most importantly, I feel appreciated and grateful to my family for their supporting on my education.

Yuranan Thathong

# CONTENTS

	<b>Page</b>
ABSTRACT IN THAI.....	I
ABSTRACT IN ENGLISH.....	III
ACKNOWLEDGEMENTS.....	V
CONTENTS.....	VI
LIST OF TABLES.....	X
LIST OF FIGURES.....	XI
LIST OF ABBREVIATIONS.....	XVII
<b>CHAPTER</b>	
<b>I SYNTHESIS AND CHARACTERIZATION OF SELF HOSTING IRIIDIUM COMPLEXES FOR ORGANIC LIGHT-EMITTING DIODES.....</b>	<b>1</b>
1.1 Introduction.....	1
1.1.1 Components of organic light-emitting diodes.....	4
1.1.2 Working principle of organic light emitting diode.....	7
1.1.3 Fluorescent organic emitters.....	8
1.1.4 Phosphorescent emitters.....	10
1.1.4.1 Blue phosphorescent emitters.....	12
1.1.4.2 Green phosphorescent emitters.....	13
1.1.4.3 Red phosphorescent emitters.....	14

## CONTENTS (Continued)

	<b>Page</b>
1.1.5 Host-Guest materials.....	14
1.2 Literature reviews of phosphorescent emitters.....	17
1.3 Aims of the study.....	22
1.4 Materials and methods.....	24
1.4.1 Materials.....	24
1.4.2 Characterization techniques.....	26
1.4.3 Synthesis methods.....	28
1.5 Results and discussion.....	42
1.5.1 Synthesis.....	42
1.5.2 Optical properties.....	57
1.5.3 Photoluminescence lifetime of Ir(III) complexes.....	58
1.5.4 Electrochemical properties.....	61
1.5.5 Thermal properties.....	63
1.5.6 Quantum chemical calculation.....	65
1.6 Conclusions.....	67
1.7 References.....	67
<b>II SYNTHESIS AND CHARACTERIZATION OF BLUE</b>	
<b>THERMALLY ACTIVATED DELAYED FLUORESCENT</b>	
<b>EMITTERS.....</b>	<b>74</b>
2.1 Introduction.....	74
2.1.1 Blue TADF emitters.....	75

## CONTENTS (Continued)

	<b>Page</b>
2.1.2 Green TADF emitters.....	76
2.1.3 Red TADF emitters.....	77
2.2 Literature reviews of thermally activated delayed fluorescent (TADF) emitters.....	77
2.3 Aims of the study.....	81
2.4 Materials and methods.....	83
2.4.1 Materials.....	83
2.4.2 Characterization techniques.....	84
2.4.3 Synthesis methods.....	84
2.5 Results and discussion.....	87
2.5.1 Synthesis.....	87
2.5.2 Optical properties.....	91
2.5.3 Time-resolved fluorescence decay.....	96
2.5.4 Thermal propertie.....	99
2.5.5 Electrochemical properties.....	101
2.5.6 Quantum chemical calculation.....	103
2.6 Conclusions.....	104
2.7 References.....	105
 <b>III SYNTHESIS AND CHARACTERIZATION OF A NEW CLASS OF ORGANIC SPIN FILTER FOR MAGNETO RESISTANCE DEVICES.....</b>	 <b>108</b>

**CONTENTS (Continued)**

	<b>Page</b>
3.1 Introduction.....	108
3.2 Literature reviews of organic spin filter materials.....	113
3.3 Aims of the study.....	116
3.4 Materials and methods.....	117
3.4.1 Materials.....	117
3.4.2 Characterization techniques.....	119
3.4.3 Synthesis methods.....	120
3.5 Results and discussion.....	126
3.5.1 Synthesis.....	126
3.5.2 Optical properties.....	134
3.6 Conclusions.....	134
3.7 References.....	136
CURRICULUM VITAE.....	138

## LIST OF TABLES

Table		Page
1.1	Chemicals of Chapter I.....	24
1.2	Photophysical properties and emission lifetimes of <b>IrG0-IrG3</b> .....	61
1.3	Thermal and electrochemical properties of <b>IrG0-IrG3</b> .....	65
2.1	Chemicals of Chapter II.....	84
2.2	Photophysical properties and emission lifetimes of <b>FSG1-FSG3</b> .....	99
2.3	Thermal and electrochemical properties of <b>FSG1-FSG3</b> .....	104
3.1	Chemicals of Chapter III.....	118

## LIST OF FIGURES

Figure		Page
1.1	Molecular structures of polymer and small molecule OLEDs.....	2
1.2	The structure of the single layer OLED devices.....	3
1.3	General structure of multilayer OLED devices.....	4
1.4	A simple composition of organic light emitting devices.....	4
1.5	Working principle of each layer in an OLED.....	8
1.6	Energy diagrams of fluorescent OLEDs.....	9
1.7	Molecular structure of red, green and blue fluorescent emitters.....	9
1.8	Chemical structures of Pt(II), Re(I), Os(II) and Ir(III) complexes.....	11
1.9	Chemical structures of blue phosphorescent emitters.....	13
1.10	Chemical structures of green phosphorescent emitters.....	13
1.11	Chemical structures of red phosphorescent emitters.....	14
1.12	Energy level relationships in a phosphorescent host-guest system.....	15
1.13	Molecular structures of general host materials.....	16
1.14	Molecular structures of carbazole host materials.....	17
1.15	The chemical structures of <b>Ir-7</b> as guest materials.....	17
1.16	The chemical structures of green phosphorescent emitters ( <b>G2</b> ) and <b>TPBI</b> host material.....	18
1.17	The chemical structures of <b>DCzDCN</b> and <b>4CzIPN</b> host materials.....	19

## LIST OF FIGURES (Continued)

Figure		Page
1.18	The chemical structure of the self-hosting blue phosphorescent emitter ( <b>B-G2</b> ).....	19
1.19	The chemical structure of the self-hosting green PhOLED ( <b>21NPC-G2</b> ).....	20
1.20	The chemical structure of the yellow light emitting OLEDs, ( <b>fbi</b> ) <sub>2</sub> Ir( <b>acac</b> ).....	21
1.21	The structure of the blue Ir(III) complex grafted with 3,6-carbazole- <i>alt</i> -Tetraphenylsilane.....	21
1.22	The molecular structure of the designed self-hosting Ir(III) complexes.....	23
1.23	The synthetic routes to three dendrimers <b>2</b> , <b>6</b> and <b>8</b> .....	43
1.24	The propose mechanism of Ullmann coupling reaction.....	44
1.25	The <sup>1</sup> H-NMR spectra in CDCl <sub>3</sub> of <b>2</b> and <b>6</b> .....	45
1.26	The <sup>1</sup> H-NMR spectrum in CDCl <sub>3</sub> of <b>8</b> .....	46
1.27	The synthesis and <sup>1</sup> H-NMR spectra in CDCl <sub>3</sub> of molecule <b>9</b> and <b>10</b> .....	47
1.28	The synthesis and <sup>1</sup> H-NMR spectrum in CDCl <sub>3</sub> of <b>11</b> .....	48
1.29	The synthetic route to intermediate self-hosting iridium complex ( <b>13</b> ).....	49
1.30	The propose mechanism of Suzuki cross coupling reaction of <b>12</b> .....	50
1.31	The <sup>1</sup> H-NMR in CDCl <sub>3</sub> and MALDI-TOF MS spectra of molecule <b>13</b> .....	51
1.32	The synthesis and <sup>1</sup> H-NMR spectrum in CDCl <sub>3</sub> of <b>IrG0</b> .....	52
1.33	The MALDI-TOF MS spectrum of <b>IrG0</b> .....	53
1.34	The synthesis, <sup>1</sup> H-NMR in CDCl <sub>3</sub> and MALDI-TOF MS spectra of <b>IrG1</b>	54
1.35	The synthesis, <sup>1</sup> H-NMR in CDCl <sub>3</sub> and MALDI-TOF MS spectra of <b>IrG2</b>	55

## LIST OF FIGURES (Continued)

Figure		Page
1.36	The synthesis, <sup>1</sup> H-NMR in CDCl <sub>3</sub> and MALDI-TOF MS spectra of <b>IrG3</b>	56
1.37	Absorption and PL intensity spectra of all Ir(III) complexes in CH <sub>2</sub> Cl <sub>2</sub> solution and thin film.....	58
1.38	Photoluminescence lifetimes of all self-hosting Ir(III) complexes in CH <sub>2</sub> Cl <sub>2</sub> solution (O <sub>2</sub> and O <sub>2</sub> free) and thin film.....	59
1.39	Photoluminescence lifetimes of all self-hosting Ir(III) complexes in CH <sub>2</sub> Cl <sub>2</sub> solution under O <sub>2</sub> (solid line) and O <sub>2</sub> free (dashed line).....	60
1.40	The electron energy transfer of phosphorescent compound.....	61
1.41	CV curves of the complexes <b>IrG0-IrG3</b> in CH <sub>2</sub> Cl <sub>2</sub> solution using 0.1 M Bu <sub>4</sub> NPF <sub>6</sub> at a scan rate of 50 mV/s.....	62
1.42	DSC and TGA thermograms of all complexes measured at a heating rate of 10 °C min <sup>-1</sup> under N <sub>2</sub> .....	64
1.43	HOMO (left) and LUMO (right) distributions of the <b>IrG0</b> and <b>IrG1</b> complexes by DFT B3LYP/6-31G (d) calculation.....	66
2.1	Energy diagram of a conventional organic molecule.....	75
2.2	Chemical structures of blue TADF emitters ( <b>4TCzBN</b> and <b>t4CzIPN</b> ).....	76
2.3	Chemical structures of green TADF emitters.....	76
2.4	Chemical structures of red TADF emitters.....	77
2.5	The structure of carbazole/sulfone series based on TADF emitters.....	78
2.6	The molecular structure of deep blue TADF emitters ( <b>DMOC-DPS</b> ).....	78
2.7	The molecular structures of <b>PPZ-4TPT</b> and <b>DMAC-DPS</b> TADF emitters	79

## LIST OF FIGURES (Continued)

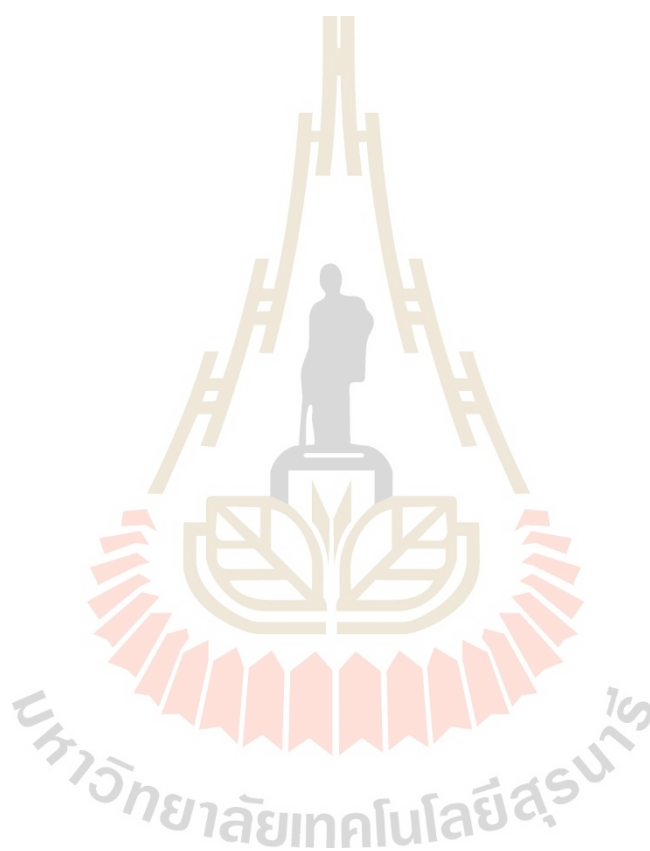
Figure		Page
2.8	The molecular structure of <b>G3F2</b> molecule.....	80
2.9	The structure of the red-light emitting dendrimers ( <b>9C</b> ).....	81
2.10	The molecular structure of non-doped blue TADF dendrimers.....	81
2.11	The designed self-hosting TADF emitters ( <b>FSG1</b> , <b>FSG2</b> and <b>FSG3</b> ).....	83
2.12	The synthesis and <sup>1</sup> H-NMR spectrum in CDCl <sub>3</sub> of <b>FSG1</b> .....	89
2.13	The synthesis and <sup>1</sup> H-NMR spectrum in CDCl <sub>3</sub> of <b>FSG2</b> .....	90
2.14	The synthesis and <sup>1</sup> H-NMR spectrum in CDCl <sub>3</sub> of <b>FSG3</b> .....	92
2.15	UV-Vis absorption and PL spectra of all TADF emitters (λ <sub>ex</sub> = 350 nm) in toluene solution and thin film.....	94
2.16	UV-Vis absorption and PL spectra of <b>FSG1-FSG3</b> in various solvents.....	95
2.17	The emission spectra of <b>FSG1-FSG3</b> in solution under O <sub>2</sub> and O <sub>2</sub> free.....	97
2.18	Time-resolved fluorescence decay of all TADF emitters in toluene solution (O <sub>2</sub> and O <sub>2</sub> free) and thin film.....	98
2.19	Time-resolved fluorescence decay of all TADF emitters in toluene solution under O <sub>2</sub> and O <sub>2</sub> free.....	99
2.20	DSC thermograms of novel blue TADF emitters measured at a heating rate of 10 °Cmin <sup>-1</sup> under N <sub>2</sub> .....	101
2.21	TGA thermograms of new blue TADF emitters measured at a heating rate of 10 °Cmin <sup>-1</sup> under N <sub>2</sub> .....	102
2.22	CV curves of the dendrimers <b>FSG1-FSG3</b> in toluene solution using 0.1 M Bu <sub>4</sub> NPF <sub>6</sub> at a scan rate of 50 mV/s.....	103

## LIST OF FIGURES (Continued)

Figure	Page
2.23	The spatial distribution of HOMO (left) and LUMO (right) energies densities of <b>FSG1-FSG3</b> by DFT B3LYP/6-31G(d) calculation..... 105
3.1	Schematic of the AMR effect: (a) <i>M</i> is transverse to <i>i</i> and (b) <i>M</i> is parallel to <i>i</i> ..... 110
3.2	Schematic illustration of the CISS effect..... 112
3.3	The determining stereochemistry in atropisomers..... 113
3.4	Schematic diagram of the organic magnetoresistance device..... 113
3.5	Chiroptical molecular switch based on the photoisomerization ( <b>P3</b> , <b>M4</b> )..... 114
3.6	<i>N</i> -Hexyl functionalized donor-acceptor target molecule <b>2.4</b> ..... 115
3.7	Molecular structure of selective switching between two atropisomers.... 115
3.8	Molecular structure of <i>P</i> - and <i>M</i> -helicenes..... 116
3.9	Donor-acceptor substituted molecular organic spin filter <b>21</b> ..... 116
3.10	The molecular designed structure of donor-acceptor motor <b>21</b> ..... 117
3.11	The conditions and reagents to synthesize molecule <b>16</b> ..... 127
3.12	<sup>1</sup> H-NMR spectrum in CDCl <sub>3</sub> of molecule <b>16</b> ..... 128
3.13	The synthesis of lower half thioketone <b>19</b> ..... 129
3.14	<sup>1</sup> H-NMR spectrum in CDCl <sub>3</sub> of molecule <b>19</b> ..... 130
3.15	Formation of the central double bond and the synthesis of <b>21</b> ..... 131
3.16	The propose mechanism of Barton-Kellogg reaction of <b>21</b> ..... 132
3.17	<sup>1</sup> H-NMR compared between Trans (top) and Cis isomer <b>21</b> (bottom)..... 133

**LIST OF FIGURES (Continued)**

<b>Figure</b>		<b>Page</b>
3.18	The HPLC spectra of Cis- and Trans-isomers <b>21</b> .....	134
3.19	CD spectra of <i>M</i> -Trans and <i>P</i> -Trans <b>21</b> in CHCl <sub>3</sub> solution.....	135



## LIST OF ABBREVIATIONS

A	Ampere
°C	Degree Celsius
Cd	Candela
CD	Circular dichroism
CIE	Commission Internationale de l'Eclairage
CISS	Chiral induced spin selectivity effect
cm <sup>-1</sup>	Wave number
<sup>13</sup> C-NMR	Carbon nuclear magnetic resonance
CV	Cyclic voltametry
CT	Charge transfer
DFT	Density functional theory
E <sub>1/2</sub>	Haft-wave potential
ΔE <sub>ST</sub>	Difference energy between singlet and triplet state
EIL	Electron injection layer
E <sub>g</sub>	Energy gap
EN	Electronegativity
EL	Electro luminescence
EML	Emissive layer
EQE	External quantum efficiency
ETL	Electron transporting layer

**LIST OF ABBREVIATIONS (Continued)**

$E_T$	Triplet energy
FTIR	Fourier transform infrared
FTO	Fluoride doped tin oxide
g	Gram
h	Hour
HIL	Hole injection layer
HOMO	Highest occupied molecular orbital
HTL	Hole transporting layer
$^1\text{H-NMR}$	Proton nuclear magnetic resonance
Hz	Hertz
ITO	Indium thin oxide
IR	Infrared
ISC	Intersystem crossing
$J$	Coupling constant (for NMR spectral data)
K	Degree kelvin
L	Liter
LCMS	Liquid chromatography mass spectrometry
lm	Luminance
LUMO	Lowest unoccupied molecular orbital
M	Molarity
m	Multiplet (for NMR spectral data)
$\text{m}^2$	Square meter

**LIST OF ABBREVIATIONS (Continued)**

MHz	Mega hertz
min	Minute
ml	Milliliter
MLCT	Metal to ligand charge transfer
mmol	Millimol
mol	Mole
m.p.	Melting point
MR	Magnetoresistance
mV	Millivolt
nm	Nanometer
ns	Nanosecond
OLED	Organic light emitting diode
Ox	Oxidation
PhOLED	Phosphorescent organic light emitting diode
PLQY	Photoluminescence quantum yield
ppm	Part per million
q	Quartet (for NMR spectral data)
Red	Reduction
RISC	Reverse intersystem crossing
s	Singlet (for NMR spectral data)
s	Second

**LIST OF ABBREVIATIONS (Continued)**

$S_0$	Singlet ground state
$S_1$	Singlet excited state
SOC	Spin orbit coupling
$T_1$	Triplet excited state
$t$	Triplet (for NMR spectral data)
$T_{5d}$	5% of decomposition temperature
TADF	Thermally activated delayed fluorescence
$T_g$	Glass transition temperature
TLC	Thin layer chromatography
TMS	Tetramethylsilane
UV-Vis	Ultraviolet-visible
W	Watt
$\delta$	Chemical shift (for NMR spectral data)
$\mu\text{m}$	Micrometer
$\mu\text{s}$	Microsecond
$\epsilon$	Molar absorptivity
$p$	Para
$\lambda$	Wavelength
$\Phi$	Work function
$\phi$	Conduction value

# CHAPTER I

## SYNTHESIS AND CHARACTERIZATION OF SELF HOSTING IRIDIUM COMPLEXES FOR ORGANIC LIGHT-EMITTING DIODES

### 1.1 Introduction

Organic light-emitting diodes (OLEDs) are light emitting diodes (LEDs) in which the emissive layers are made of organic films emitting light in response to electric current. Organic molecules are generally considered to be insulators. This general concept has been changed since the discovery of conducting polymers in 1970s by Heeger, MacDiarmid and Shirakawa. In 1987, Tang and Vanslyke at Kodak Chemical fabricated the first thin film light-emitting diode using tris(8-hydroxyquinolinolato)aluminum ( $\text{Alq}_3$ ) as the emitter sandwiched between a transparent indium tin oxide (ITO) and Al/Mg electrodes (Tang and Vanslyke, 1987). In 1990, semiconducting conjugated polymers were also found to emit green-yellow light under an electric field (Burroughes et al., 1990). Researches on organic light-emitting diodes culminated in 1998 with the work by Forrest and co-workers, who reported the discovery of OLEDs employing phosphorescent metal-organic complexes (Baldo et al., 1998). These pioneering studies have truly revolutionized our understanding of the correlation between the chemical structures and optical properties of the OLED molecules. Nowadays, the OLED molecular structures are

classified into polymer light-emitting diodes (PLEDs) and small molecule organic light-emitting diodes (SMOLEDs). **MEH-PPV** (Braun and Heeger, 1991) and **DCDDC** molecules, as shown in Figure 1.1, are examples of PLEDs and SMOLEDs, respectively, which are used as emitters in flat-panel displays.

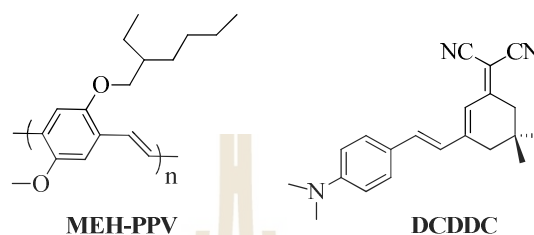


**Figure 1.1** Molecular structures of polymer and small molecule OLEDs.

OLEDs have attracted enormous attention in the scientific community due to their potential for applications in full-color flat-panel displays and large area solid state lighting. Moreover, OLEDs are considered to be the next generation of flat panel displays because of advantages, such as high brightness, high luminous efficiency, fast response time, wide viewing angle, low power consumption, light weight and easy fabrication on potentially large area in comparison to liquid crystal displays (LCDs) and plasma display panels (PDPs).

Depending on the device architecture, electroluminescent devices can be divided into single layer and multilayer OLEDs.

A single layer OLED, shown in Figure 1.2, typically consists of an organic emissive layer sandwiched between a metal cathode with a low work function (WF) (e. g. Ca, Al, Ba) and a transparent anode (e. g. indium tin oxide, ITO) (Yersin, 2004). All layers are immobilized on a transparent carrier material such as glass or a flexible polymer. A balanced charge injection or carrier mobility is usually not observed in the

simple device architecture of single layer OLEDs, because the difference in the electron and hole injection barrier between the organic emissive material and the two electrodes is very high.

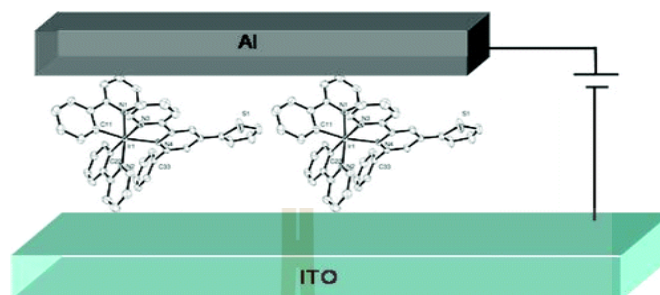


**Figure 1.2** The structure of the single layer OLED devices (Graber et al., 2008).

This problem can be overcome by the incorporation of additional layers. Multilayer OLEDs, represented in Figure 1.3, consist of multiple layers namely ITO anode, hole injection layer (HIL), hole transporting layer (HTL), emitting layer (EML), electron transport layer (ETL), electron injection layer (EIL) and metal cathode. The materials used as layers for the advanced type of OLEDs should meet the requirements of high luminescence efficiency, adequate conductivity, narrow spectra, correct Commission Internationale de l'Eclairage (CIE) coordinates, good temperature stability and also good oxidative stability to water and oxygen. Additionally, it should be mentioned that the transport layers can readily be used for increasing the efficiency of the corresponding light-emitting devices.

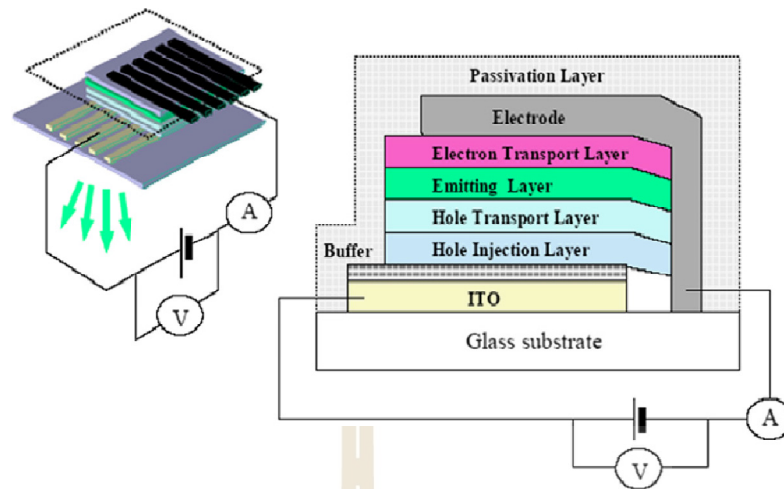


**Figure 1.3** General structure of multilayer OLED devices (Thejokalyani and Dhoble, 2014).

### 1.1.1 Components of organic light-emitting diodes

To improve the brightness and efficiency of basic multi layer devices, extra layers are often introduced (see Figure 1.4). The materials used for different layers of OLEDs are discussed in the following paragraph:

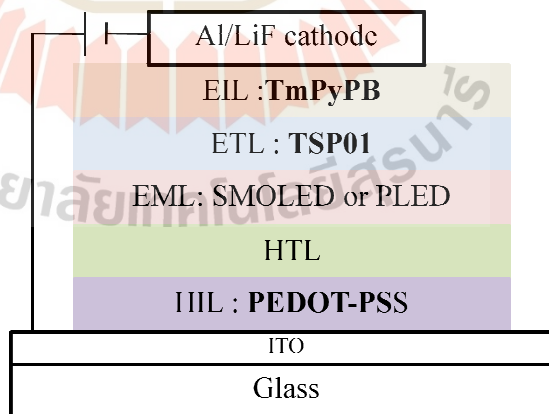


**Figure 1.4** A simple composition of organic light emitting devices (Wang et al., 2014).

1. Substrate materials: The substrate is an essential component of a light-emitting display. The substrate requirements include high transparency, low roughness with high surface area, high flatness, dimensional stability at processing temperature and high resistance against  $\text{HNO}_3$ , HF and NaOH (Wyckhoff, 1963). In general, substrate materials are glass, plastic sheet and metal foil.

2. Cathode materials: The function of this layer is to inject electrons into the emitting layers. The work function of the cathode material should be relatively small ( $\phi \approx 2.9\text{-}4.0$  eV) in order to minimize the barrier of electron injection. Moreover, this layer should have high conductivity, good film forming ability and good stability. ITO is actually the best choice as a good cathode material (Mahon et al., 1998). Other materials such as lithium, calcium and magnesium have low work functions but they are not used because of their reactive nature.

3. Electron injection layer (EIL): This layer injects electrons from the cathode to the emissive layer. The materials for this part of the optical device should have high charge mobility and high glass transition temperature.

4. Electron transport layer (ETL): This layer functions as a conducting material to help transporting electrons from the cathode into the organic emissive layer of the device. The materials need to have a lowest unoccupied molecular orbital (LUMO) energy level close to the WF of the cathode material to enable easy charge injection. In addition, they should have good electron transporting, hole blocking property, and high electron affinity together with high ionization potentials. Tris(8-hydroxyquinolinolato)aluminum (**Alq<sub>3</sub>**) (Tang and Vanslyke, 1987) and 9,10-di(2-naphthyl)anthracene (**ADN**) (Guan and Niu, 2009) are the most common ETL materials.

5. Emissive layer (EML): The materials that get most of the glory in OLED device naturally generate the light output. This layer can be a material made of organic molecules or polymer dendrimers with high optical efficiency, excellent solubility and color purity. The phosphorescence emitting layer is actually a mixture of two or more materials wherein there is at least one electroluminescent emissive material in conjugation with charge transporting host material. The EML materials should have a good emitter and high glass transition temperature to obtain a long device lifetime.

Depending on the required color, we can select organic materials based on the energy gap: the distance between highest occupied molecular orbital (HOMO) and LUMO is such that the energy released during recombination, correspond to the desired wavelength. There are many emissive materials and a few examples: bis[2-(4,6-difluorophenyl)pyridinato- $C^2,N$ ](picolato) iridium(III) (**FIrpic**) and tris[2-phenylpyridinato- $C^2,N$ ]iridium(III) (**Ir(ppy)<sub>3</sub>**) complexes as blue and green phosphor OLED, respectively.

6. Hole transport layer (HTL): The HTL materials are very common in small molecule-based OLED devices but are less common in polymer-based devices because conjugated polymers are usually good hole conductors themselves. This layer provides a hole-conductive (via charge hopping) pathway for positive charge carriers to migrate from the anode into the EML. The HTL property requirements are thermal and electrochemical stability, high charge mobility, and high glass transition temperature. The most common hole transport materials are *N,N'*-diphenyl-*N,N'*-bis(3-methylphenyl)1,1'-biphenyl-4,4' diamine (**TPD**), *N,N'*-diphenyl-*N,N'*-bis(1-

naphthylphenyl)-1,10-biphenyl-4,4'-diamine (**NPB**) (Choi et al., 2013) and 1,10-bis(di-4-tolylaminophenyl) cyclohexane (**TAPC**) (Kim et al., 2014).

7. Hole injection layer (HIL): The ability of a HIL material to improve charge injection into the OLED device has spawned a number of materials. The HIL materials have been shown to provide benefits, particularly in terms of lower operating voltage and extended lifetime of devices. The hole injection materials (HIMs), should have high mobility, good adhesion to the anode and high glass transition temperature. Porphyrinic metal complexes, self-assembled silane compounds, **PEDOT-PSS** (Kokde et al., 2004) and doped polyaniline or polypyrrole are the examples of materials used for hole injection layer.

8. Anode materials: The anode material is, most typically, transparent ITO coated onto a glass or plastic substrate. The general requirements for an anode material are as follows: high conduction in order to reduce contact resistance, high WF ( $\phi > 4.1$  eV) to promote efficient hole injection, good film-forming and wetting properties of applied organic materials and good thermal and chemical stability as well as good transparent material.

### **1.1.2 Working principle of organic light emitting diode**

1. Under action of a driving voltage, electrons are injected from the cathode into the adjacent LUMO of the EIL and ETL, respectively. The holes are also injected from the anode into the adjacent HOMO of the HIL and HTL, respectively, as shown in Figure 1.5.

2. The electrons and holes move through the organic emissive layer and recombine under the formation of an "exciton" capable of relaxing from its excited state to the ground state. An exciton is forming and depending upon the nature of the

emissive materials (EMs) and according to appropriate selection rules, singlet fluorescence or triplet phosphorescence is emitted.

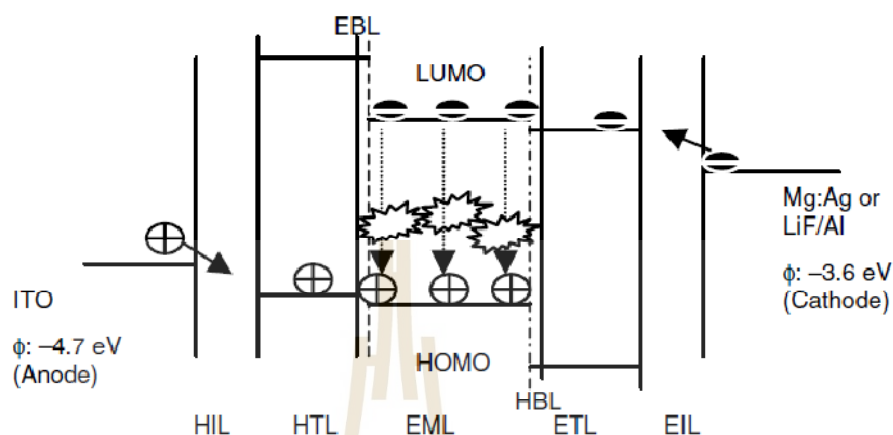


**Figure 1.5** Working principle of each layer in an OLED (Li and Meng, 2006).

For years of study, OLEDs have made many great breakthroughs, and electroluminescent materials like fluorescent emitters, phosphorescent emitters and thermally activated delayed fluorescent (TADF) emitters were developed.

### 1.1.3 Fluorescent organic emitters

Fluorescent organic emitters consist of organic materials as the main component. Donor-acceptor (D-A) structure is widely employed with the structure to improve charge injection and transport abilities for functional materials for fluorescent OLEDs. Current trends in the development of OLEDs are mainly focusing both on optimizations of device structures and on developing new emitting materials. Triarylamine, carbazole and triphenylmethane are commonly used as donor groups with the structure employed in emissive and hole transport materials. Electron withdrawing moieties like triazine, imidazole and oxadiazole as acceptors were widely used in organic emissive materials. The quantum efficiency of fluorescent material in

OLEDs is limited by theoretical ratio of singlet excitons (25%) compared to that of triplet excitons (75%) shown in Figure 1.6. Research now on novel luminescent emitter materials is identifying material emitting pure red, green and blue colors with excellent emission efficiency and stability. Research on novel luminescent materials has also played a fundamental role in developing OLEDs. Figure 1.7 shows the example of red (Chang et al., 2011), green (Wang et al., 2016) and blue (Wu et al., 2014) fluorescent emitters, respectively. All molecules have a different donor,  $\pi$  and acceptor parts corresponding to different color.

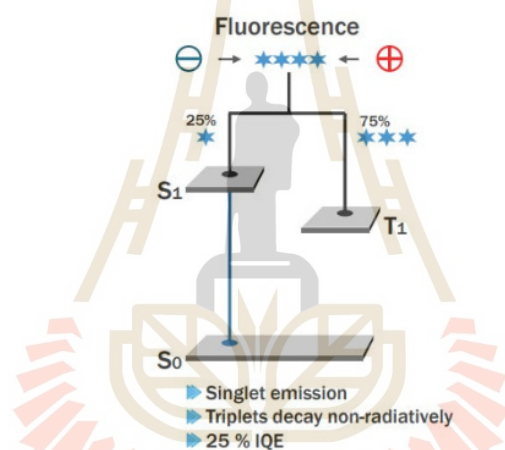


**Figure 1.6** Energy diagram of fluorescent OLEDs.

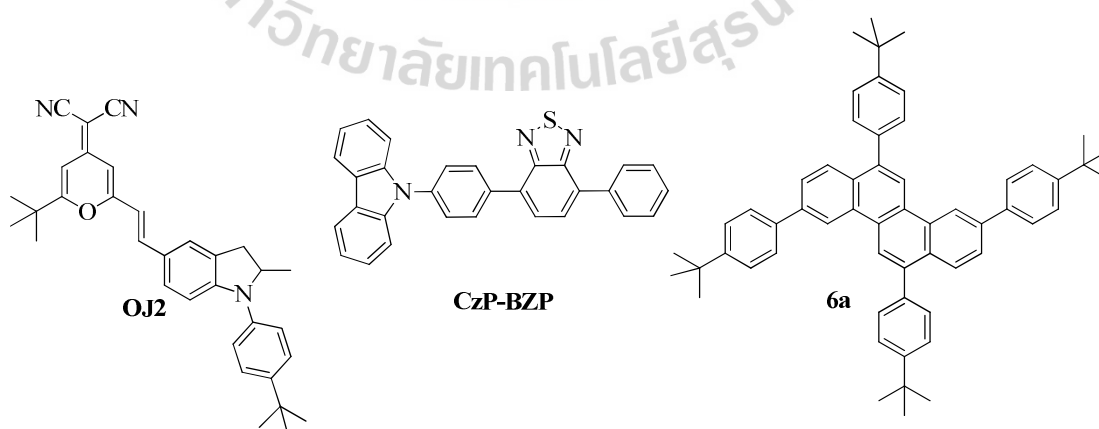


**Figure 1.7** Molecular structures of red (OJ2), green (CzP-BZP) and blue (6a) fluorescent emitters.

#### 1.1.4 Phosphorescent organic emitters

The discovery of phosphorescent organic light emitting diode (PhOLED) materials containing different transition metals, such as iridium(III), platinum(II), osmium(II), and rhenium(I) was a major breakthrough towards high performance OLEDs (Baldo et al., 1999). According to spin statistics, 75% triplet ( $T_1$ ) and 25% singlet ( $S_1$ ) excitons are formed by the recombination of a hole and an electron under electrical excitation (Waser, 2003). In conventional fluorescent organic materials, only up to 25% of the total generated excitons from singlet ( $S_1$ ) can be used for light emission.

Research on novel phosphorescent materials based on transition metal, such as Pt(II) (Steven et al., 2013), Re(I) (Li et al., 2010), Os(II) (Jiang, 2001) and Ir(III) (Chi and Chou, 2010) complexes shown in Figure 1.8, has played a key role in developing phosphorescent OLEDs. Among all of the phosphorescent OLEDs, cyclometalated iridium(III) complexes are acquiring the mainstream position in the field of organic displays because of their highly efficient emission property, relatively short excited state lifetime and excellent color tenability over the entire visible spectrum.

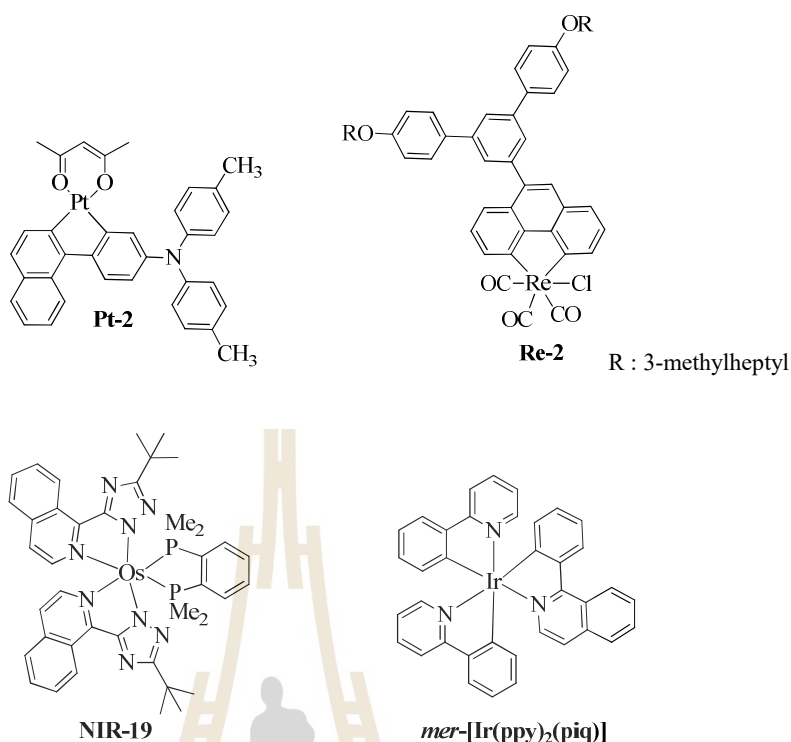


**Figure 1.8** Chemical structures of Pt(II), Re(I), Os(II) and Ir(III) complexes.

In general, to achieve high performance phosphorescent OLEDs, emitters are doped in host materials to reduce the severe concentration quenching. Recently, high performance vacuum-deposited phosphorescent OLEDs with multilayer device structures have been reported. However, the exploration of suitable phosphorescent OLEDs for non-doped PhOLEDs, which can be used alone as the emitting layer (EML) without the need to be dispersed into an additional host matrix, has become an increasingly exciting area for research (Jiang, 2010). Moreover, in order to obtain a simpler and cheaper fabricated OLED process, the non-doped phosphorescent OLEDs are also interesting compared with previous doped phosphorescent OLEDs.

Both singlet ( $S_1$ ) and triplet ( $T_1$ ) excitons can be harvested in phosphorescent organometallic material, since the strong spin-orbit coupling of the

central heavy metal can enhance the intersystem crossing (ISC). These phosphorescent OLEDs with transition metal complexes can realize nearly 100% external quantum efficiency. These transition metal complexes definitely exhibit a series of very desirable material properties such as emission wavelength covering the entire visible spectrum, high quantum yield and long lifetime. Recently, many efforts have been reported on the novel blue, green and red phosphorescent complexes described in the following section.

#### **1.1.4.1 Blue phosphorescent emitters**

In the case of blue emitters, phosphorescent materials still lag behind their fluorescent counterparts. One particular problem is finding a material with a high-enough triplet state corresponding to a blue emission wavelength. Furthermore, finding a host for this material without quenching the emissive state is a major challenge since the triplet state of the host must be higher in energy than the emitter triplet state. Figure 1.9 represents the example of blue phosphorescent emitters (Xu et al., 2014; Lo et al., 2005).

The main approaches for achieving efficient blue phosphorescence include, 1) increasing the energy gap by elevating LUMO level or lowering HOMO level, 2) introducing ancillary ligands with strong field effects and 3) shortening the effective conjugation length of molecules.

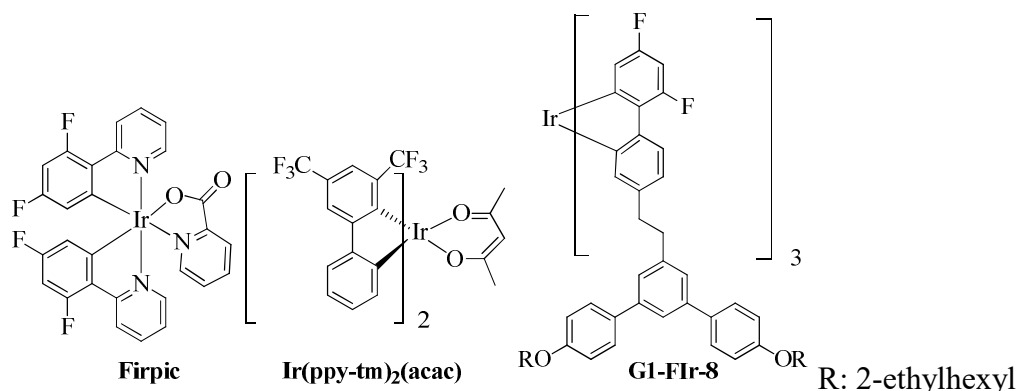


**Figure 1.9** Chemical structures of blue phosphorescent emitters.

#### 1.1.4.2 Green phosphorescent emitters

Figure 1.10 lists some iridium complexes used in green PhOLEDs (Lo et al., 2003, Wang et al., 2001). The iridium complexes containing different ligands, such as phenyl pyridine or benzoimidazole ligands have been studied. **Ir(ppy)<sub>3</sub>** is the example and original green emitter. The maximum luminescence of **Ir(ppy)<sub>3</sub>** thin films is 510 nm with full width at half maximum (FWHM) of 70 nm. The doped device of 6% **Ir(ppy)<sub>3</sub>** in a 4,4-*N,N'*-dicarbazolebiphenyl (**CBP**) as host exhibited high quantum efficiency (QE) performance (~8%); however, the neat thin film only gave ~0.8% of QE.

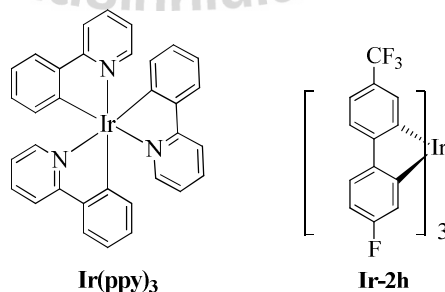


**Figure 1.10** Chemical structures of green phosphorescent emitters.

### 1.1.4.3 Red phosphorescent emitters

The research on red phosphorescence based on Ir(III) complexes has drawn increasing attention due to their high device efficiency. Red emitting Ir(III) complexes often suffer from unbalanced carrier injection and transportation leading to luminescence quenching process. Introduction of electron-donating groups can effectively enhance the carrier injecting/transporting ability. There are examples of red phosphorescent emitters, such as complex **Ir-10** with external quantum efficiency (EQE) of 11.76%, complex **Ir-45** of 3% and complex **5a** of 3.8% (Bae et al., 2014). There are depicted in Figure 1.11.

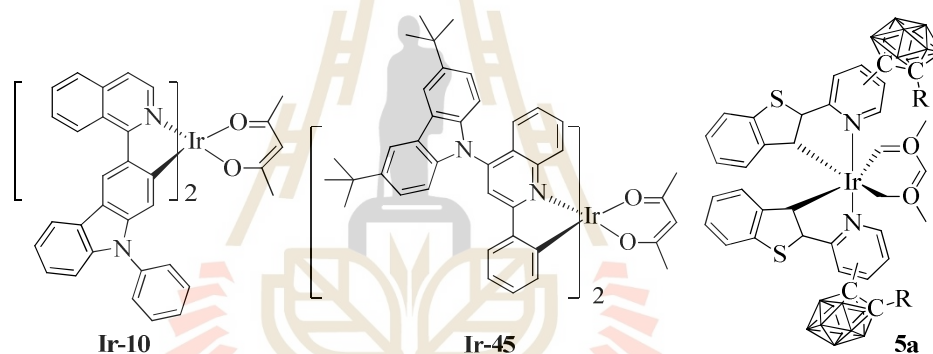


**Figure 1.11** Chemical structures of red phosphorescent emitters (Ho et al., 2014).

### 1.1.5 Host-Guest materials

For the fabrication of efficient phosphorescent OLEDs, transition metal complexes are typically used as emitting guests in the host material to avoid quenching effects associated with the relatively long excited state lifetime. Thus, the synthesis and characterization of adequate host materials are significantly important and provide big opportunities for OLED chemists (Wang et al., 2001). The technique has been widely utilized to optimize the efficiencies of OLED devices. This applies to

both singlet excited states and triplet excited states of the host and the guest as shown in Figure 1.12(c).

The basic property requirements for the host materials are as follows:

1. Good electron and hole conduction with thermal, chemical, and electrochemical stabilities
2. Matching HOMO and LUMO energy levels with the guest materials. For efficient energy transfer processes, the LUMO energy level of the host normally should be shallower than the corresponding LUMO energy level of the guest. Likewise, the HOMO energy level of the host should be deeper than that of the guest as shown in Figure 1.12(a).
3. The triplet level of the host is higher than the triplet level of the phosphorescent guest for preventing undesired energy back transfer processes.
4. Phase compatibility with the guest materials.

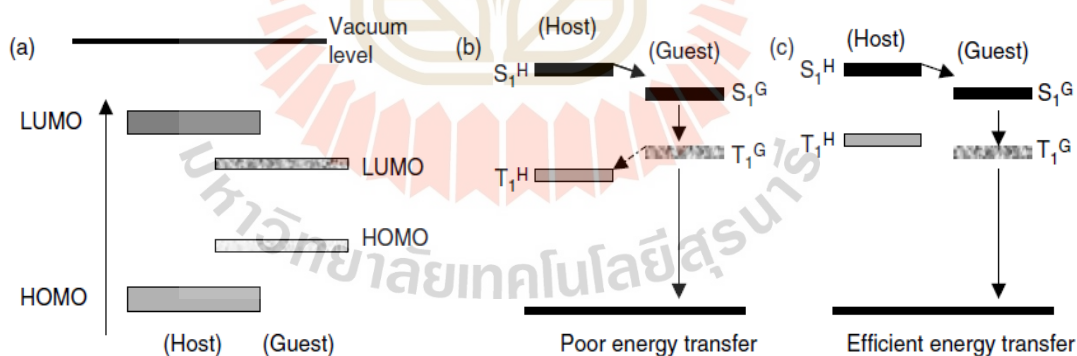


**Figure 1.12** Energy level relationships in a phosphorescent host-guest system (Li and Meng, 2006).

The selection of host materials is great importance for the preparation of efficient PhOLEDs. For example, in a blue PhOLEDs, designing materials has been rare because the triplet energy ( $E_T$ ) of the host material must be higher than that of the

blue emitter (e.g.  $\geq 2.7$  eV for **FIrpic** complex). Many achievements have been reported in this field in recent years and they may be classified into several categories according to the chemical structure, e.g. aryl silanes, phosphine oxides, polymers and carbazoles. There are general host materials used in many research groups, including **UGH2** as aryl silane, **DBF** as phosphine oxide, **PVK** as polymer and **CDBP** as carbazole derivatives (see Figure 1.13).

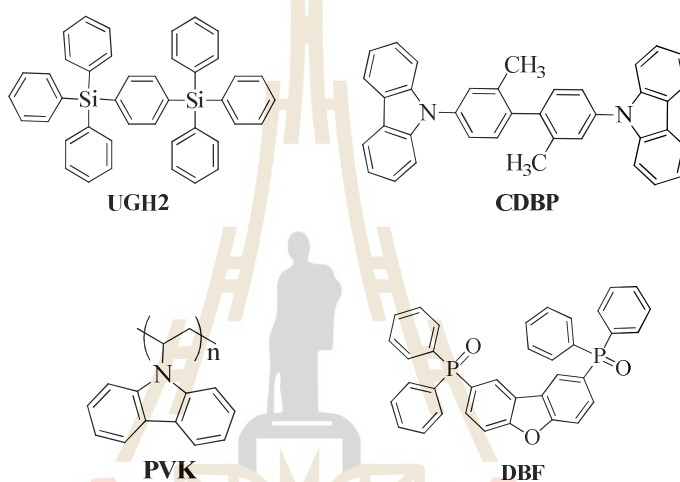


**Figure 1.13** Molecular structures of general host materials (Xiao et al., 2011).

It is well known that carbazole-based compounds are high hole mobility materials with tunable triplet energy levels and they have been widely used as the host materials of phosphorescent metal complexes for the OLEDs. Carbazole derivatives, such as 4,4-*N,N'*-dicarbazolebiphenyl (**CBP**) (Adachi et al., 2011) and 1,3-bis(9-carbazoyl)benzene (**mCP**) (Kawamura et al., 2005) presented in Figure 1.14, have been widely used as host materials in blue PhOLEDs due to their highly efficient hole transport ability.

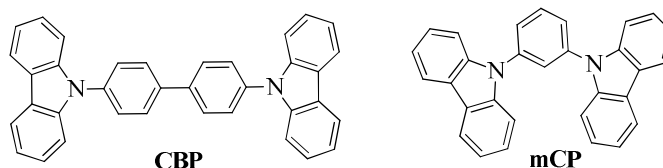


**Figure 1.14** Molecular structures of carbazole host materials.

## 1.2 Literature reviews of phosphorescent emitters

Theoretically, the internal quantum efficiency of phosphorescent OLEDs can approach 100% because of the contributions of both singlet and triplet excitons. Several excellent reviews on electrophosphorescent complexes and devices have appeared during the past few years. Herein, we highlight recent advances in the development of high performance OLEDs using phosphorescent complexes for multicolor displays and white light generation over a wide range of wavelengths.

LO and co-workers (2006) reported the synthesis of iridium cored dendrimers with carbazole dendrons, named **Ir-7** depicted in Figure 1.15. The photoluminescence quantum yields (PLQY) of thin films of the **Ir-7** dendrimers with **CBP** as host material were  $48 \pm 5\%$ .

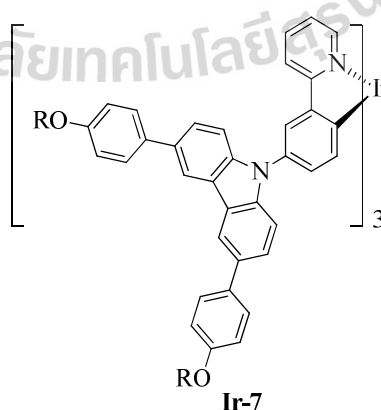


**Figure 1.15** The chemical structure of **Ir-7** as guest materials.

Ding and co-workers (2006) introduced green emitting phosphorescent iridium(III) dendrimers (**G2**) using phenyl imidazole with rigid hole transporting carbazole dendrons as ligand depicted in Figure 1.16. They found the PLQY up to 87% in solution and 45% in a film. The device structure was fabricated of ITO/poly(3,4-ethylenedioxythiophene): poly(styrenesulfonic acid)/**G2**-guest/TPBI-host/LiF/Al. Maximum EQE of 10.3% and a maximum luminous efficiency of 34.7  $\text{cdA}^{-1}$  were realized.

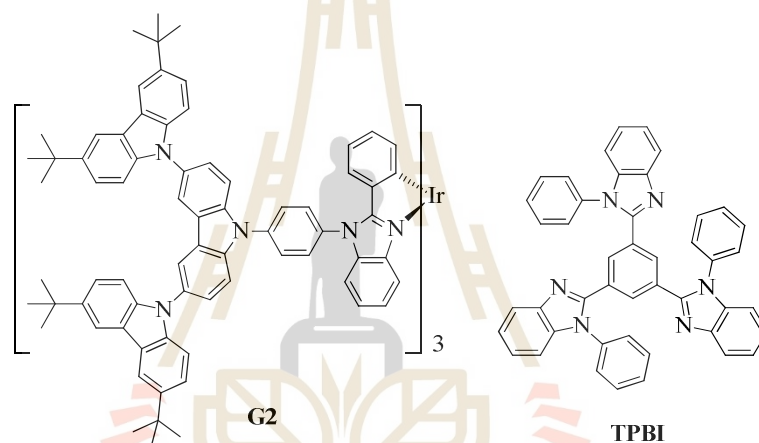


**Figure 1.16** The chemical structures of green phosphorescent emitter (**G2**) and TPBI host material.

Cho and co-workers (2014) reported **DCzDCN** host material as shown in Figure 1.17 for high EQE close to 25% and long lifetime in green fluorescent and phosphorescent OLEDs. The **DCzDCN** host showed narrow band gap, proper HOMO/LUMO levels and singlet energy of 2.98 eV and triplet energy of 2.71 eV for efficient energy transfer to **Ir(ppy)<sub>3</sub>** as phosphorescent OLEDs and **4CzIPN** as fluorescent OLEDs.

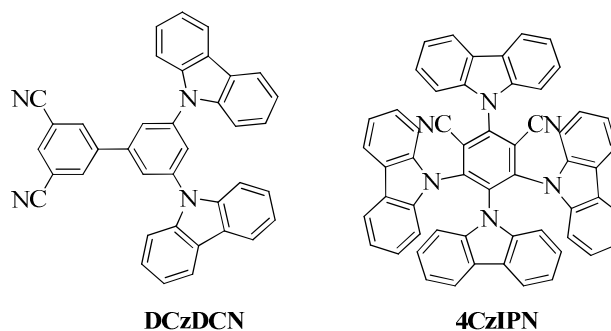


**Figure 1.17** The chemical structures of **DCzDCN** and **4CzIPN** host materials.

Xia and co-workers (2014) reported novel self-hosting blue emitting iridium dendrimers with carbazole dendrons (**B-G2**) as depicted in Figure 1.18. **B-G2** showed continuous enhancement in the device efficiency with increasing concentration. When the neat **B-G2** was used as the emitting layer, a nondoped device was achieved without loss in efficiency, thus giving an EQE as high as 15.3% ( $31.3 \text{ cdA}^{-1}$  or  $28.9 \text{ lmW}^{-1}$ ) along with CIE coordinates of (0.16, 0.29).

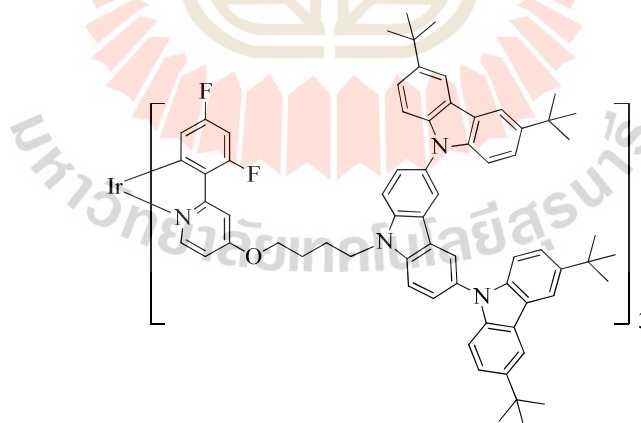


**Figure 1.18** The chemical structure of self-hosting blue phosphorescent emitters (**B-G2**).

Wang and co-workers (2015) reported self-hosting functional Ir(III)-cored dendrimers up to four generations on the basis of a newly developed polyether dendron and used *N*-phenylcarbazole (NPC) moiety as the basic building block. The performance of non-doped PhOLEDs is found to be greatly dependent on the molecular size. **9NPC-G2** (radius ( $R$ )  $\approx 30$  Å) as shown in Figure 1.19 reveals the best luminous efficiency as high as  $50.5 \text{ cdA}^{-1}$  ( $56.6 \text{ lm W}^{-1}$  or 14.8%). The results suggest that an appropriate size of  $6 \pm 2$  nm is desirable to balance the dilemma between luminescence quenching and charge transport with non-doped PhOLEDs.

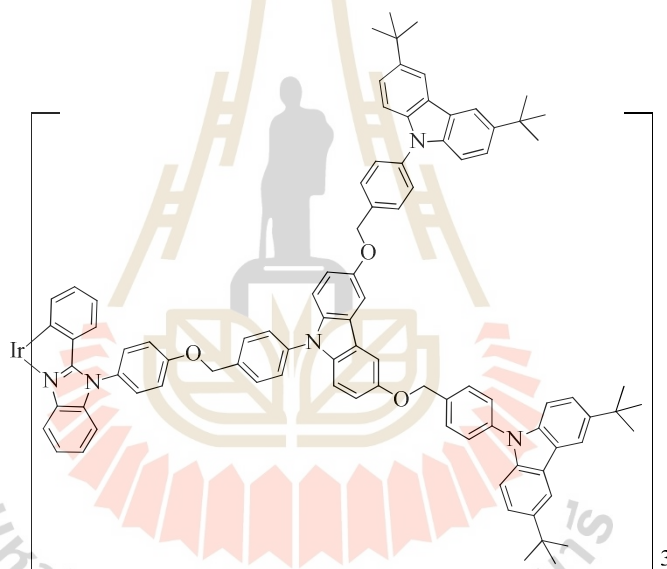


**Figure 1.19** The chemical structure of self-hosting green PhOLED (**9NPC-G2**).

Cui and co-workers (2015) reported a yellow emitting Ir(III) complex (see in Figure 1.20) by designing double light-emitting layer devices. Compared with single-EML devices, these designed double-EML devices showed improved EL efficiency and brightness attributed to better balance in carriers. In addition, they found that the yellow EL device had CIE coordinate of (0.446, 0.542) with maximum current

efficiency, power efficiency and brightness up to 78.62 cd/A, 82.28 lm/W and 72,713 cd/m<sup>2</sup>, respectively, and also showed EQE of 21.1%.

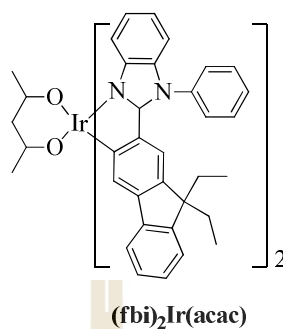


**Figure 1.20** The chemical structure of the yellow light emitting OLED.

Fei and co-workers (2010) designed a 3,6-dibromo-9-hexyl-carbazole derivative with blue emissive iridium complex grafted onto the polymer side chains (see in Figure 1.21). They demonstrated an efficient energy transfer from polymeric host to covalently bonded guest. The luminous efficiency of preliminary devices reached 2.3 cd/A and the efficiency roll-off at high current densities was suppressed.

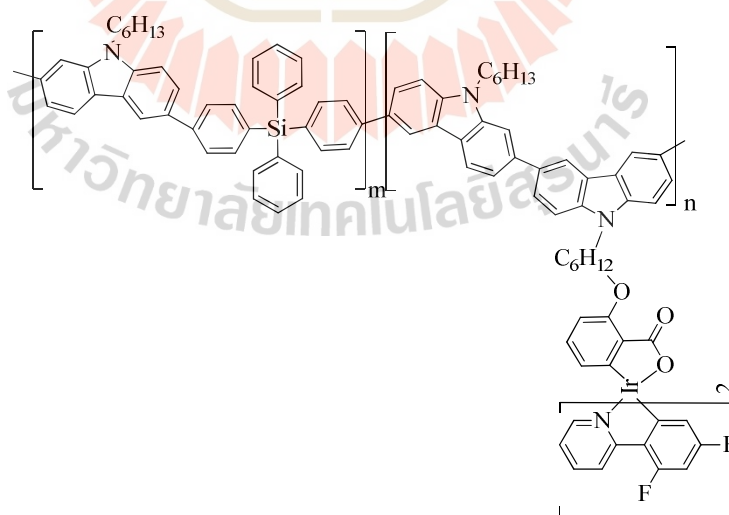


**Figure 1.21** The structure of the blue Ir(III) complex grafted with 3,6-carbazole-*alt*-tetraphenylsilane.

Based on the literature information, referent iridium complexes are prepared in different methods by many researchers. However, in most device fabrication processes iridium complexes (guests) should be mixed with different host materials in various ratios to inhibit self-quenching and confine the energy on the guest molecules. In this work, we focus on the synthesis of novel iridium-core complexes based on phenyl pyridine as cyclometalated ligand, and picolinic acid with a non conjugated linkage with carbazole dendrimers (**2**, **6** and **8**) as the end cap to obtain the desired self-hosting iridium complexes. In addition, the use of self-hosting iridium complexes is more convenient, simpler and cheaper for the device fabrication.

In this work, we aim to further improve the performance of the well known light-emitting Ir(III) complexes by designing their structures as self-hosting phosphorescent emitters. With this strategy, an efficient self-hosting system of four dendritic molecules (**IrG0-IrG3**) was designed, in which the carbazole dendrons were expected to function as the host for the iridium emissive core.

### 1.3 Aims of the study

Due to high molar extinction coefficients of the carbazole, our target phosphorescent emitters for OLEDs have been designed to contain different numbers of carbazole dendrons as self-hosting materials to increase device performance. The objectives of this chapter are the following:

1. To synthesize self-hosting Ir(III) complexes containing carbazole dendrons up to three generations. The Ir(III) core complexes are served as electron acceptors and the carbazole dendrons as donors with self-hosting property (see in Figure 1.22).

2. To characterize the synthesized target complexes by NMR, FTIR and MALDI-TOF MS techniques.

3. To study the effect of the number of carbazole dendritic generation on the physical and electrochemical as well as optical properties of these novel self-hosting phosphorescent emitters.

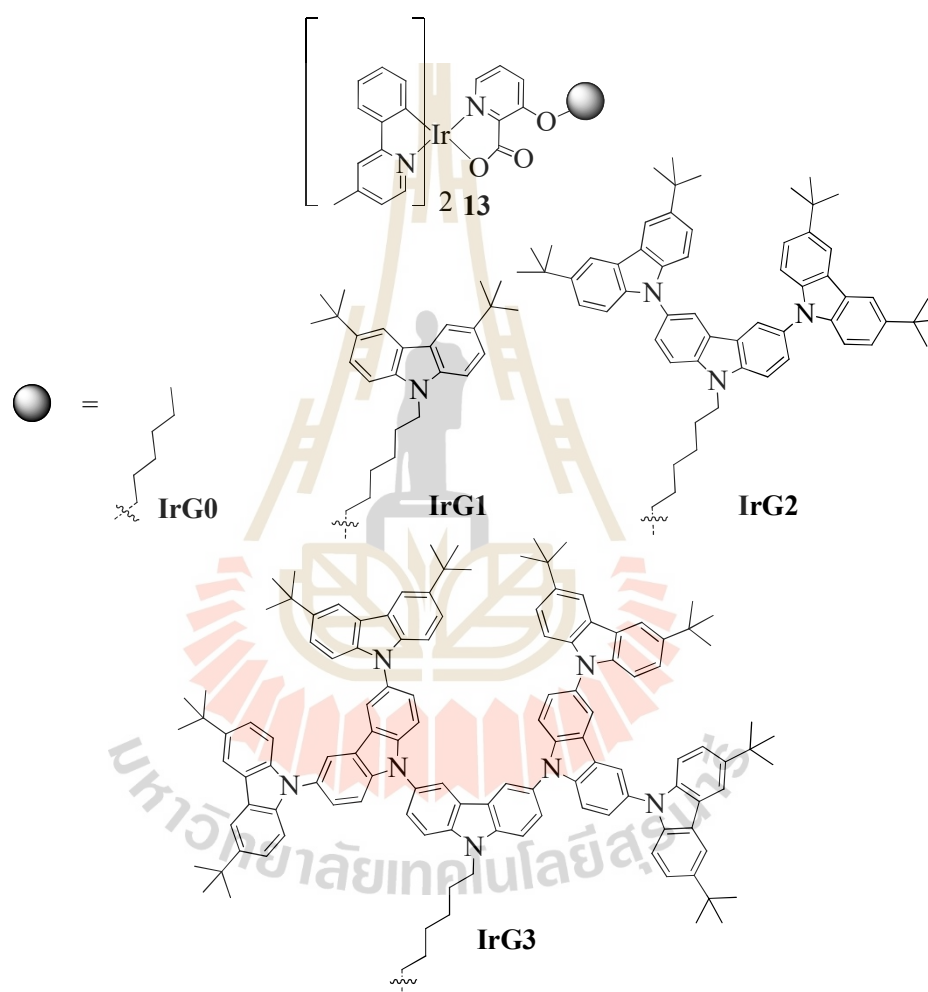


**Figure 1.22** The molecular structures of the designed self-hosting Ir(III) complexes.

#### 1.4 Materials and methods

All reactions were performed under a nitrogen atmosphere and no special precautions were required during workup. All solvents were carefully dried and

distilled from appropriate drying agents prior to use. Commercially available reagents were used without further purification unless otherwise stated. All reactions were monitored by thin-layer chromatography (TLC) with Silicycle pre-coated aluminum plates. Flash column chromatography of all compounds was carried out using silica gel (230-400 mesh) as stationary phase and commercial organic solvents as eluent.

### 1.4.1 Materials

All the chemicals used in this thesis were analytical grade as shown in

Table 1.1

**Table 1.1** Chemicals of Chapter I.

Chemicals	Formula	Grade	Manufacturer
Acetone	C <sub>3</sub> H <sub>6</sub> O	99.5%	B&J
Acetic acid	C <sub>2</sub> H <sub>4</sub> O <sub>2</sub>	ACS-for analysis	CARLO ERBA
Acetonitrile	C <sub>2</sub> H <sub>3</sub> N	99.5%	CARLO ERBA
1-Bromohexane	C <sub>6</sub> H <sub>13</sub> Br	99%	Acros
2-Bromo-4-methylpyridine	C <sub>6</sub> H <sub>6</sub> BrN	99%	Acros
Carbazole	C <sub>12</sub> H <sub>9</sub> N	96%	Acros
Chloroform	CHCl <sub>3</sub>	99%	CARLO ERBA
2-Chloro-2-methylpropane	C <sub>4</sub> H <sub>9</sub> Cl	99%	Acros
18-Crown-6	C <sub>12</sub> H <sub>24</sub> O <sub>6</sub>	99%	Acros
Copper(I) iodide	CuI	98%	Acros organics
1,6-Dibromohexane	C <sub>6</sub> H <sub>12</sub> Br <sub>2</sub>	97%	TCI
Dichloromethane	CH <sub>2</sub> Cl <sub>2</sub>	99.9%	CARLO ERBA
Dimethylformamide	C <sub>3</sub> H <sub>7</sub> NO	99.9%	CARLO ERBA
Dimethylsulfoxide	C <sub>2</sub> H <sub>6</sub> OS	99.9%	CARLO ERBA

**Table 1.1** Chemicals of Chapter I (Continued).

Chemicals	Formula	Grade	Manufacturer
2-Ethoxyethanol	C <sub>4</sub> H <sub>10</sub> O <sub>2</sub>	for analysis	CARLO ERBA
Hydrochloric acid	HCl	37%, for analysis	CARLO ERBA
3-Hydroxypicolinic acid	C <sub>6</sub> H <sub>5</sub> NO <sub>3</sub>	98%	Acros
Iridium trichloride trihydrate	IrCl <sub>3</sub> .3H <sub>2</sub> O	53-56% Ir	Pressure Chemical Co.
Magnesium sulfate	MgSO <sub>4</sub>	99%	Fluka
Methyl alcohol	CH <sub>4</sub> O	99.9%	CARLO ERBA
Potassium carbonate	K <sub>2</sub> CO <sub>3</sub>	99%	CARLO ERBA
Potassium iodate	KIO <sub>3</sub>	99%	Acros organics
Potassium iodide	KI	ACS-for analysis	Acros organics
Potassium hydroxide	KOH	99.99%	Aldrich
Potassium phosphate	K <sub>3</sub> PO <sub>4</sub>	97%	Acros organics anh.
Sodium carbonate	Na <sub>2</sub> CO <sub>3</sub>	99.5%	CARLO ERBA
Sodium sulfate	Na <sub>2</sub> SO <sub>4</sub>	99%	CARLO ERBA
Tetrahydrofuran	C <sub>4</sub> H <sub>8</sub> O	99.5%	CARLO ERBA
Tetrakis(triphenylphosphine) palladium(0)	Pd(PPh <sub>3</sub> ) <sub>4</sub>	97%	TCI
Toluene	C <sub>7</sub> H <sub>8</sub>	ISO for analysis	CARLO ERBA
<i>p</i> -Toluenesulfonyl chloride	C <sub>7</sub> H <sub>7</sub> ClO <sub>2</sub> S	99%	TCI
Zinc chloride	ZnCl <sub>2</sub>	96%	CARLO ERBA
<i>Trans</i> -1,2-diaminocyclohexane	C <sub>6</sub> H <sub>14</sub> N <sub>2</sub>	97%	TCI

### 1.4.2 Characterization techniques

The structures of intermediate and the target Ir(III) phosphorescent emitters were characterized by  $^1\text{H-NMR}$ ,  $^{13}\text{C-NMR}$ , MALDI-TOF, melting point and FTIR techniques. The optical and electrical properties of all self-hosting iridium(III) complexes were characterized by UV-Visible spectroscopy, fluorescence spectroscopy, and cyclic voltammetry, respectively. The details of the methods are the following.

1. Nuclear magnetic resonance (NMR);  $^1\text{H-NMR}$  and  $^{13}\text{C-NMR}$  spectra were performed in  $\text{CDCl}_3$  and recorded on Bruker AVANCE 600 MHz spectrometer using TMS (0.00 ppm) as the internal reference. Data for NMR spectra are reported in the order of chemical shift ( $\delta$  ppm), multiplicity, coupling constant ( $J$ ) and integration (Hz).

2. Fourier Transform Infrared (FTIR) Spectroscopy; infrared (IR) spectra were recorded on a Perkin-Elmer Spectrum Fourier transform infrared spectrophotometer over the  $4000\text{-}400\text{ cm}^{-1}$ . Data for FTIR spectra are reported as frequency ( $\text{cm}^{-1}$ ).

3. UV-Visible (UV-Vis) spectroscopy; UV-Visible spectra were measured in a 1 cm path length quartz cell using a Perkin-Elmer UV-Vis spectrometer, Lambda 1050. The samples were dissolved in dried organic solvents and diluted to an optimize concentration.

4. Cyclic voltammetry (CV); cyclic voltammetry was conducted on a Autolab potentiostat NOVA metrohm. The solution complexes were prepared in dried organic solvents containing 0.1 M tetrabutylammonium hexafluorophosphate ( $[\text{n-Bu}_4\text{N}]\text{PF}_6$ ) as supporting electrolyte at room temperature. The working electrode was

a glassy carbon electrode, the auxiliary electrode was a Pt disk electrode, and Ag/Ag<sup>+</sup> electrode was used as reference electrode.

5. Melting point (m.p.); melting points were measured on KRÜSS melting point meter in open capillary method and reported in degree Celsius.

6. Mass spectroscopy; MALDI-TOF mass spectra of all target products were recorded on microflex, Bruker using  $\alpha$ -cyano-4-hydroxycinnamic acid (HCCA) as a matrix. LCMS mass spectra were collected on mass spectrometry LC 908 using dried organic solvents.

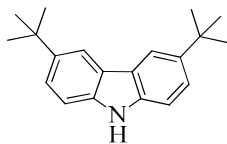
7. Differential scanning calorimetry (DSC) and thermo gravimetric analyses (TGA); the thermal properties of all molecules were investigated using differential scanning calorimetry (DSC) and thermo gravimetric analyses (TGA) on a Thermo plus TG 8120 with an optimized heating rate under a nitrogen atmosphere.

8. Fluorescence spectroscopy; photoluminescence of all target compounds were recorded with Edinburgh instrument spectroscopy in a 1.0 cm quartz cell with dried organic solution of optimized concentration and a thin film. Data for PL spectra are reported as wavelength (nm).

9. Quantum chemical calculation; the HOMO and LUMO distributions of phosphorescence and TADF emitters were calculated by DFT B3LYP/6-31G (d).

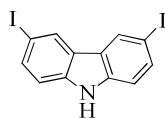
### 1.4.3 Synthesis methods

#### 3,6-Di-*tert*-butyl-9H-carbazole (**2**)



The mixture of carbazole **1** (10.07 g, 59.82 mmol), 80 ml of nitromethane and ZnCl<sub>2</sub> (24.45 g, 179.40 mmol) in 250 ml round bottom flask was sonicated for 10 min. 2-Chloro-2-methylpropane (20.00 ml, 179.40 mmol) was slowly added into the reaction. Then the reaction mixture was sonicated for 1 h and allowed to cool at room temperature. The reaction mixture was filtered under vacuum. The white corrected solid was obtained after washing with 4:1 (v/v) hexane-methanol and recrystallized with dichloromethane-hexane (11.52 g, 70%); m.p. 228-229 °C; <sup>1</sup>H-NMR (600 MHz, CDCl<sub>3</sub>): δ 8.07 (s, 2H), 7.83 (s, 1H), 7.46 (d, *J* = 1.9 Hz, 2H), 7.32 (d, *J* = 8.5 Hz, 2H), 1.45 (s, 18H) ppm; <sup>13</sup>C-NMR (151 MHz, CDCl<sub>3</sub>): δ 142.26, 138.06, 123.52, 123.36, 116.18, 110.00, 34.70, 32.04 ppm; FTIR 3413, 3052, 2954, 2864, 1470, 1362, 1300, 1099 cm<sup>-1</sup>; MALDI-TOF (m/z) [M<sup>+</sup>] calcd for C<sub>20</sub>H<sub>25</sub>N: 279.1987, found: 279.3134.

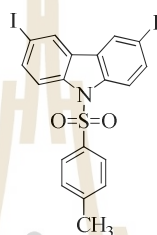
#### 3,6-Diiodo-9H-carbazole (**3**)



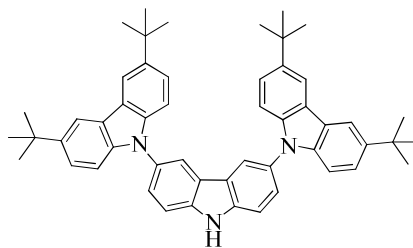
Carbazole **1** (10.08 g, 60.30 mmol) was dissolved with 80 ml conc. acetic acid. KI (13.01 g, 78.41 mmol) and KIO<sub>3</sub> (12.90 g, 60.30 mmol) were then added in the reaction. The mixture was stirred at 80 °C for 4 h. After cooling to room temperature, the precipitate was filtered by vacuum and then washed with hexane-

methanol to obtain brown solid compound (19.41 g, 77%); m.p. 203-205 °C;  $^1\text{H-NMR}$  (600 MHz,  $\text{CDCl}_3$ ):  $\delta$  8.33 (s, 2H), 7.69-7.62 (m, 2H), 7.21 (d,  $J = 8.5$  Hz, 2H) ppm;  $^{13}\text{C-NMR}$  (151 MHz,  $\text{CDCl}_3$ ):  $\delta$  138.52, 134.83, 129.39, 124.59, 112.70, 82.48 ppm; FTIR 3413, 1870, 1739, 1593, 1464, 1425, 1280, 1241, 1128  $\text{cm}^{-1}$ ; MALDI-TOF (m/z) [ $\text{M}^+$ ] calcd for  $\text{C}_{12}\text{H}_7\text{I}_2\text{N}$ : 418.8668, found: 418.9840.

#### 3,6-Diiodo-9-tosyl carbazole (**4**)



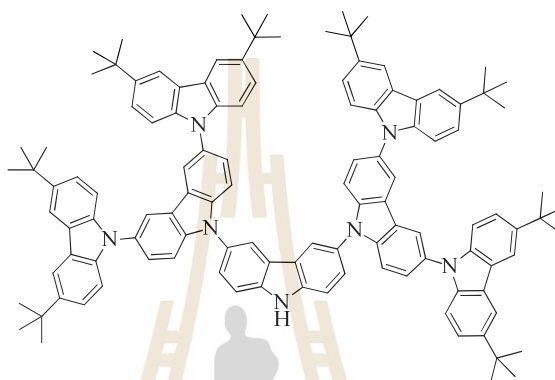
To a mixture of **3** (15.02 g, 35.79 mmol), *p*-toluene sulfonyl chloride (20.47 g, 107.39 mmol) and KOH (6.02 g, 107.39 mmol) in acetone 50 ml was refluxed for 5 h. The precipitate was filtered using vacuum and then washed with hexane and diluted HCl. The crude product was recrystallized by dichloromethane-methanol to obtain white solid (15.80 g, 95%); m.p. 259-260 °C;  $^1\text{H-NMR}$  (600 MHz,  $\text{CDCl}_3$ ):  $\delta$  8.17 (d,  $J = 1.6$  Hz, 2H), 8.07 (d,  $J = 8.8$  Hz, 2H), 7.78 (dd,  $J = 8.8, 1.6$  Hz, 2H), 7.64 (d,  $J = 8.4$  Hz, 2H), 7.13 (d,  $J = 8.4$  Hz, 2H), 2.17 (s, 3H) ppm;  $^{13}\text{C-NMR}$  (151 MHz,  $\text{CDCl}_3$ )  $\delta$  145.47, 137.85, 136.55, 134.49, 129.89, 129.17, 127.19, 126.47, 116.99, 87.94, 21.54 ppm; FTIR 1595, 1465, 1423, 1365, 1167, 1020  $\text{cm}^{-1}$ ; MALDI-TOF (m/z) [ $\text{M}^+$ ] calcd for  $\text{C}_{19}\text{H}_{13}\text{I}_2\text{NO}_2\text{S}$ : 573.8790, found: 573.0573.

3,3'',6,6''-Tetra-*tert*-butyl-9,3':6',9''-terbenzoindole (**6**)

A mixture of **4** (2.05 g, 3.48 mmol), **2** (2.24 g, 8.03 mmol), CuI (0.66 g, 3.48 mmol), K<sub>3</sub>PO<sub>4</sub> (3.70 g, 17.4 mmol) in 60 ml toluene was degassed with N<sub>2</sub> for 3 times. *Trans*-1,2-diaminocyclohexane (0.42 ml, 3.48 mmol) was added in to the reaction mixture and then stirred at reflux under N<sub>2</sub> atmosphere for 2 days. After cooling at room temperature, the reaction was extracted with CH<sub>2</sub>Cl<sub>2</sub> (20 ml × 3). The combine organic phase was washed with H<sub>2</sub>O (50 ml) and brine solution (50 ml), dried over anhydrous Na<sub>2</sub>SO<sub>4</sub>. The organic phase was concentrated under vacuum. The crude product was recrystallized with dichloromethane-methanol. The resulting product **5** (5.60 g, 6.42 mmol) was dissolved with 30 ml of 2:1 THF-DMSO mixture, 1 ml H<sub>2</sub>O and then added KOH (0.72 g, 12.80 mmol). The reaction was heated at 65 °C for 1 h. After cooling at room temperature, the reaction was extracted with CH<sub>2</sub>Cl<sub>2</sub> (20 ml × 3). The combine organic phase was washed with H<sub>2</sub>O (50 ml) and brine solution (50 ml), dried over anhydrous Na<sub>2</sub>SO<sub>4</sub>. The organic phase was concentrated under vacuum. The crude product was purified by column chromatography over silica gel eluting with a mixture of dichloromethane-hexane to obtain white solid compound (3.76 g, overall yield 65%); m.p. 233-235 °C; <sup>1</sup>H-NMR (600 MHz, CDCl<sub>3</sub>): δ 8.41 (s, 1H), 8.16 (s, 2H), 8.15 (s, 4H), 7.67 (d, *J* = 8.4 Hz, 2H), 7.61 (d, *J* = 1.8 Hz, 2H), 7.44 (dd, *J* = 8.4, 1.8 Hz, 4H), 7.31 (d, *J* = 8.4 Hz, 4H), 1.46 (s, 36H) ppm; <sup>13</sup>C-NMR (151 MHz, CDCl<sub>3</sub>): δ 142.52, 140.22, 139.04, 130.50,

125.98, 124.13, 123.54, 123.09, 119.43, 116.18, 111.85, 109.11, 34.73, 32.05 ppm;  
 FTIR 3415, 3047, 2959, 2864, 1578, 1490, 1292, 1262, 1034  $\text{cm}^{-1}$ ; MALDI-TOF  
 (m/z) [ $\text{M}^+$ ] calcd for  $\text{C}_{52}\text{H}_{55}\text{N}$ : 721.4296, found: 721.6074.

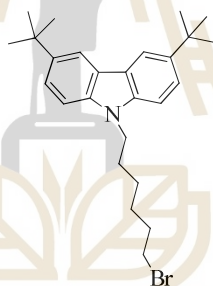
3,3',6,6'-Tetra-*tert*-butyl-6',6''-bis(3,6-di-*tert*-butyl carbazol-9-yl)-9''H-9,3':  
 9',3':6',9':3',9''-quinquebenzoindole (**8**)



A mixture of **4** (1.02 g, 1.78 mmol), **6** (3.21 g, 4.45 mmol), CuI (0.34 g, 1.78 mmol),  $\text{K}_3\text{PO}_4$  (1.90 g, 8.90 mmol) in 60 ml toluene was degassed with  $\text{N}_2$  for 3 times. *Trans*-1,2-diaminocyclohexane (0.25 ml, 1.78 mmol) was added in to the reaction mixture and then stirred at reflux under  $\text{N}_2$  atmosphere for 2 days. After cooling at room temperature, the reaction was extracted with  $\text{CH}_2\text{Cl}_2$  (20 ml  $\times$  3). The combine organic phase was washed with  $\text{H}_2\text{O}$  (50 ml) and brine solution (50 ml), dried over anhydrous  $\text{Na}_2\text{SO}_4$ . The organic phase was concentrated under vacuum. The crude product was recrystallized with dichloromethane-methanol. The resulting product **7** (2.10 g, 2.40 mmol) was dissolved with 30 ml of 2:1 THF-DMSO mixture, 1 ml  $\text{H}_2\text{O}$  and then added KOH (0.26 g, 4.80 mmol). The reaction was heated at 65  $^\circ\text{C}$  for 2 h. After cooling at room temperature, the reaction was extracted using  $\text{CH}_2\text{Cl}_2$  (20 ml  $\times$  3). The combine organic phase was washed with  $\text{H}_2\text{O}$  (50 ml) and brine solution (50 ml), dried over anhydrous  $\text{Na}_2\text{SO}_4$ . The organic phase was concentrated

under vacuum. The crude product was purified by column chromatography over silica gel eluting with a mixture of dichloromethane-hexane to obtain white solid compound (0.75 g, overall yield 58%); m.p. > 350 °C;  $^1\text{H-NMR}$  (600 MHz,  $\text{CDCl}_3$ ):  $\delta$  8.59 (s, 1H), 8.47 (s, 2H), 8.26 (s, 4H), 8.15 (s, 8H), 7.86-7.83 (m, 4H), 7.63-7.56 (m, 8H), 7.44 (dd,  $J = 8.6, 1.6$  Hz, 8H), 7.33 (d,  $J = 8.6$  Hz, 8H), 1.45 (s, 72H) ppm;  $^{13}\text{C-NMR}$  (151 MHz,  $\text{CDCl}_3$ ):  $\delta$  142.54, 141.41, 140.23, 139.68, 130.73, 129.66, 126.38, 126.00, 124.30, 123.76, 123.56, 123.11, 120.08, 119.39, 116.20, 112.47, 111.09, 109.12, 34.73, 32.05 ppm; FTIR 3044, 2957, 2864, 1578, 1485, 1362, 1229, 1306  $\text{cm}^{-1}$ ; MALDI-TOF (m/z) [ $\text{M}^+$ ] calcd for  $\text{C}_{116}\text{H}_{115}\text{N}_7$ : 1606.9248, found:1606.6956.

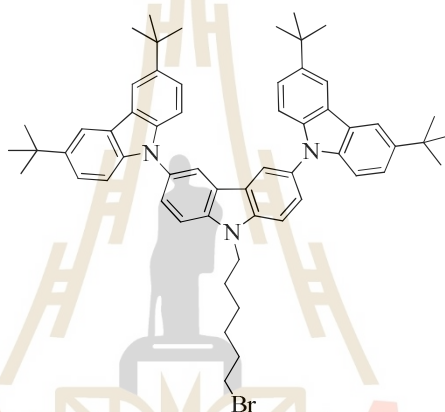
9-(6-Bromohexyl)-3,6-di-*tert*-butyl-carbazole (**9**)



Compound **2** (0.50 g, 1.78 mmol) was dissolved in dried DMF 30 ml at room temperature. KOH (0.40 g, 7.15 mmol) was then added into the mixture and stirred for 1 h. 1,6-Dibromohexane (1.10 ml, 7.15 mmol) was slowly added into the reaction. The reaction mixture was stirred overnight at room temperature. Some water was poured into the solution, extracted with dichloromethane several times. The combine organic phase was dried over anhydrous  $\text{Na}_2\text{SO}_4$ . After evaporation of the solvent, the crude was purified by column chromatography eluting with a mixture of dichloromethane-hexane to give white solid compound (0.58 g, 74%); m.p. 110-112 °C;  $^1\text{H-NMR}$  (600 MHz,  $\text{CDCl}_3$ ):  $\delta$  8.09 (s, 2H), 7.51 (d,  $J = 8.5$  Hz, 2H), 7.29 (d,  $J = 8.5$  Hz, 2H), 4.26 (t,  $J = 7.0$  Hz, 2H), 3.36 (t,  $J = 6.7$  Hz, 2H), 1.89-1.87 (m, 2H),

1.84-1.80 (m, 2H), 1.46 (s, 18H), 1.42-1.40 (m, 4H) ppm;  $^{13}\text{C-NMR}$  (151 MHz,  $\text{CDCl}_3$ );  $\delta$  141.53, 138.96, 123.25, 122.71, 116.29, 107.96, 42.96, 34.65, 33.71, 32.60, 32.07, 28.98, 27.97, 26.50 ppm; FTIR 3052, 2949, 2856, 1605, 1480, 1362, 1297, 1259, 1164, 1031  $\text{cm}^{-1}$ ; MALDI-TOF (m/z)  $[\text{M}^+]$  calcd for  $\text{C}_{26}\text{H}_{36}\text{BrN}$ : 441.2031, found: 441.4473.

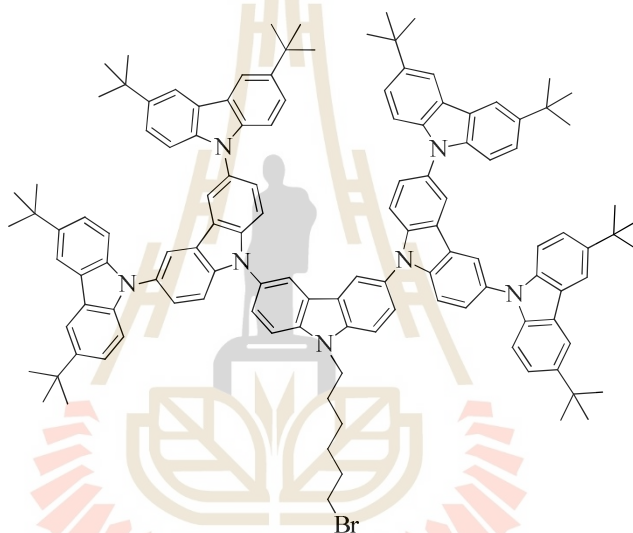
9'-(6-Bromohexyl)-3,3'',6,6''-tetra-*tert*-butyl-9,3':6',9''-terbenzo indole (**10**)



Compound **6** (0.40 g, 0.56 mmol) and KOH (0.12 g, 2.23 mmol) were added to a solution 1:2 of THF/DMF ratio. After the solution was stirred at room temperature for 1 h, 1,6-dibromohexane (3.36 ml, 2.22 mmol) was slowly added, following which the mixture was stirred at room temperature overnight. Some water was poured into the solution. The mixed solution was extracted with  $\text{CH}_2\text{Cl}_2$  (20 ml  $\times$  3). The combine organic phase was washed by  $\text{H}_2\text{O}$  (50 ml) and brine solution (50 ml), dried over anhydrous  $\text{Na}_2\text{SO}_4$ . The white solid compound was obtained after purified by column chromatography eluting with a mixture of dichloromethane-hexane (0.31 g, 62%); m.p. 298-300  $^\circ\text{C}$ ;  $^1\text{H-NMR}$  (600 MHz,  $\text{CDCl}_3$ ):  $\delta$  8.18 (s, 2H), 8.15 (s, 4H), 7.64 (d,  $J = 2.3$  Hz, 4H), 7.45 (dd,  $J = 8.5, 1.6$  Hz, 4H), 7.31 (d,  $J = 8.5$  Hz, 4H), 4.49 (t,  $J = 6.7$  Hz, 2H), 3.43 (t,  $J = 6.7$  Hz, 2H), 2.09-2.06 (m, 2H), 1.93-

1.91 (m, 2H), 1.61-1.57 (m, 4H), 1.46 (s, 36H) ppm;  $^{13}\text{C-NMR}$  (151 MHz,  $\text{CDCl}_3$ ):  $\delta$  142.50, 140.27, 139.94, 129.95, 125.75, 123.53, 123.45, 123.09, 119.50, 116.18, 109.88, 109.13, 43.51, 34.73, 33.68, 32.61, 32.06, 29.08, 28.00, 26.63 ppm; FTIR 3044, 2954, 2864, 1631, 1488, 1360, 1297, 1262, 1237  $\text{cm}^{-1}$ ; MALDI-TOF ( $m/z$ ) [ $\text{M}^+$ ] calcd for  $\text{C}_{58}\text{H}_{66}\text{BrN}_3$ : 883.4440, found: 883.7093.

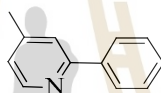
9''-(6-Bromohexyl)-3,3''',6,6'''-tetra-*tert*-butyl-6',6''-bis(3,6-di-*tert*-butyl-carbazol-9-yl)-9''H-9,3':9',3'':6'',9''':3''',9''''-quinquebenzoindole (**11**)



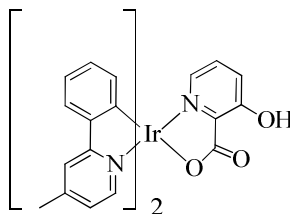
A mixture **8** (0.30 g, 0.19 mmol), KOH (0.04 g, 0.75 mmol) and 1:2 THF-DMF solution was stirred at room temperature for 1 h. 1,6-Dibromohexane (0.11 ml, 0.75 mmol) was slowly added to the mixture and then stirred overnight at this temperature. Water (10 ml) was added to the residue and the mixture was extracted with  $\text{CH}_2\text{Cl}_2$  (20 ml  $\times$  3). The combine organic phase was washed by  $\text{H}_2\text{O}$  (50 ml) and brine solution (50 ml), dried over anhydrous  $\text{Na}_2\text{SO}_4$ . The white solid compound was obtained after purified by column chromatography eluting with a mixture of dichloromethane-hexane (0.18 g, 55%); m.p. 305-307  $^\circ\text{C}$ ;  $^1\text{H-NMR}$  (600 MHz,  $\text{CDCl}_3$ ):  $\delta$  8.49 (s, 2H), 8.26 (s, 4H), 8.15 (s, 8H), 7.90-7.87 (m, 2H), 7.82 (d,  $J = 8.6$

Hz, 2H), 7.62-7.58 (m, 8H), 7.44 (dd,  $J = 8.5, 1.5$  Hz, 8H), 7.34 (d,  $J = 8.5$  Hz, 8H), 4.61 (t,  $J = 6.6$  Hz, 2H), 3.47 (t,  $J = 6.6$  Hz, 2H), 2.18-2.15 (m, 2H), 1.98-1.95 (m, 2H), 1.66-1.64 (m, 4H), 1.45 (s, 72H) ppm;  $^{13}\text{C-NMR}$  (151 MHz,  $\text{CDCl}_3$ ):  $\delta$  142.54, 141.47, 140.60, 140.24, 130.72, 129.12, 126.18, 126.00, 123.76, 123.56, 123.12, 120.16, 119.40, 116.21, 111.11, 110.51, 109.13, 43.17, 34.74, 33.66, 32.61, 32.06, 29.11, 28.00, 26.66 ppm; FTIR 3052, 2954, 2864, 1583, 1485, 1360, 1297, 1262, 1234, 1031  $\text{cm}^{-1}$ ; MALDI-TOF ( $m/z$ ) [ $\text{M}^+$ ] calcd for  $\text{C}_{112}\text{H}_{116}\text{BrN}_7$ : 1770.9271, found: 1770.5261.

#### 4-Methyl-2-phenylpyridine (**12**)



2-Bromo-4-methyl pyridine (0.50 g, 2.90 mmol), phenyl boronic acid (0.32 g, 2.64 mmol), 2 M  $\text{Na}_2\text{CO}_3$  (30.00 ml, 58.13 mmol) and  $\text{Pd}(\text{PPh}_3)_4$  (0.08 g, 0.07 mmol) was introduced in 50 ml dried THF in a two neck round bottom flask. The reaction mixture was then heated to reflux under nitrogen atmosphere for 24 h. After that it was cooled to room temperature and extracted into dichloromethane (15 ml  $\times$  3). The crude reaction was evaporated to dryness and then passed through silica column chromatography using dichloromethane-hexane to get the target product as a colorless oil (0.22 g, 70%);  $^1\text{H-NMR}$  (600 MHz,  $\text{CDCl}_3$ ):  $\delta$  8.65 (d,  $J = 4.8$  Hz, 1H), 8.08 (d,  $J = 7.4$  Hz, 2H), 7.64 (s, 1H), 7.56 (t,  $J = 7.4$  Hz, 2H), 7.50 (t,  $J = 7.4$  Hz, 1H), 7.15 (d,  $J = 4.8$  Hz, 1H), 2.50 (s, 3H) ppm;  $^{13}\text{C-NMR}$  (151 MHz,  $\text{CDCl}_3$ ):  $\delta$  157.39, 149.40, 147.79, 139.52, 128.83, 128.69, 126.96, 123.14, 121.56, 21.23 ppm; FTIR 3087, 3052, 2918, 1602, 1446, 1234, 1027  $\text{cm}^{-1}$ ; MALDI-TOF ( $m/z$ ) [ $\text{M}^+$ ] calcd for  $\text{C}_{12}\text{H}_{11}\text{N}$ : 170.2975, found: 170.1395.

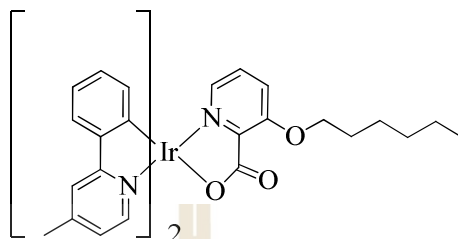
Iridium precursor (**13**)

4-Methyl-2-phenylpyridine (**12**) (0.06 g, 0.35 mmol),  $\text{IrCl}_3 \cdot 3\text{H}_2\text{O}$  (0.05 g, 0.14 mmol), 2-ethoxyethanol (3 ml),  $\text{H}_2\text{O}$  (1 ml) was refluxed over night under argon atmosphere. After cooling to room temperature, the  $\text{H}_2\text{O}$  was poured in to the reaction and stirred for 30 minute. The precipitate was collected by filtration, washed with water and methanol. The brick yellow dimer was obtained after drying.

A mixture of the above resulting dimer (0.10 g, 0.08 mmol), 3-hydroxy picolinic acid (0.04 g, 0.27 mmol),  $\text{Na}_2\text{CO}_3$  (0.76 g, 0.72 mmol) and 8 ml of 2-ethoxy ethanol was heated to 120 °C for 24 h under  $\text{N}_2$  atmosphere. After cooling the mixture to room temperature, a precipitate was filtered off and washed with water and ether. The yellow product was obtained by column chromatography on silica gel using acetone-dichloromethane as eluents (0.09 g, 72%); m.p. > 350 °C;  $^1\text{H-NMR}$  (600 MHz,  $\text{CDCl}_3$ ):  $\delta$  13.85 (s, 1H), 8.52 (d,  $J = 5.9$  Hz, 1H), 7.68 (s, 1H), 7.64 (s, 1H), 7.58-7.54 (m, 2H), 7.34 (t,  $J = 7.2$  Hz, 2H), 7.24 (d,  $J = 4.9$  Hz, 1H), 7.16-7.13 (m, 1H), 6.98 (d,  $J = 5.9$  Hz, 1H), 6.90 (t,  $J = 7.4$  Hz, 1H), 6.84 (t,  $J = 7.4$  Hz, 1H), 6.79-6.73 (m, 3H), 6.37 (d,  $J = 7.6$  Hz, 1H), 6.20 (d,  $J = 7.6$  Hz, 1H), 2.54 (s, 6H) ppm;  $^{13}\text{C-NMR}$  (151 MHz,  $\text{CDCl}_3$ ):  $\delta$  177.57, 168.54, 166.91, 160.56, 148.99, 148.83, 148.79, 148.20, 147.50, 146.09, 144.34, 144.05, 139.65, 135.01, 132.67, 132.53, 129.70, 129.47, 126.22, 124.02, 123.86, 123.43, 123.29, 121.62, 120.99, 119.76, 119.30, 21.38, 21.33 ppm; FTIR 3049, 2917, 2851, 1736, 1616, 1565, 1480, 1400,

1254, 1061, 1031  $\text{cm}^{-1}$ ; MALDI-TOF ( $m/z$ ) [ $M^+$ ] calcd for  $\text{C}_{30}\text{H}_{24}\text{IrN}_3\text{O}_3$ : 667.1447, found: 667.4183.

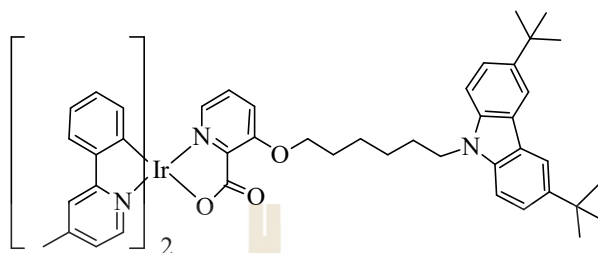
### Iridium complex (**IrG0**)



Compound **13** (0.10 g, 0.15 mmol),  $\text{K}_2\text{CO}_3$  (0.02 g, 0.16 mmol), 18-crown-6 (2.00 mg, 0.01 mmol) were dispersed in 15 ml of 1:1 acetone-DMSO mixture. The reaction mixture was degassed and then stirred at 55 °C for 1 h. 1-Bromohexane was then added into the solution under argon and stirred at 55 °C for 24 h. After cooling, some water was added into the reaction mixture, extracted with ethyl acetate and dried with anhydrous sodium sulfate. The solution was concentrated and purified by column chromatography using acetone-dichloromethane as eluents to obtain a bright yellow solid (0.06 g, 50%); m.p. 253-255 °C;  $^1\text{H-NMR}$  (600 MHz,  $\text{CDCl}_3$ ):  $\delta$  8.66 (d,  $J = 5.7$  Hz, 1H), 7.66 (s, 1H), 7.61 (s, 1H), 7.56 (d,  $J = 7.2$  Hz, 1H), 7.53 (d,  $J = 7.4$  Hz, 1H), 7.40 (d,  $J = 4.3$  Hz, 1H), 7.36-7.33(m, 2H), 7.15 (dd,  $J = 8.4, 5.0$  Hz, 1H), 6.95 (d,  $J = 4.5$  Hz, 1H), 6.88 (t,  $J = 7.1$  Hz, 1H), 6.81 (t,  $J = 7.1$  Hz, 1H), 6.75-6.73 (m, 3H), 6.39 (d,  $J = 7.4$  Hz, 1H), 6.14 (d,  $J = 7.4$  Hz, 1H), 4.11-4.07 (m, 2H), 2.52 (d,  $J = 5.6$  Hz, 6H), 1.94-1.92 (m, 2H), 1.50-1.45 (m, 2H), 1.33 (d,  $J = 3.1$  Hz, 4H), 0.91 (t,  $J = 3.1$  Hz, 3H) ppm;  $^{13}\text{C-NMR}$  (151 MHz,  $\text{CDCl}_3$ ):  $\delta$  171.46, 168.56, 167.12, 159.13, 149.65, 149.33, 148.54, 148.41, 147.50, 144.26, 144.21, 140.70, 132.66, 132.52, 129.65, 129.22, 128.20, 124.00, 123.74, 123.20, 123.04, 122.46, 121.19, 120.60, 119.58, 119.07, 70.05, 31.57, 28.85, 25.47, 22.51, 21.36, 21.28, 14.02 ppm; FTIR

3039, 2924, 2856, 1636, 1583, 1448, 1335, 1285, 1247, 1129, 1036  $\text{cm}^{-1}$ ; MALDI-TOF ( $m/z$ ) [ $M^+$ ] calcd for  $\text{C}_{36}\text{H}_{36}\text{IrN}_3\text{O}_3$ : 751.2386, found: 751.4088.

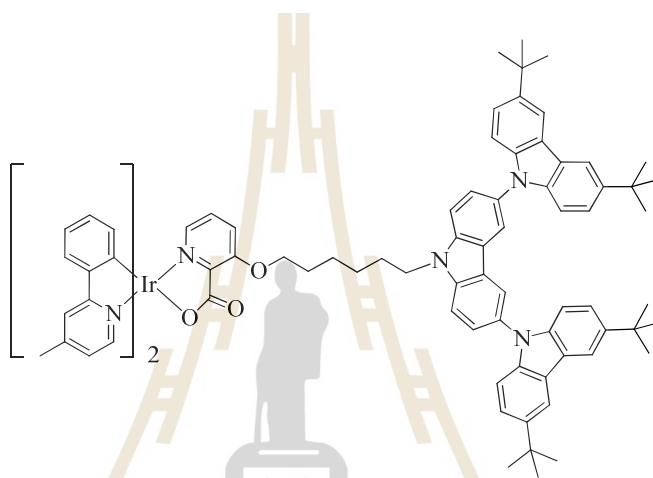
### Iridium complex (**IrG1**)



A mixture of **13** (0.07 g, 0.10 mmol),  $\text{K}_2\text{CO}_3$  (0.02 g, 0.15 mmol), 18-crown-6 (2.00 mg, 0.01 mmol) and 1:2 THF-DMF solution was heated at 55 °C under argon for 1 h. Compound **9** (0.05 g, 0.15 mmol) was then added into the solution under argon and stirred at this temperature for 24 h. the reaction was allowed to cool to room temperature. Some water was added to the residue and the mixture was extracted with  $\text{CH}_2\text{Cl}_2$  (15 ml  $\times$  3). The  $\text{CH}_2\text{Cl}_2$  extracts were combined, washed with brine (30 ml), dried over anhydrous  $\text{Na}_2\text{SO}_4$ . The bright yellow compound was obtained after purified by column chromatography using acetone-dichloromethane as eluents and dried under vacuum (0.06 g, 52%); m.p. 205-206 °C;  $^1\text{H-NMR}$  (600 MHz,  $\text{CDCl}_3$ ):  $\delta$  8.64 (d,  $J = 5.7$  Hz, 1H), 8.07 (s, 2H), 7.64 (s, 1H), 7.59 (s, 1H), 7.55 (d,  $J = 7.2$  Hz, 1H), 7.52 (d,  $J = 7.2$  Hz, 1H), 7.47 (dd,  $J = 8.4, 1.4$  Hz, 2H), 7.38 (d,  $J = 4.7$  Hz, 1H), 7.31 (d,  $J = 5.8$  Hz, 1H), 7.28 (d,  $J = 8.4$  Hz, 3H), 7.12 (dd,  $J = 8.4, 5.8$  Hz, 1H), 6.91 (d,  $J = 4.7$  Hz, 1H), 6.87 (t,  $J = 7.0$  Hz, 1H), 6.81 (t,  $J = 7.0$  Hz, 1H), 6.79 (t,  $J = 7.0$  Hz, 1H), 6.69 (d,  $J = 4.7$  Hz, 2H), 6.38 (d,  $J = 7.2$  Hz, 1H), 6.14 (d,  $J = 7.0$  Hz, 1H), 4.25 (t,  $J = 6.7$  Hz, 2H), 4.04-4.02 (m, 2H), 2.49 (s, 6H), 1.89-1.87 (m, 4H), 1.44 (s, 18H), 1.44-1.43 (m, 4H) ppm;  $^{13}\text{C-NMR}$  (151 MHz,  $\text{CDCl}_3$ ):  $\delta$  171.43, 168.54, 167.10, 159.02, 149.60, 149.25, 148.49, 148.43, 147.47, 144.25, 144.20,

141.43, 140.75, 139.02, 132.65, 132.51, 129.65, 129.23, 128.21, 124.00, 123.75, 123.25, 123.20, 123.03, 122.65, 122.42, 121.20, 120.61, 119.58, 119.08, 116.20, 108.10, 69.70, 43.03, 34.65, 32.08, 29.06, 28.76, 27.06, 25.66, 21.34, 21.27 ppm; FTIR 3517, 3054, 2954, 2861, 1648, 1580, 1480, 1362, 1247, 1127, 1034  $\text{cm}^{-1}$ ; MALDI-TOF ( $m/z$ ) [ $M^+$ ] calcd for  $\text{C}_{56}\text{H}_{59}\text{IrN}_4\text{O}_3$ : 1028.4026, found: 1028.8040.

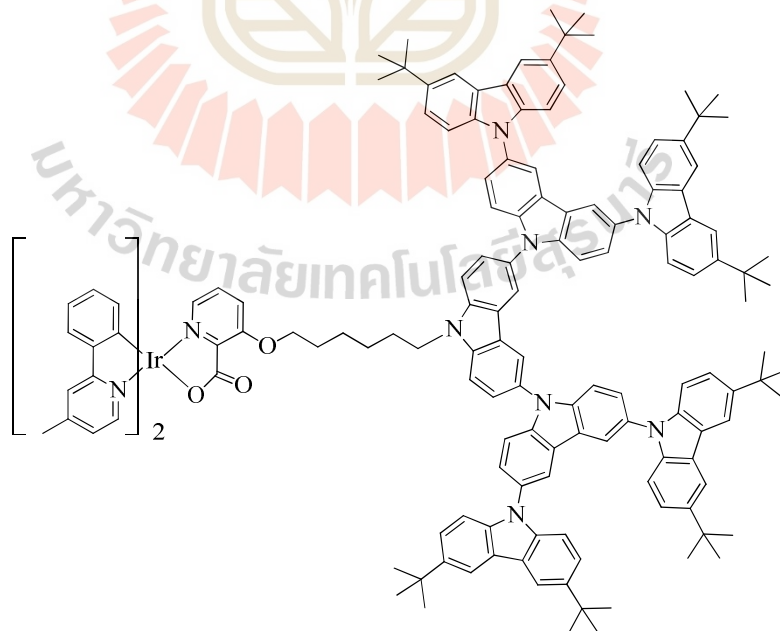
#### Iridium complex (**IrG2**)



To a mixture of **13** (0.07 g, 0.10 mmol),  $\text{K}_2\text{CO}_3$  (0.02 g, 0.11 mmol), 18-crown-6 (2.00 mg, 0.01 mmol) and 1:2 THF-DMF solution was heated at 55 °C under argon for 1 h. Compound **10** (0.10 g, 0.11 mmol) was added to the mixture at this temperature under argon and then heated for 24 h. After cooling at room temperature, the reaction was quenched with water and extracted with  $\text{CH}_2\text{Cl}_2$  (15 ml  $\times$  3). The combined organic layers were dried over anhydrous  $\text{Na}_2\text{SO}_4$ , filtered and then the solvent was completely removed. The crude product was purified by silica gel column chromatography with acetone-dichloromethane as eluents and dried under vacuum to afford bright yellow compound (0.07 g, 47%); m.p. 218-220 °C;  $^1\text{H-NMR}$  (600 MHz,  $\text{CDCl}_3$ ):  $\delta$  8.64 (s, 1H), 8.15 (s, 6H), 7.67 (d,  $J = 7.4$  Hz, 2H), 7.59 (s, 4H), 7.55 (d,  $J = 6.8$  Hz, 2H), 7.49 (d,  $J = 5.7$  Hz, 1H), 7.44-7.40 (m, 5H), 7.34 (d,  $J = 7.7$  Hz, 1H),

7.30 (d,  $J = 8.2$  Hz, 4H), 7.13 (dd,  $J = 8.4, 5.1$  Hz, 1H), 6.87 (d,  $J = 7.0$  Hz, 2H), 6.79 (t,  $J = 6.3$  Hz, 1H), 6.75 (t,  $J = 5.9$  Hz, 1H), 6.68 (d,  $J = 7.0$  Hz, 2H), 6.37 (d,  $J = 6.1$  Hz, 1H), 6.13 (d,  $J = 6.0$  Hz, 1H), 4.52 (t,  $J = 6.7$  Hz, 2H), 4.11 (t,  $J = 6.0$  Hz, 2H), 2.46 (s, 3H), 2.42 (s, 3H), 2.13-2.04 (m, 2H), 2.02-1.93 (m, 2H), 1.78-1.68 (m, 2H), 1.67-1.61 (m, 2H), 1.46 (s, 36H) ppm;  $^{13}\text{C}$ -NMR (151 MHz,  $\text{CDCl}_3$ ):  $\delta$  171.52, 168.54, 167.10, 159.05, 149.50, 149.11, 148.48, 147.43, 144.23, 144.17, 142.43, 140.81, 140.70, 140.29, 140.04, 132.65, 132.49, 129.75, 129.67, 129.25, 128.32, 125.66, 124.02, 123.78, 123.53, 123.36, 123.22, 123.05, 122.24, 121.23, 120.65, 119.60, 119.33, 119.09, 116.14, 110.19, 109.20, 69.75, 43.47, 34.73, 32.07, 29.71, 29.02, 27.02, 25.85, 21.32, 21.19 ppm; FTIR 3047, 2954, 2864, 1653, 1620, 1485, 1362, 1292, 1259, 1234, 1124, 1034  $\text{cm}^{-1}$ ; MALDI-TOF ( $m/z$ ) [ $\text{M}^+$ ] calcd for  $\text{C}_{88}\text{H}_{89}\text{IrN}_6\text{O}_3$ : 1470.6625, found: 1470.2563.

#### Iridium complex (**IrG3**)



Compound **13** (0.12 g, 0.18 mmol),  $\text{K}_2\text{CO}_3$  (0.03 g, 0.20 mmol), 18-crown-6 (2.00 mg, 0.01 mmol) was added in 30 ml of 1:2 THF-DMF mixed solution. The

reaction mixture was stirred and heated at 55 °C for 1 h and compound **11** (0.35 g, 0.20 mmol) was then added into the mixture at this temperature under argon. The mixture was allowed to cool to room temperature. The reaction was quenched with water and extracted with CH<sub>2</sub>Cl<sub>2</sub> (15 ml × 3). The combined organic layers were dried over anhydrous Na<sub>2</sub>SO<sub>4</sub>, filtered and then the solvent was completely removed. The bright yellow compound was obtained after purified by silica gel column chromatography using acetone-dichloromethane as eluents and dried under vacuum (0.06 g, 52%); m.p. 262-264 °C; <sup>1</sup>H-NMR (600 MHz, CDCl<sub>3</sub>): δ 8.65 (d, *J* = 5.9 Hz, 1H), 8.45 (d, *J* = 1.7 Hz, 2H), 8.26 (d, *J* = 1.5 Hz, 4H), 8.15 (d, *J* = 1.5 Hz, 8H), 7.88 (d, *J* = 8.7 Hz, 2H), 7.81 (d, *J* = 1.8 Hz, 1H), 7.80 (d, *J* = 1.8 Hz, 1H), 7.62 (s, 1H), 7.61 (s, 3H), 7.59 (d, *J* = 1.7 Hz, 4H), 7.57 (d, *J* = 2.0 Hz, 2H), 7.54 (d, *J* = 7.3 Hz, 1H), 7.48-7.40 (m, 10H), 7.37 (d, *J* = 8.1 Hz, 1H), 7.35-7.31 (m, 9H) 7.17 (dd, *J* = 8.7, 4.7 Hz, 1H) 6.86 (t, *J* = 6.9 Hz, 2H), 6.74 (t, *J* = 7.3 Hz, 2H), 6.69 (d, *J* = 4.7 Hz, 1H), 6.64 (t, *J* = 7.9 Hz, 1H), 6.37 (d, *J* = 7.5 Hz, 1H), 6.12 (d, *J* = 7.5 Hz, 1H), 4.65 (t, *J* = 7.3 Hz, 2H), 4.14 (t, *J* = 6.9 Hz, 2H), 2.45 (s, 3H), 2.40 (s, 3H), 2.17 (t, *J* = 7.6 Hz, 2H), 2.01 (dd, *J* = 14.4, 8.3 Hz, 2H), 1.88-1.78 (m, 2H), 1.76-1.66 (m, 2H), 1.45 (s, 72H) ppm; <sup>13</sup>C-NMR (151 MHz, CDCl<sub>3</sub>) δ 171.57, 168.57, 167.14, 159.06, 149.39, 149.03, 148.49, 148.41, 147.39, 144.20, 144.09, 142.49, 141.52, 140.87, 140.70, 140.24, 132.63, 132.46, 130.62, 129.69, 129.28, 128.86, 128.33, 126.08, 125.97, 124.03, 123.78, 123.69, 123.55, 123.18, 123.10, 123.00, 122.17, 121.28, 120.68, 119.94, 119.58, 119.32, 119.11, 116.17, 111.23, 110.91, 109.15, 69.79, 43.73, 32.06, 29.71, 29.02, 28.92, 27.07, 25.99, 21.33, 21.19 ppm; FTIR 3051, 2952, 2867, 1621, 1487, 1293, 1261, 1233, 1034 cm<sup>-1</sup>; MALDI-TOF (m/z) [M<sup>+</sup>] calcd for C<sub>152</sub>H<sub>149</sub>IrN<sub>10</sub>O<sub>3</sub>: 2356.1477, found: 2356.8601.

## 1.5 Results and discussion

### 1.5.1 Synthesis

#### The synthesis of self-hosting carbazole dendrons

The syntheses of the carbazole dendrons **2**, **6** and **8** are summarized in Figure 1.23. The first step in the synthesis, carbazole **1** was sonicated with 2-chloro-2-methyl propane under electrophilic substitution reaction in the presence of  $\text{ZnCl}_2$  as Lewis base in nitromethane as a solvent for 1 h to give 3,6-di-*tert*-butyl-9H-carbazole (**2**) as white solid in 71% yield. The next step involved an iodination reaction of carbazole (**1**) at C-3,6 positions with KI as nucleophile,  $\text{KIO}_3$  as base in a conc.  $\text{CH}_3\text{COOH}$  as a solvent to give a brown solid of 3,6-diiodo-9H-carbazole (**3**) in 77% yield. The resultant compound **3** was then tosylated with *p*-toluene sulfonyl chloride in the presence of KOH as base in dried acetone to afford 3,6-diiodo-9-tosyl-carbazole (**4**) in 86% yield. Following this procedure, compound **5** was formed from a coupling of **2** and **4** under Ullmann coupling reaction using  $\text{K}_3\text{PO}_4$  as base, CuI as catalyst and *trans*-1,2-diamino cyclohexane as co-catalyst in dried toluene solution refluxed for 2 days to obtain 3,3'',6,6''-tetra-*tert*-butyl-9'-tosyl-9,3':6',9''-terbenzoindole (**5**). Without purification process, the crude product (**5**) was then detosylated using KOH as base in the mixture of  $\text{H}_2\text{O}/\text{THF}/\text{DMSO}$  to 0.01:1:2 ratio to afford white solid compound of 3,3'',6,6''-tetra-*tert*-butyl-9,3':6',9''-terbenzoindole (**6**) in an overall yield of 65% for the two steps. The 3,3''',6,6'''-tetra-*tert*-butyl-6',6'''-bis(3,6-di-*tert*-butyl-carbazol-9-yl)-9''H-9,3':9',3'':6'',9''':3''',9''''-quinque-benzoindole (**8**) was obtained by Ullmann coupling reaction of compounds **6** and **4** to give **7**, and this was directly converted with detosylation reaction in an isolated overall yield of 58% in the two steps.

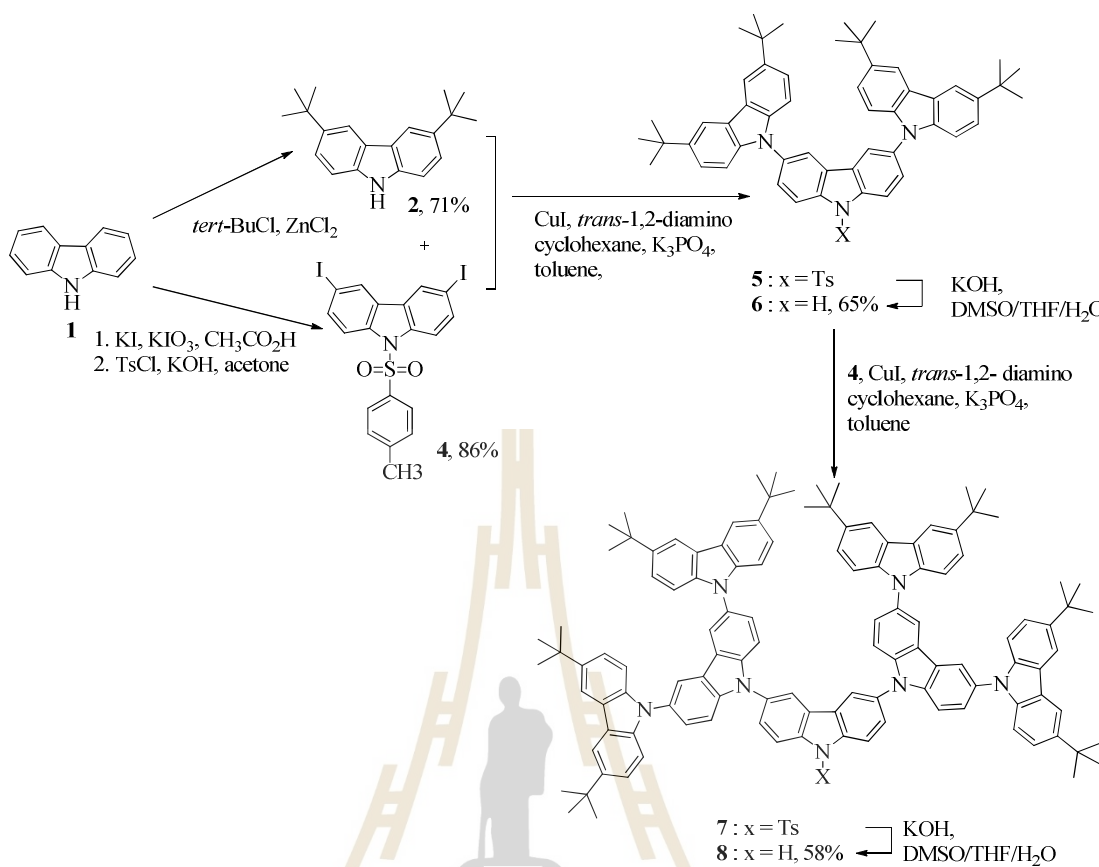


**Figure 1.23** The synthetic routes to three dendrimers **2**, **6** and **8**.

The Ullmann coupling reaction was used to synthesize two intermediate of the carbazole dendrimers **5** and **7**. It is a coupling reaction between C-N coupling of biaryl compounds using Cu(I) as catalyst under thermal conditions. The mechanism of the Ullmann coupling reaction is shown in Figure 1.24. The CuI active catalyst species undergoes oxidative addition with compound **2** to form an organocuprate reagent. The reaction followed by another oxidative addition reaction to form an other organocuprate and then reductive elimination to form the biaryl product **5** carbon-nitrogen bond.

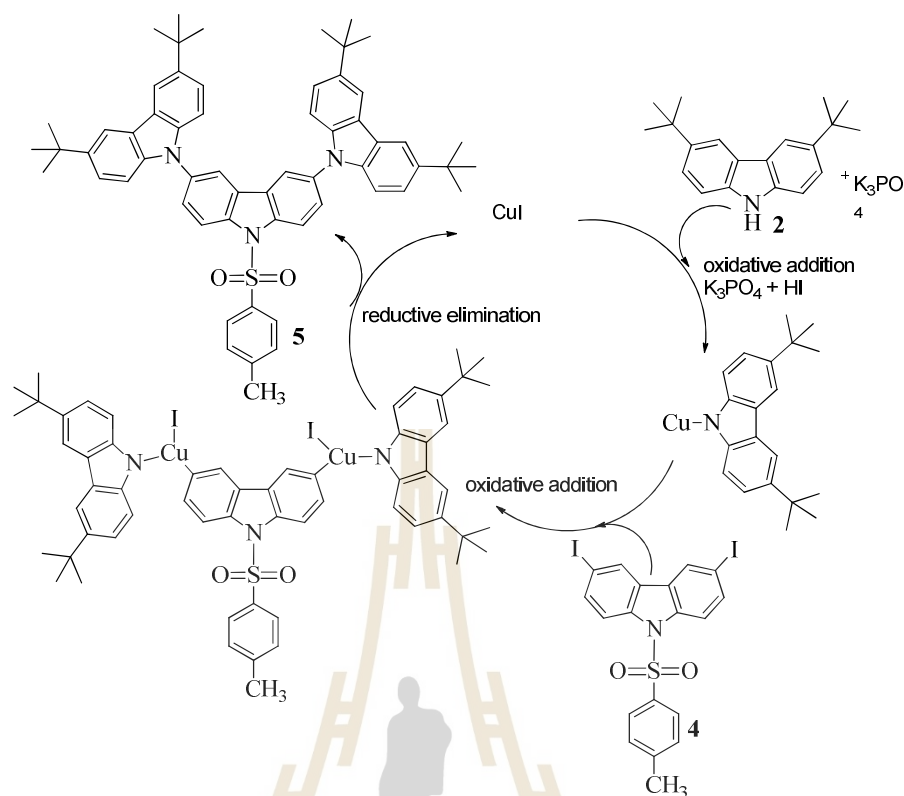


**Figure 1.24** The propose mechanism of Ullmann coupling reaction.

The molecular structure of product **2** was clearly confirmed by  $^1\text{H-NMR}$  analysis presented in Figure 1.25. The  $^1\text{H-NMR}$  spectrum of **2** shows the singlet signal of *tert*-buthyl substituent at **b** position located at chemical shift 1.45 ppm (18H). The singlet signal at chemical shift 8.07 ppm (2H) was observed from **a** position of compound **2**. This result indicated that two *tert*-buthyls were completely substituted on C-3,6-positions of carbazole **1**.

$^1\text{H-NMR}$  spectra of **6** and **8** reveals the similar proton position of **2**, but both molecules show the different chemical shift and integration ratio of the  $^1\text{H-NMR}$  signal. The  $^1\text{H-NMR}$  signals of **6** and **8** (see Figure 1.26) at chemical shift in the range 8.00-8.50 ppm were assigned as carbazole dendron generation 1<sup>st</sup>, 2<sup>nd</sup> and 3<sup>rd</sup> with the integration ratio of protons from 2 to 2:4 and 2:4:8, respectively. In addition, we

clearly observed the N-H singlet proton at chemical shifts 8.41 and 8.62 ppm of the dendrons **6** and **8**, respectively. This result concluded that both compounds were completely detosylated.

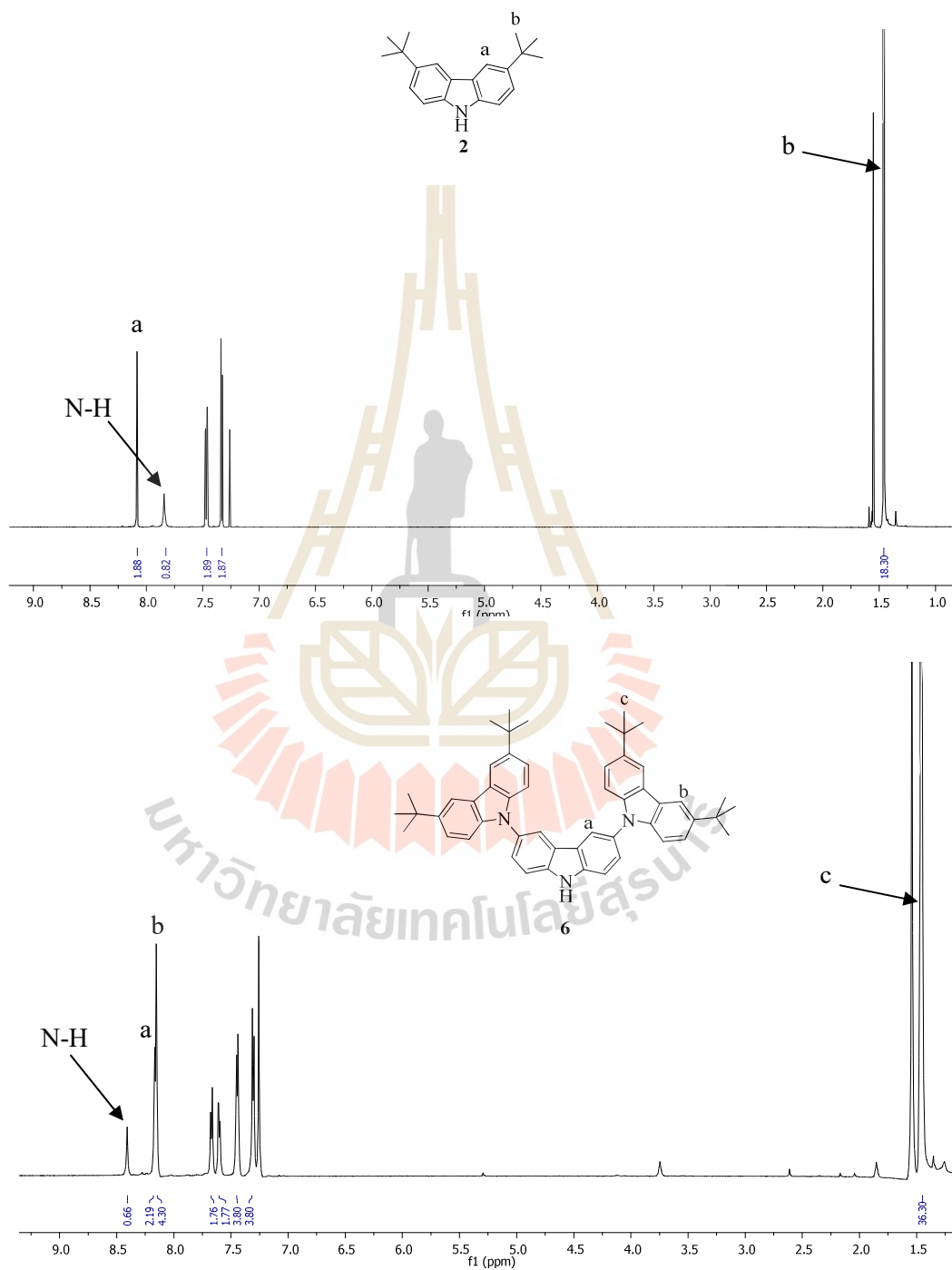
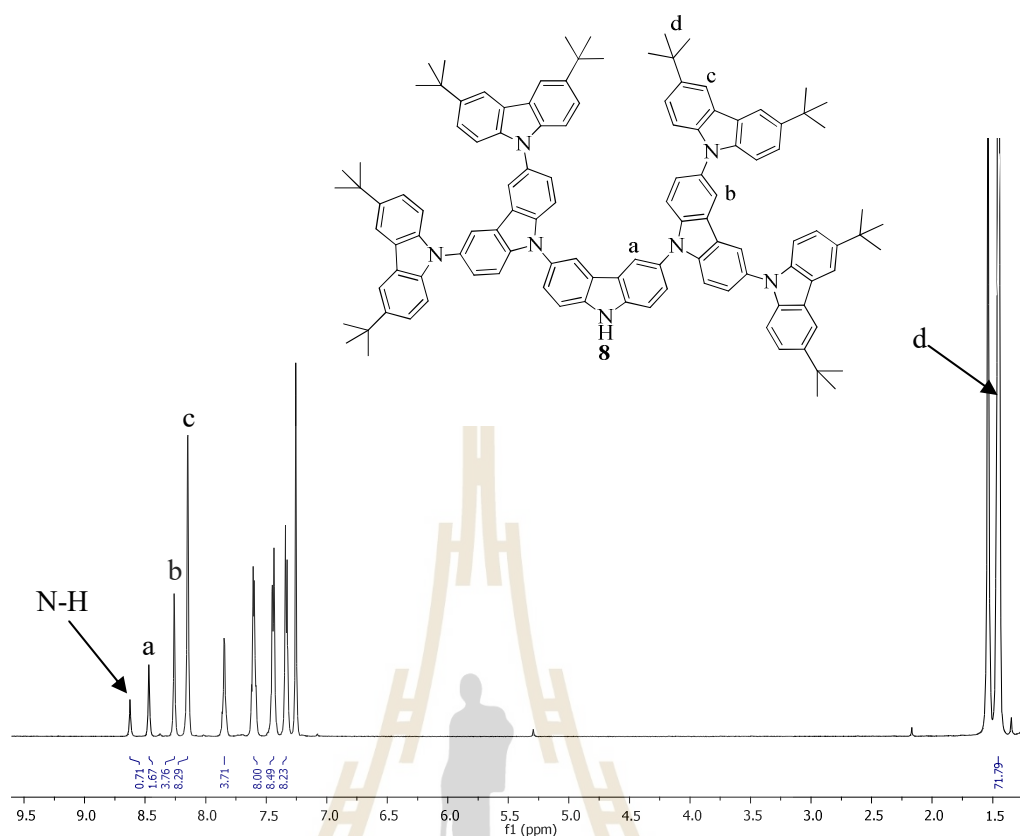


Figure 1.25 The <sup>1</sup>H-NMR spectra in CDCl<sub>3</sub> of **2** and **6**.



**Figure 1.26** The  $^1\text{H-NMR}$  spectrum in  $\text{CDCl}_3$  of molecule **8**.

For the non-conjugated self-hosting carbazole dendrons **9-11**, we chose 1,6-dibromohexane as the starting material which reacted with **2**, **6** (Figure 1.27) and **8** (Figure 1.28) under C-N alkylation reaction in the present of KOH as base in dimethyl formamide as solution at room temperature overnight. 9-(6-Bromohexyl)-3,6-di-*tert*-butyl-carbazole (**9**), 9'-(6-bromohexyl)-3,3'',6,6''-tetra-*tert*-butyl-9,3':6',9''-terbenzoindeole (**10**) and 9'''-(6-bromohexyl)-3,3''',6,6'''-tetra-*tert*-butyl-6',6'''-bis(3,6-di-*tert*-butyl-carbazol-9-yl)-9''H-9,3':9',3'':6'',9''':3'',9'''-quinquebenzoindeole (**11**) were obtained in 74%, 62% and 55% yields, respectively.

The target compounds **9-11** were also confirmed by  $^1\text{H-NMR}$  analysis. The  $^1\text{H-NMR}$  spectra of **9-11** (Figure 1.27-1.28) not only show the same pattern

comparing as the dendrimers **2**, **6** and **8**, respectively but also clearly observe 2 triplet signals at chemical shifts 3.00-4.00 ppm assigned as 2H of CH<sub>2</sub>-Br and 2H of *N*-alkyl proton positions.

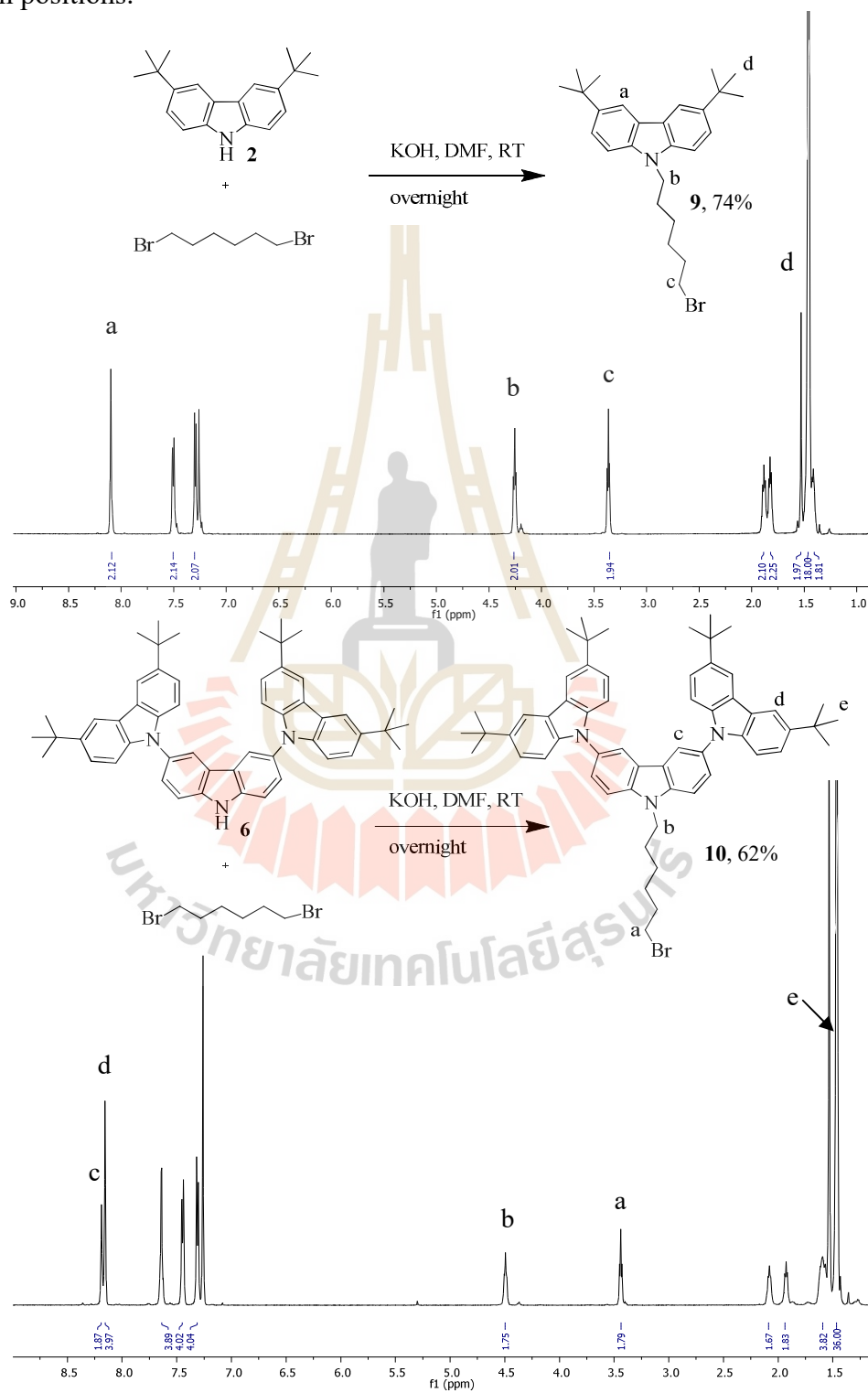


**Figure 1.27** The synthesis and <sup>1</sup>H-NMR spectra in CDCl<sub>3</sub> of **9** and **10**.

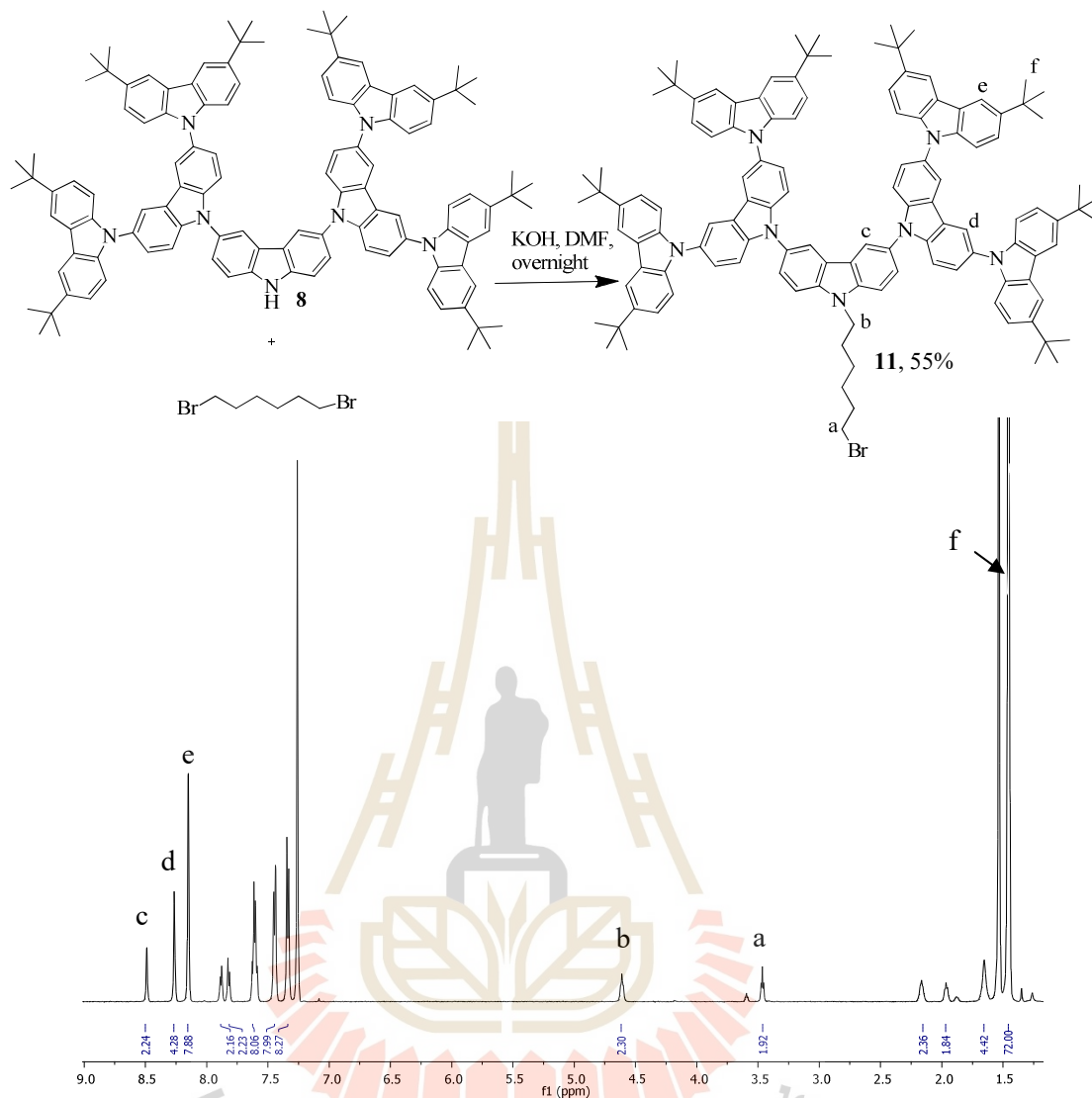


**Figure 1.28** The synthesis and <sup>1</sup>H-NMR spectrum in CDCl<sub>3</sub> of **11**.

### The synthesis of target Ir(III) complexes

The three-step procedure is used for the preparation of intermediate iridium(III) complex (**13**). First, Suzuki cross coupling reaction between phenyl boronic acid and 2-bromo-4-methyl pyridine using Pd(PPh<sub>3</sub>)<sub>4</sub> as catalyst, K<sub>2</sub>CO<sub>3</sub> as base in tetrahydrofuran as a solvent to obtain 4-methyl-2-phenylpyridine (**12**) in 71% yield. Molecule **12** was then reacted with iridium(III) chloride trihydrate in a 3:1 ratio of 2-ethoxyethanol/H<sub>2</sub>O mixture heated at reflux to obtain bis-iridium chloro-bridge

dimer without purification process. The formed bis-iridium chloro-bridged dimer was then reacted with excess 3-hydroxy pyridine-2-carboxylic acid in the presence of sodium carbonate as base in dimethyl sulfoxide/acetone **13** to yield in 72%.

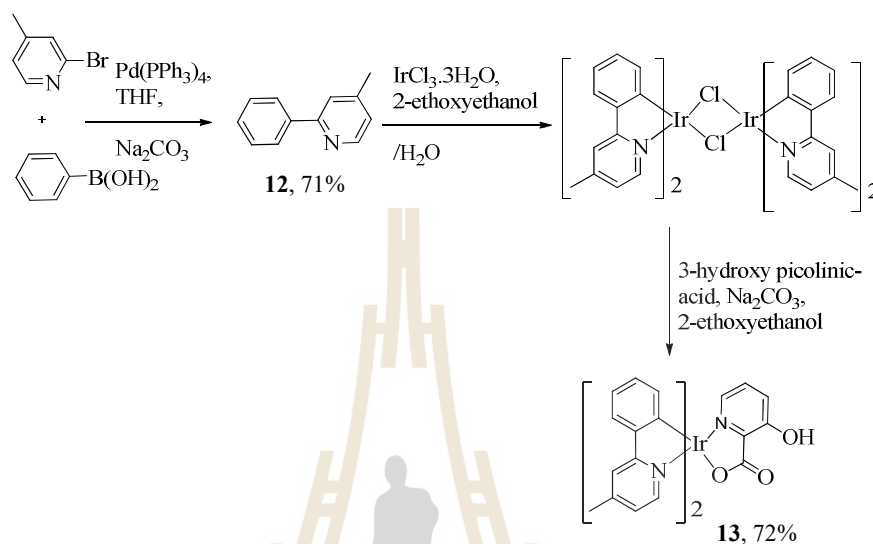


**Figure 1.29** The synthetic route to intermediate self-hosting iridium complex **13**.

Suzuki cross coupling reaction was used to synthesize the main ligand, compound **12**. The reaction is a coupling reaction between aryl halide and aryl boronic acid using Pd(0) as catalyst in thermal conditions. The mechanism of Suzuki cross coupling reaction is shown in Figure 1.30. The Pd(0) active catalyst species undergoes oxidative addition with 2-bromo-4-methyl pyridine to form Pd(II) complex. The reaction followed by transmetallation reaction where its R group replaces the halide anion on the Pd(II) complex and then reductive elimination to form the biaryl product **12** carbon-carbon bond.

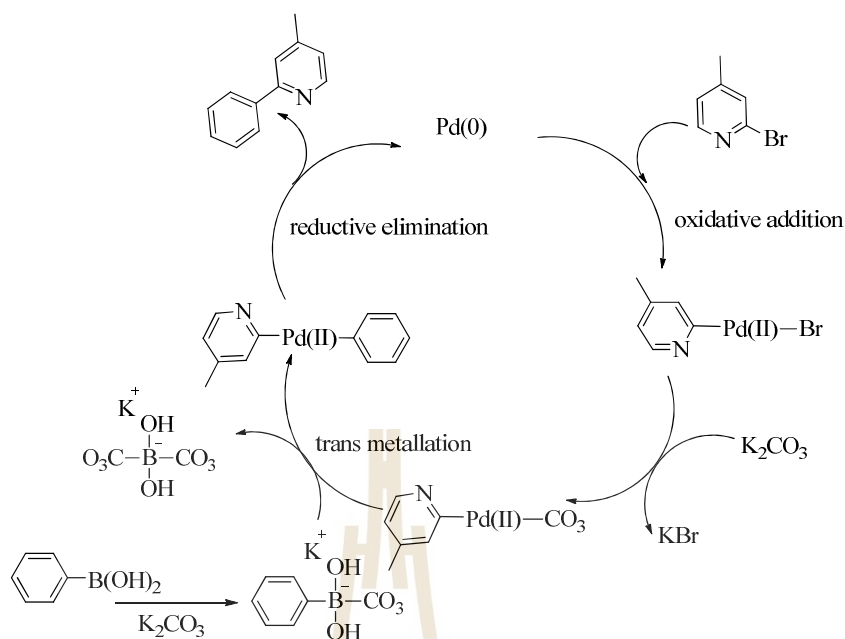


**Figure 1.30** The propose mechanism of Suzuki cross coupling reaction of **12**.

The molecular structure of the intermediate **13** was confirmed by <sup>1</sup>H-NMR analysis and MALDI-TOF MS before synthesizing to the next step is shown in Figure 1.31. A singlet signal at 13.85 ppm (1H) was found from the <sup>1</sup>H-NMR spectrum assigned as O-H proton signal of picolinic moiety as ancillary ligand. Moreover, we observed the singlet proton signal at chemical shift 2.54 ppm (6H) obtained from methyl substituent on pyridine ring. The MALDI-TOF MS spectrum of **13** was found to be 667.4183 m/z, calculated for C<sub>30</sub>H<sub>24</sub>IrN<sub>3</sub>O<sub>3</sub>.

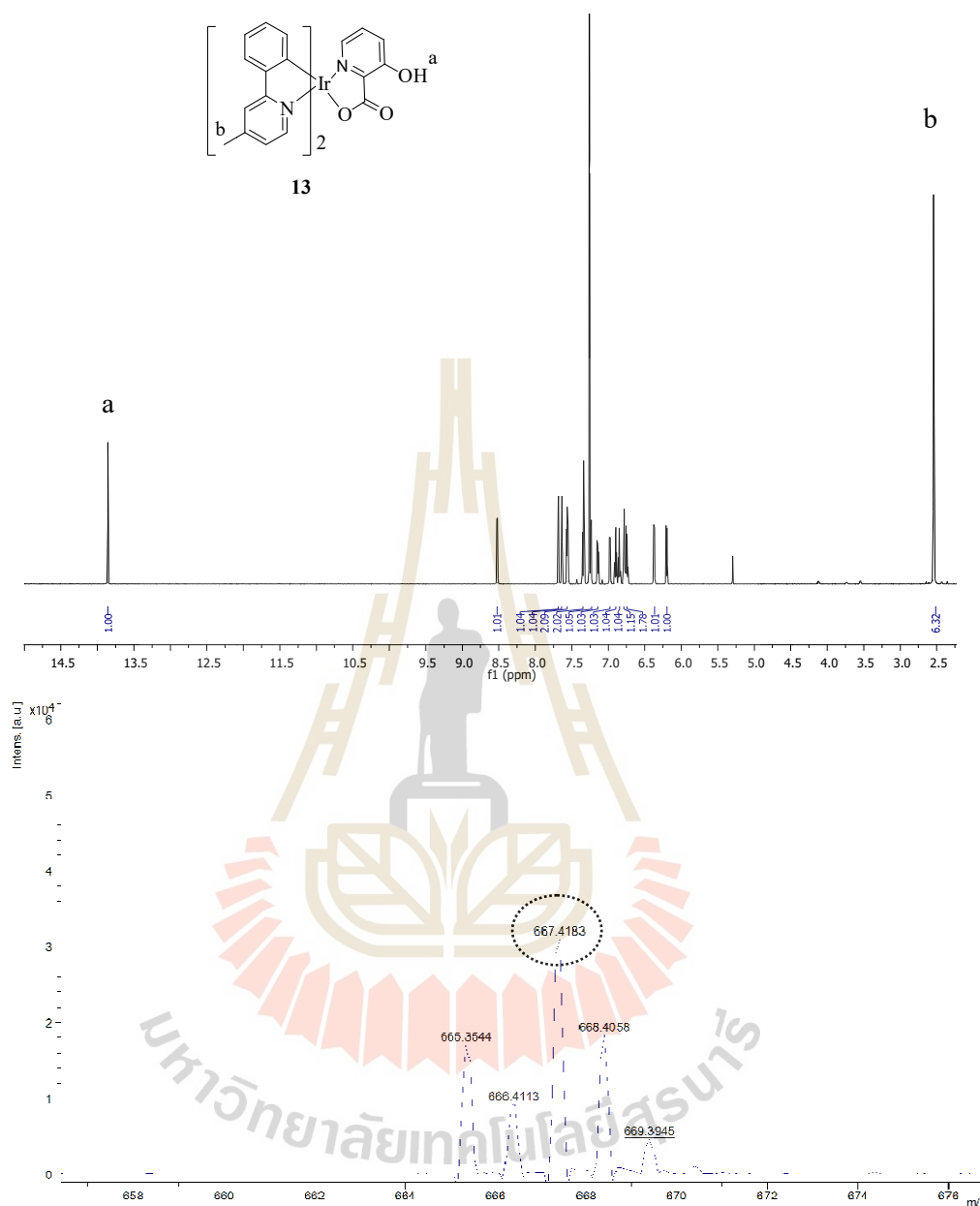


**Figure 1.31** The <sup>1</sup>H-NMR in CDCl<sub>3</sub> and MALDI-TOF MS spectra of **13**.

In the final step of the synthesis target self-hosting iridium complexes (**IrG0**, **IrG1**, **IrG2** and **IrG3**), each self-hosting cabazole dendrimer part (bromo hexane and **9-11**) was reacted with **13** in the presence of K<sub>2</sub>CO<sub>3</sub> as base, 18-crown-6 as coordinate ligand for potassium cation in the mixture of acetone/DMSO as solvents

to give all complexes in 50, 52, 47 and 52% yield for **IrG0**, **IrG1**, **IrG2** and **IrG3**, respectively shown in Figure 1.32-1.34.

The  $^1\text{H-NMR}$  spectrum of **IrG0** shows the same proton pattern compared to the intermediate **13** while this spectrum is clearly not show O-H proton signal in the aromatic region at chemical shift 13.85 ppm. In addition, the  $^1\text{H-NMR}$  signals at chemical shift 4.07 ppm (2H) was observed indicating to O-CH<sub>2</sub> proton signal. This result confirmed that O-H proton position of the intermediate **13** was completely substituted with hexyl part to give **IrG0** complex, shown in Figure 1.32. The MALDI-TOF MS spectrum was observed to be 751.4088 m/z, calculated for C<sub>36</sub>H<sub>36</sub>IrN<sub>3</sub>O<sub>3</sub>: 751.2386.

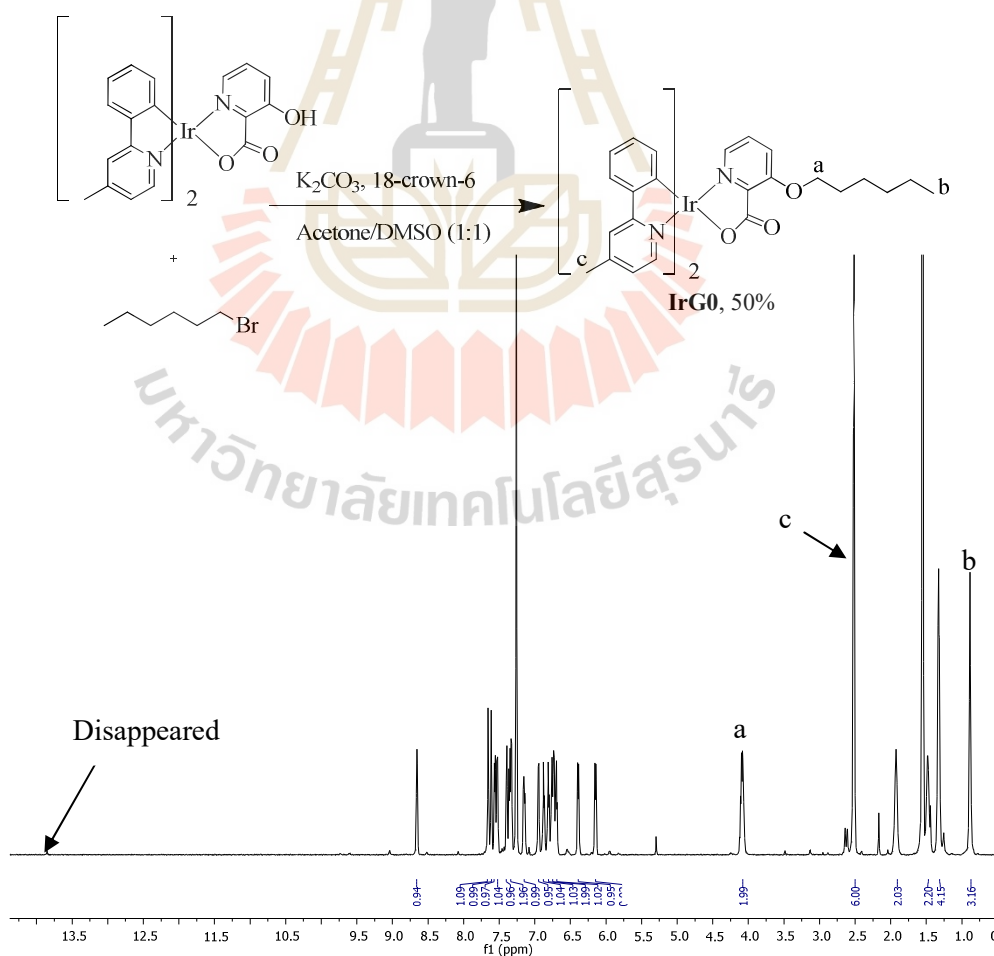


**Figure 1.32** The synthesis and  $^1\text{H-NMR}$  spectrum in  $\text{CDCl}_3$  of **IrG0**.

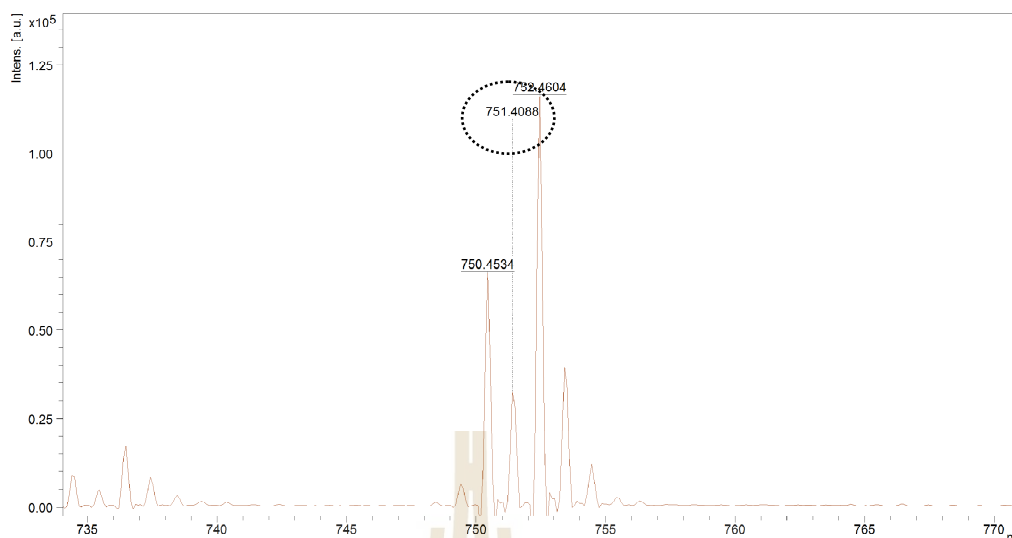


**Figure 1.33** The MALDI-TOF MS spectrum of **IrG0**.

The  $^1\text{H-NMR}$  spectra of **IrG1** (Figure 1.34), **IrG2** (Figure 1.35) and **IrG3** (Figure 1.36) show the same proton pattern compared with **IrG0**. The spectra are clearly not show O-H proton signal at chemical shift 13.85 ppm that observed those of intermediate **13**. In addition, all complexes were observed  $^1\text{H-NMR}$  signal pattern of singlet proton at **d**, **e** and **f** positions in aromatic region like **2**, **6** and **8** with integration ratio of 2, 2:4 to 2:4:8, respectively. The  $^1\text{H-NMR}$  signals at chemical shift 4.00-4.70 ppm (4H) was observed corresponding to O-CH<sub>2</sub> and N-CH<sub>2</sub> proton signal of all complexes. This result confirmed that O-H proton position of intermediate **13** was completely substituted with each non-conjugated self-hosting carbazole dendrimer parts of the complexes. The MALDI-TOF MS was used to confirm the structure and found to be 1028.8040, 1470.2563 and 2356.8601 m/z for **IrG1**, **IrG2** and **IrG3**, respectively.

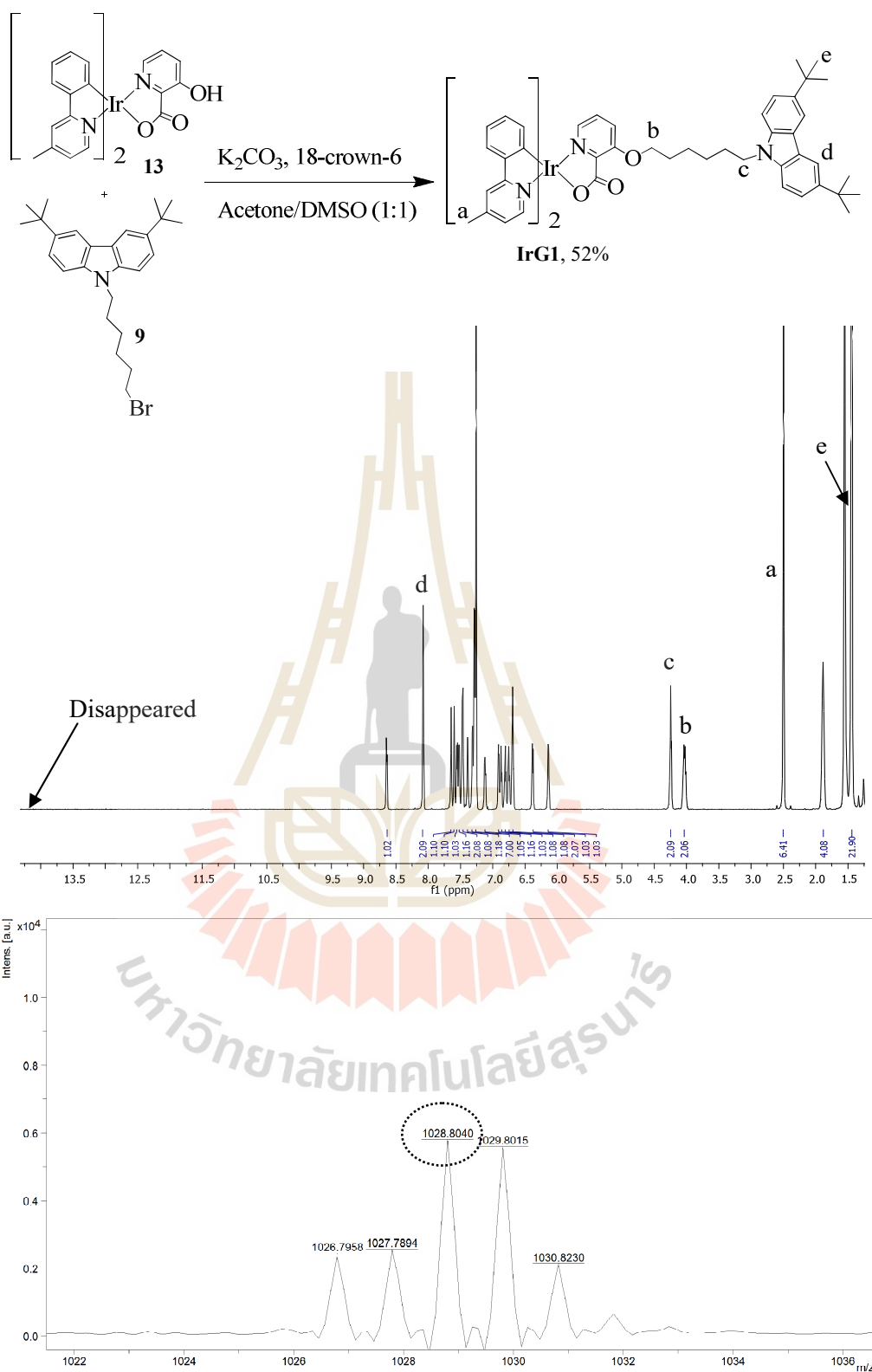
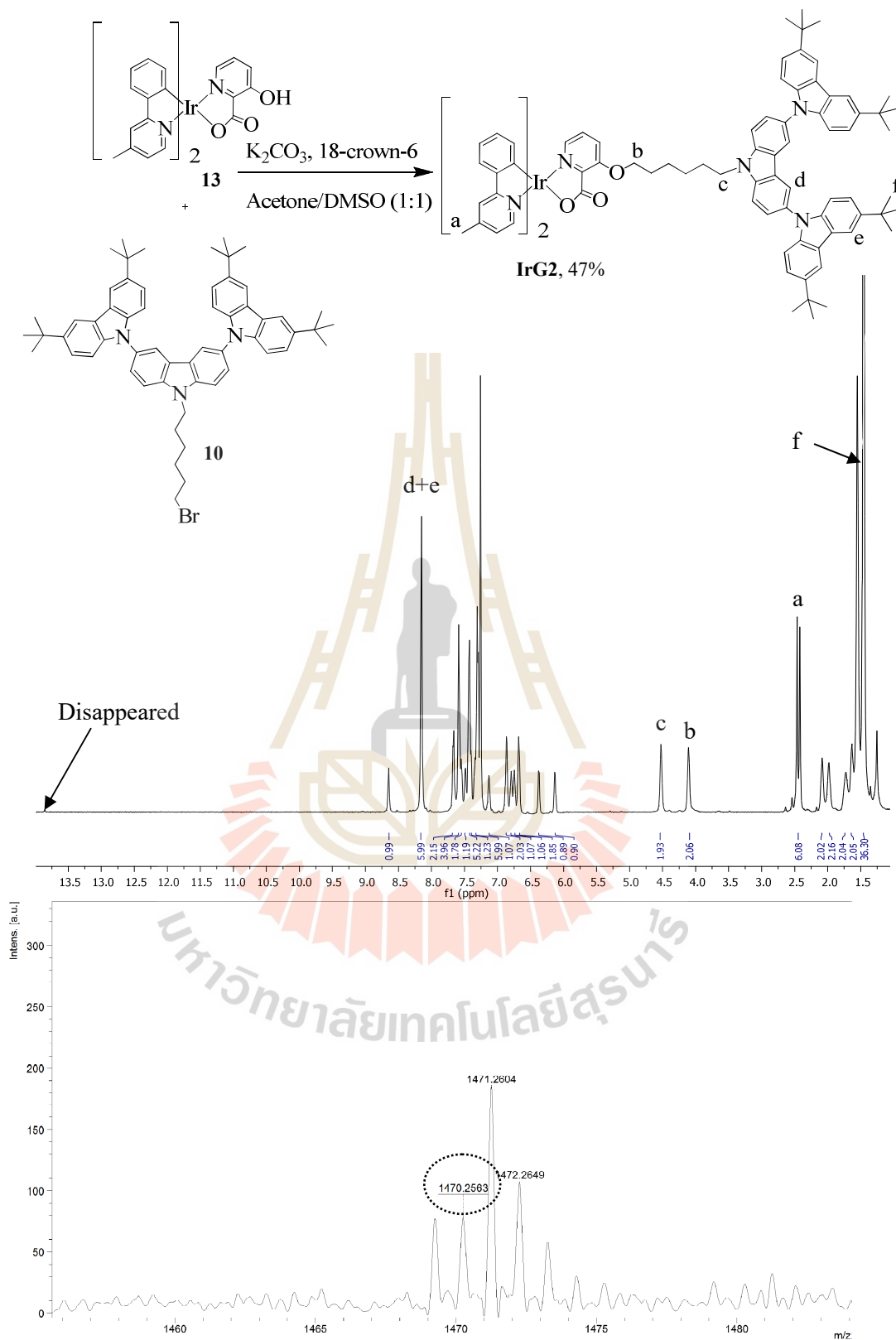
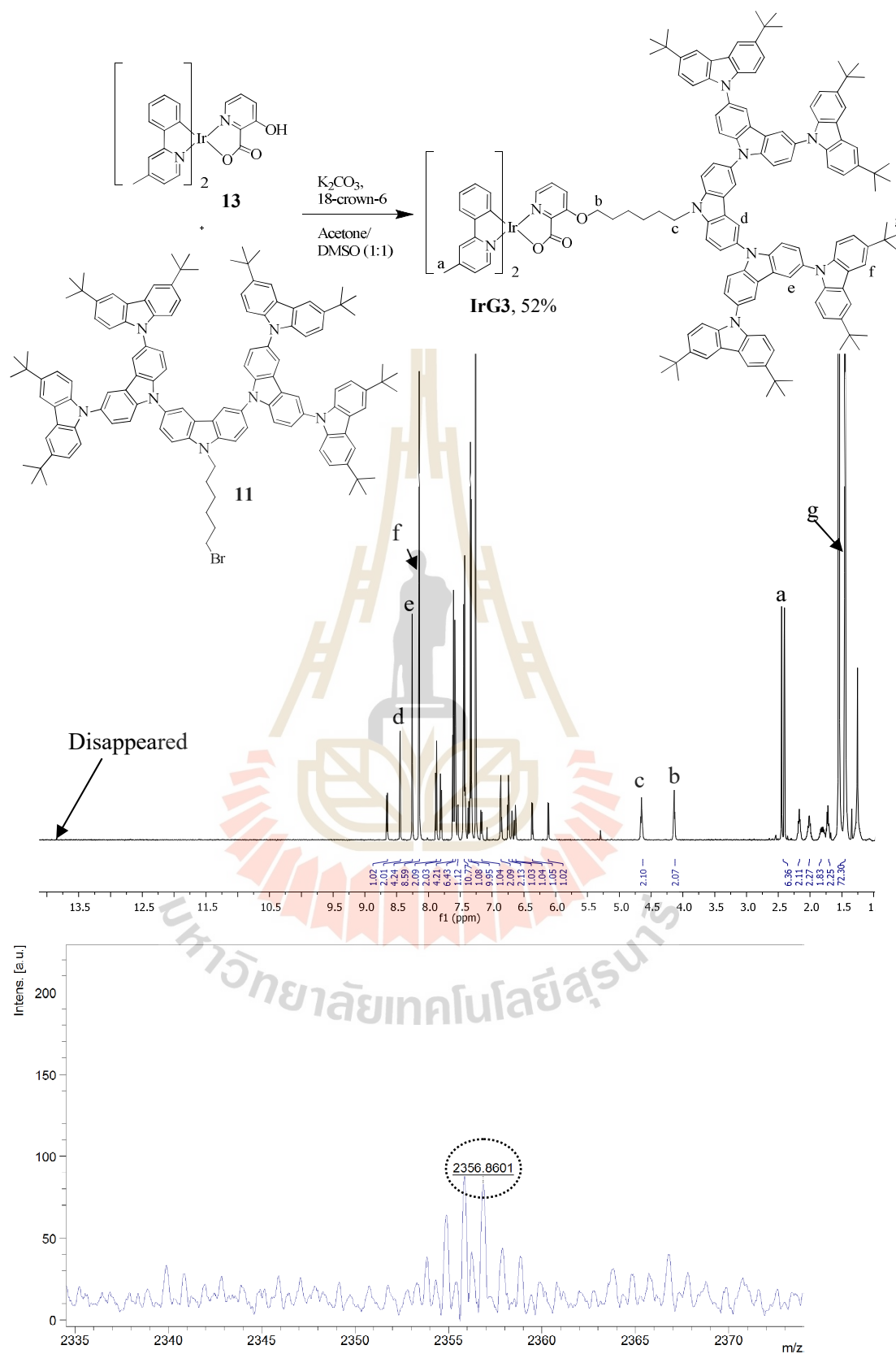


Figure 1.34 The synthesis, <sup>1</sup>H-NMR in CDCl<sub>3</sub> and MALDI-TOF MS spectra of IrG1.



**Figure 1.35** The synthesis,  $^{1}H$ -NMR in  $CDCl_3$  and MALDI-TOF MS spectra of IrG2.



**Figure 1.36** The synthesis,  $^1H$ -NMR in  $CDCl_3$  and MALDI-TOF MS spectra of IrG3.

### 1.5.2 Optical properties

UV-Vis absorption spectra of all Ir(III) complexes, **IrG0** to **IrG3**, in dichloromethane (CH<sub>2</sub>Cl<sub>2</sub>) solution are shown in Figure 1.37 and data are listed in Table 1.2. All complexes show three main absorbance regions. The first region at around 298 nm that assigns to the  $\pi\text{-}\pi^*$  electron transition of the periphery carbazole moieties. For this region, the absorption wavelength shows difference results based on molecular size of carbazole dendrimers. The molar coefficients are increased from the **IrG1** to the **IrG3**, which is attributed to the increased number of carbazole dendromer units on ancillary ligand except **IrG0** without carbazole unit. For example, the  $\epsilon$  values at 298 nm for **IrG1**, **IrG2** and **IrG3** were 1280, 4902 and 6650 M<sup>-1</sup> cm<sup>-1</sup>, respectively. Second, the absorbance around 320-360 nm is consistent with the spin allowed  $\pi\text{-}\pi^*$  transition of the C<sup>^</sup>N ligands and picolinic ancillary ligands. The third absorption band, weaker bands around 350-450 nm were assigned to singlet to triplet metal-to-ligand charge transfer (MLCT) transitions arising from the Ir(III) metal complex. In the thin film, all complexes show similar result absorption spectra in the region around 270-450 nm compared with these complexes in CH<sub>2</sub>Cl<sub>2</sub> solution.

The emission spectra of all complexes exhibited yellow phosphorescent emissions at  $\lambda_{\text{em}} = 580\text{-}590$  nm. These results agree well with our theoretical prediction and suggestion that the introduction of the dendrimers **2**, **6** and **8** moieties with non-conjugated into the 3-hydroxy-2-picolinic acid ancillary ligand make a little impact on their emissions.

On going from solution to the solid state, **IrG0**, **IrG1**, **IrG2** and **IrG3** exhibit small blue shifted of about 24, 32, 34 and 46 nm, respectively, which is associated with the appearance of a long tail in the range of  $\lambda_{\text{abs}} = 280\text{-}350$  nm. This

finding supported that the non conjugated linkage with carbazole dendron suppressed intermolecular  $\pi$ - $\pi$  interactions in the solid state.

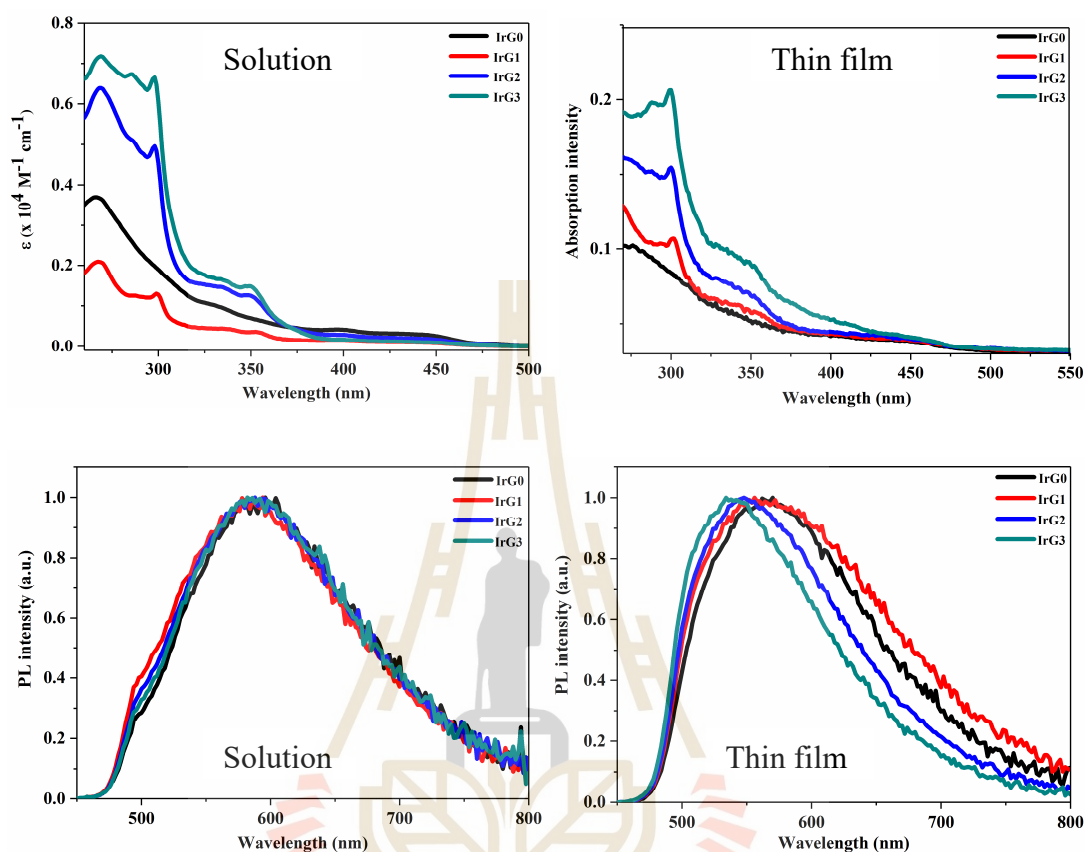


**Figure 1.37** Absorption and PL intensity spectra of all Ir(III) complexes in  $\text{CH}_2\text{Cl}_2$  solution and thin film.

### 1.5.3 Photoluminescence lifetime of Ir(III) complexes

Figure 1.38 shows the average lifetime estimated by biexponential fit of emission decay curves. The emission lifetime of all complexes in  $\text{CH}_2\text{Cl}_2$  solution ( $\text{O}_2$  and  $\text{O}_2$  free) and thin film exhibited the similar result. The data were summarized in Table 1.2. The tendency of lifetime was increased from 102.18 ns for **IrG0** to 135.84 ns for **IrG1** and 195.05 ns for **IrG2**. However, when the number of carbazole was increased to **IrG3**, the emission lifetime slightly decreased to 170.42 ns. This result

corresponds with Wang's report (Wang et al., 2015). When the range from Ir(III) emissive core complex to the end of self-hosting more than  $30 \text{ \AA}$ , the intramolecular charge transfer from host to iridium core emissive as guest was decreased resulting in shortening lifetime. It can be concluded that the molecular size of self-hosting iridium complex is importance.

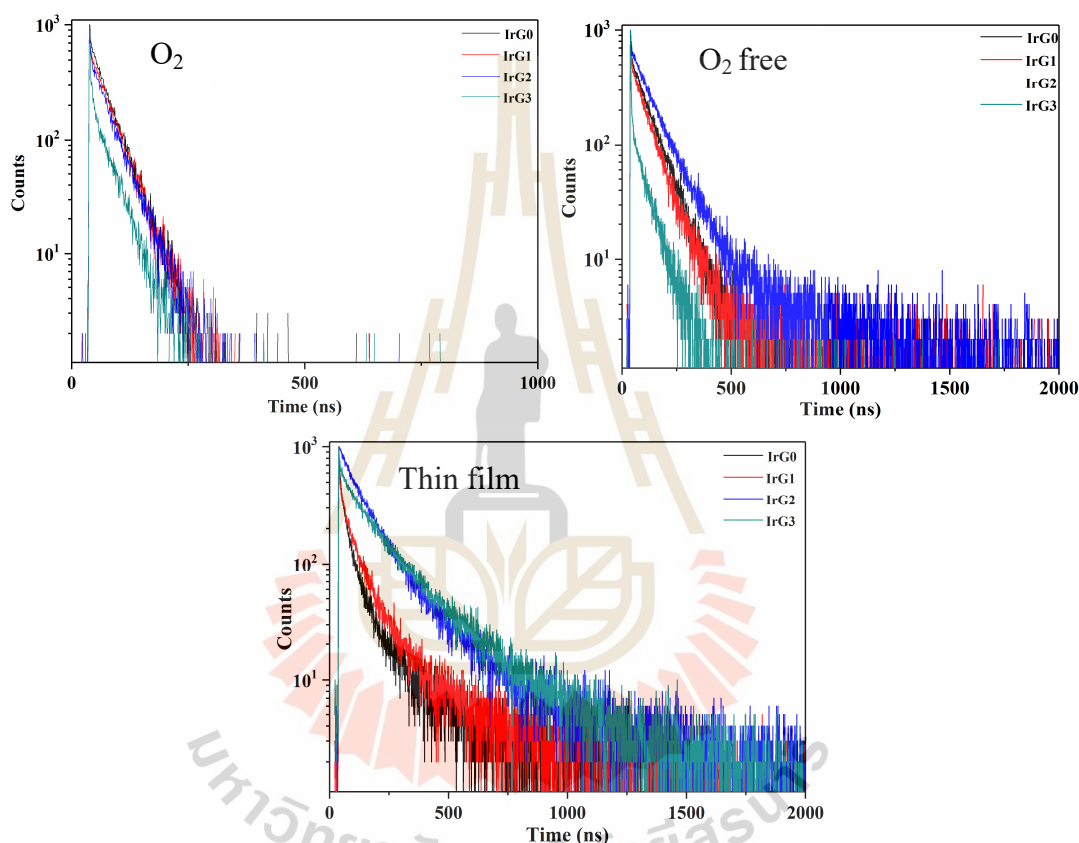


**Figure 1.38** Photoluminescence lifetimes of all self-hosting Ir(III) complexes in  $\text{CH}_2\text{Cl}_2$  solution ( $\text{O}_2$  and  $\text{O}_2$  free) and thin film.

To prove the effect of  $\text{O}_2$  quenching theory for phosphorescent emitters in the solution, all complexes were measured the photoluminescence lifetime under  $\text{O}_2$  and  $\text{O}_2$  free (Figure 1.39). The **IrG0**, **IrG1**, **IrG2** and **IrG3** in  $\text{CH}_2\text{Cl}_2$  solution under  $\text{O}_2$  show the emission lifetime value of 30.15, 36.29, 37.83 and 33.79 ns, respectively.

The photoluminescence lifetimes with O<sub>2</sub> free for all complexes are increased to 78.89, 79.87, 90.83 and 58.71 ns for **IrG0**, **IrG1**, **IrG2** and **IrG3**, respectively. All complexes in the CH<sub>2</sub>Cl<sub>2</sub> solution with O<sub>2</sub> free exhibit longer lifetime than with O<sub>2</sub> suggesting from phosphorescent character of the complexes.

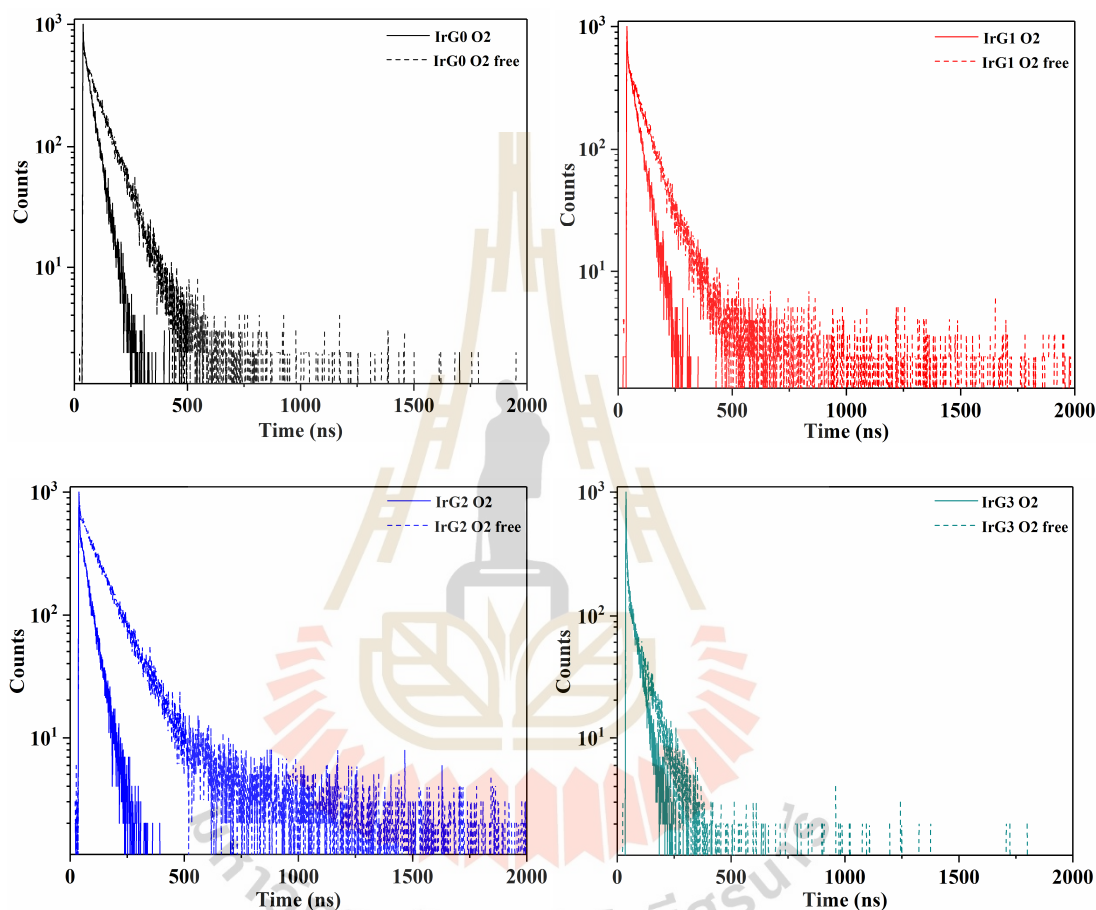


**Figure 1.39** Photoluminescence lifetimes of all self-hosting Ir(III) complexes in CH<sub>2</sub>Cl<sub>2</sub> solution under O<sub>2</sub> (solid line) and O<sub>2</sub> free (dashed line).

This observation was described in Figure 1.40. The emission of the complexes related with triplet exciton (T<sub>1</sub>), so the emission of triplet exciton was quenched by directly transfer energy to ground state triplet oxygen (<sup>3</sup>O<sub>2</sub>) to produce reactive <sup>1</sup>O<sub>2</sub> resulting in shortening lifetime.

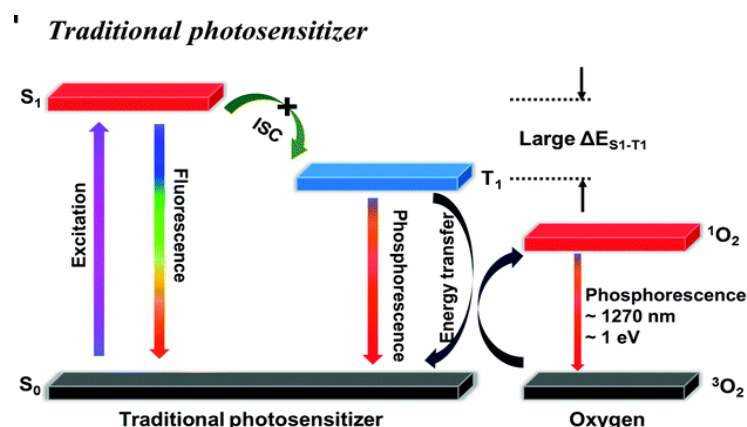


**Figure 1.40** The electron energy transfer of phosphorescent compound.

**Table 1.2** Photophysical properties and emission lifetimes of **IrG0-IrG3**.

Comp.	$\lambda_{\text{abs}}^{\text{sol}}$ ( $\epsilon$ ) (nm, $M^{-1}cm^{-1}$ ) <sup>a</sup>	$\lambda_{\text{em}}^{\text{sol}}/\lambda_{\text{em}}^{\text{film}}$ (nm) <sup>b</sup>	$\tau_p$ (ns) <sup>c</sup>		
			O <sub>2</sub>	O <sub>2</sub> free	film
<b>IrG0</b>	442 (306)	594/570	30.15	78.89	102.18
<b>IrG1</b>	443 (98)	588/556	36.29	79.87	135.84
<b>IrG2</b>	443 (183)	582/548	37.83	90.83	195.05
<b>IrG3</b>	443 (117)	598/534	33.79	58.71	170.42

<sup>a</sup> Measured in  $CH_2Cl_2$  ( $10^{-4}$  M) at 298 K.

<sup>b</sup> Measured in  $CH_2Cl_2$  ( $10^{-5}$  M) and thin film at 298 K.

<sup>c</sup> Measured in  $CH_2Cl_2$  ( $10^{-5}$  M) (O<sub>2</sub> and O<sub>2</sub> free) and thin film at 298 K.

### 1.5.4 Electrochemical properties

Electrochemical properties of **IrG0**, **IrG1**, **IrG2** and **IrG3** in  $CH_2Cl_2$  solution containing 0.1 M tetra butyl ammonium hexafluorophosphate as supporting electrolyte were studied by cyclic voltammetry (see Figure 1.41). The data are summarized in Table 1.3. According to the equation  $E_{\text{HOMO}} = -(4.44 + E_{\text{onset}})$ , the HOMO and LUMO energies of all complexes were calculated. All complexes show

reversible oxidation in the range of 0.60-1.50 V vs Ag/AgCl. According to previous electrochemical studies on iridium complexes, the oxidation wave are assigned to metal centered Ir(III)/Ir(IV) oxidation process. The others located at more positive potentials are related to the surrounding carbazole dendrons oxidation. The corresponding HOMO levels of **IrG0**, **IrG1**, **IrG2** and **IrG3** are determined to be -5.31, -5.30, -5.29 and -5.29 eV, respectively. According to the optical band gap ( $E_g$ ) estimated from the absorption onset, the LUMO levels of **IrG0** to **IrG3** are calculated to be -2.83, -2.79, -2.78 and -2.78 eV, respectively. The similar energy-level alignment of all Ir(III) complexes further illustrates that the non-conjugated linkage is small impact to oxidation maintain the properties of the emissive Ir(III) core corresponding to UV-Vis and photoluminescence results as expected.

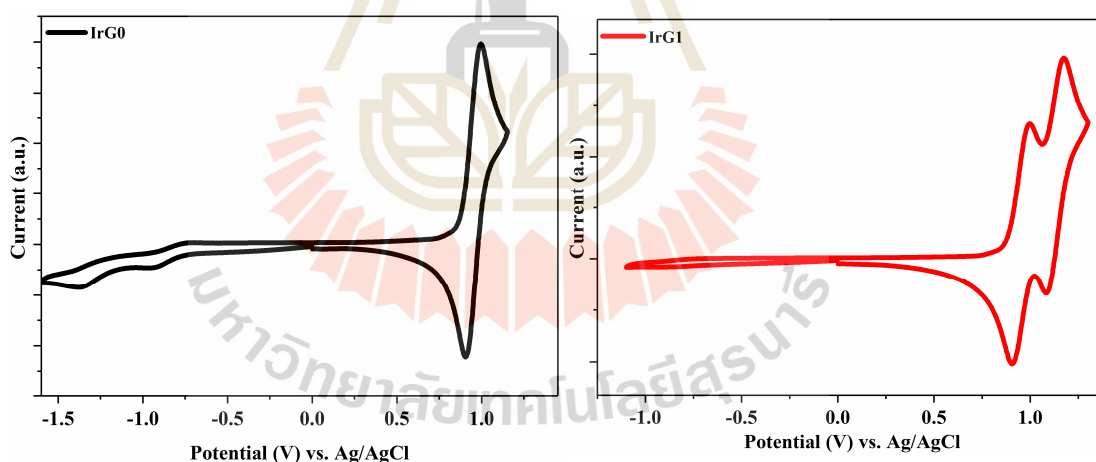


**Figure 1.41** CV curves of the complexes **IrG0-IrG3** in  $\text{CH}_2\text{Cl}_2$  solution using 0.1 M  $\text{Bu}_4\text{NPF}_6$  at a scan rate of 50 mV/s.

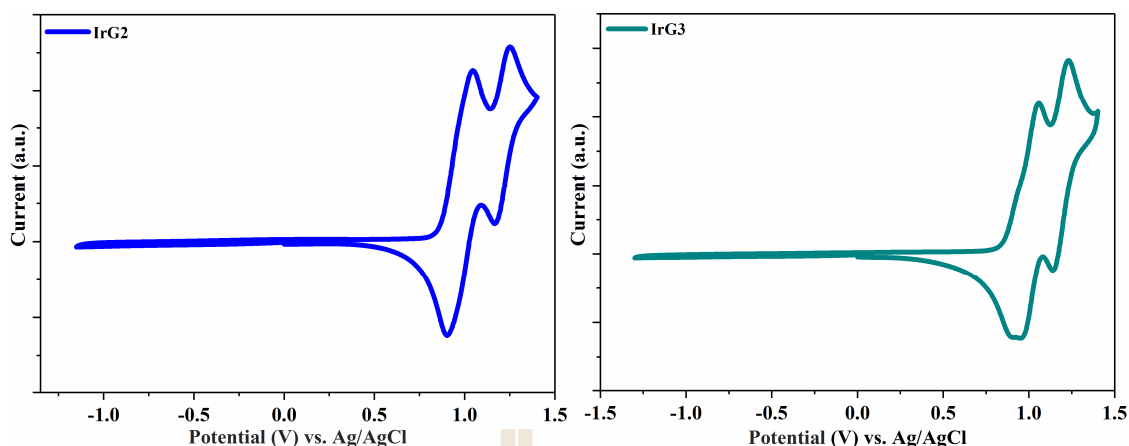


**Figure 1.41** CV curves of the complexes **IrG0-IrG3** in  $\text{CH}_2\text{Cl}_2$  solution using 0.1 M  $\text{Bu}_4\text{NPF}_6$  at a scan rate of 50 mV/s (Continued).

### 1.5.5 Thermal properties

Differential scanning calorimetry (DSC) and thermogravimetric analysis (TGA) were used to examine the thermal properties of all Ir(III) complexes in nitrogen atmosphere at a scan rate of  $10\text{ }^\circ\text{C}\cdot\text{min}^{-1}$  (Figure 1.42). From the presence of non conjugated linkage with 2, 6 and 8 dendrimer units, the onset of DSC curves of **IrG1-IrG3** display an unexpected glass-transition temperature ( $T_g$ ) to 198, 317  $^\circ\text{C}$  of **IrG1**, 218, 303  $^\circ\text{C}$  of **IrG2** and 263, 330  $^\circ\text{C}$  of **IrG3**, respectively. The enhanced  $T_g$  of **IrG1-IrG3** might arise from a higher degree of dendron rigidity derived from carbazole dendrons. It is highly desirable to attain effective end-capped solution for the Ir(III) emissive core. Their  $T_g$  values of **IrG1-IrG3** have 2 positions. This result concluded that the three complexes have 2 configuration structures. Furthermore, the thermally stable with a high decomposition temperature ( $T_d$ : at a 5% weight loss) over 222  $^\circ\text{C}$ . These results prove that the use of carbazole dendrimers as self-hosting of Ir(III) emissive core could reduce the crystallization and improve the amorphous

stability of the material and thin film. This property caused to increase the service in device operation.

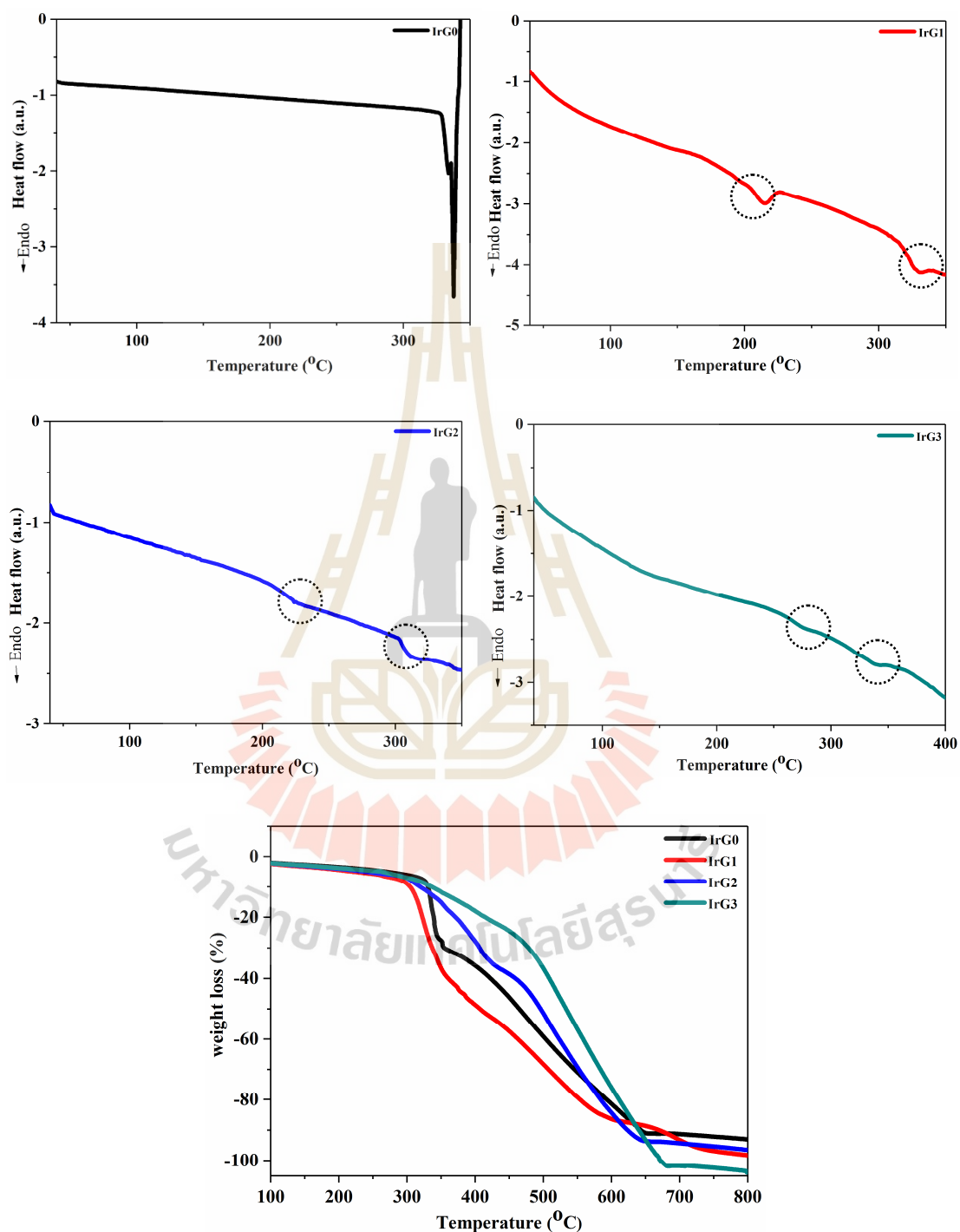


**Figure 1.42** The DSC and TGA thermograms of all complexes measured at a heating rate of  $10\text{ }^{\circ}\text{C min}^{-1}$  under  $\text{N}_2$ .

**Table 1.3** Thermal and electrochemical properties of **IrG0-IrG3**.

Comp.	T <sub>g</sub> /T <sub>d</sub> (°C) <sup>a</sup>	E <sup>ox</sup> <sub>onset</sub> (V) <sup>b</sup>	HOMO (eV) <sup>c</sup>	E <sub>g</sub> eV <sup>d</sup>	LUMO (eV) <sup>e</sup>
<b>IrG0</b>	-/269	0.87	-5.31	2.48	-2.83
<b>IrG1</b>	198, 317/222	0.86	-5.30	2.51	-2.79
<b>IrG2</b>	218, 303/240	0.85	-5.29	2.51	-2.78
<b>IrG3</b>	263, 330/265	0.85	-5.29	2.51	-2.78

<sup>a</sup> Corrected from DSC and TGA techniques at scan rate 10 °C/min.

<sup>b</sup> Measured by CV in CH<sub>2</sub>Cl<sub>2</sub> vs Ag/Ag<sup>+</sup> at a scan rate of 50 mV/s

<sup>c</sup> Calculated from onset oxidation potential HOMO = -(E<sup>ox</sup><sub>onset</sub> + 4.44) eV

<sup>d</sup> Calculated from  $\lambda^{\text{abs}}_{\text{onset}}$ ;  $E_g = 1240/\lambda^{\text{abs}}_{\text{onset}}$

<sup>e</sup> Calculated from LUMO = HOMO + E<sub>g</sub>

### 1.5.6 Quantum chemical calculation

To get further insight into the effect of molecular structures and electron distributions of the four novel Ir(III) complexes on the performances of PhOLED, their geometries and energies were optimized by density functional theory (DFT) calculations. The B3LYP/6-31G(d) method was used to calculate for the main-group atoms while the Stuttgart-Dresden ECP was employed for Ir atom. The HOMO is mainly located in electron donating groups and  $\pi$ -spacer. The LUMO is mainly located in electron withdrawing groups, Ir(III) core complex. There are effective electron separations between HOMO and LUMO of these complexes induced by light irradiation. This results support the supposed push-pull characteristics of these molecules (see in Figure 1.43).

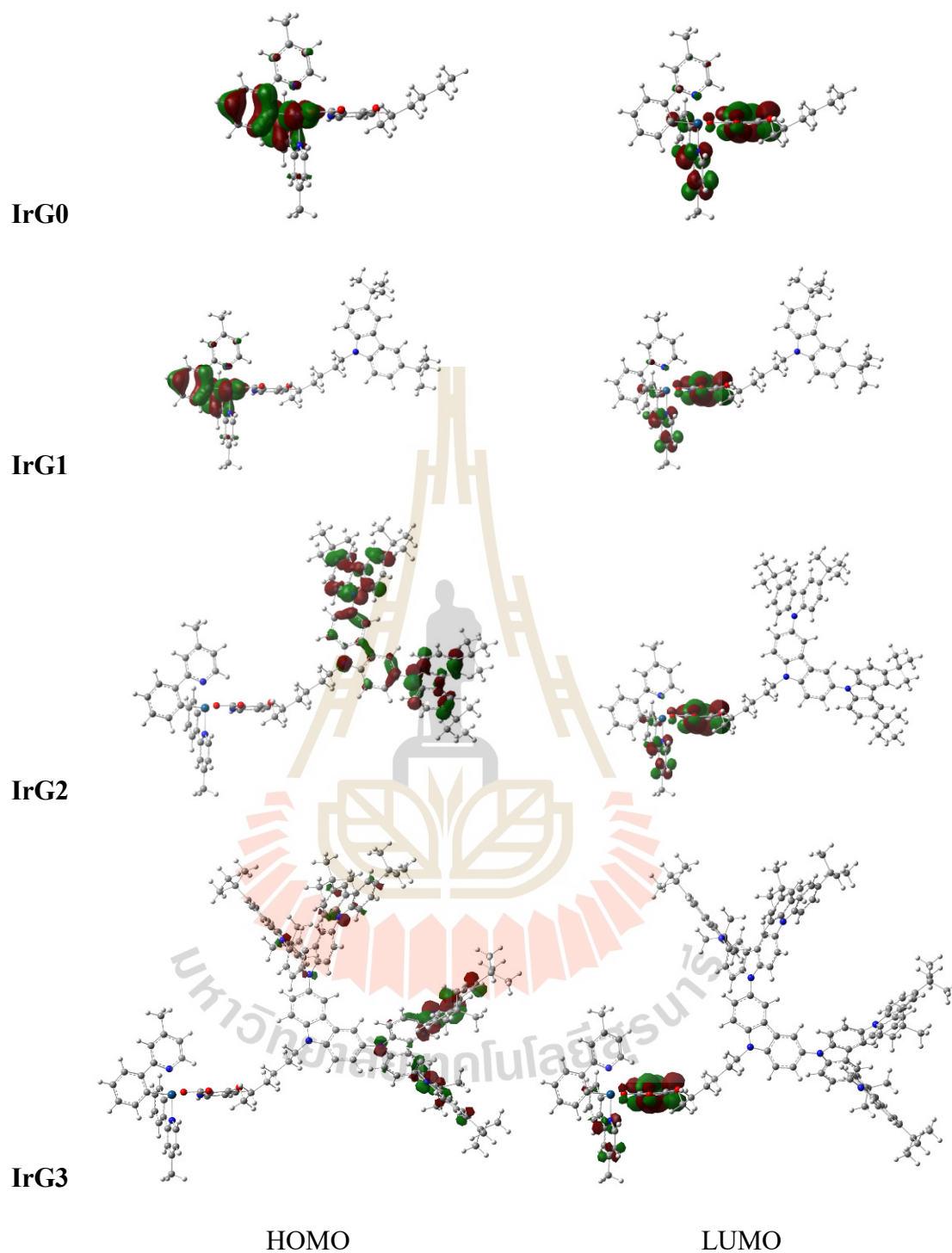


**Figure 1.43** HOMO (left) and LUMO (right) distributions of the **IrG0-IrG3** complexes by DFT B3LYP/6-31G (d) calculation.

## 1.6 Conclusions

This work has been demonstrated to construct self-hosting functional Ir(III)-cored dendrimers up to four generations on the basis of non conjugated linkage self-hosting carbazole dendrimers. Novel self-hosting Ir(III) complexes, **IrG0-IrG3**, have synthesized as emitters for phosphorescent emitter applications using Ullmann coupling, Suzuki coupling, alkylation and ligation reaction. The different type of non-conjugated carbazole moieties are introduced to the molecules and serve as self-hosting property. This moiety had small impact on optical and electrochemical as expected. Moreover, it suppressed intermolecular  $\pi$ - $\pi$  interaction on PL spectra and emission lifetime in the solid state. The novel target complexes were characterized by using NMR, IR, MALDI-TOF MS, UV-Vis and photoluminescence techniques. The complexes exhibit an absorption band cover UV and visible region. Phosphorescence spectra of the complex molecules show emission peak at yellow region ( $\lambda_{em} = 580$ -590 nm), excited at  $\lambda_{ex} = 430$  nm. **IrG0-IrG3** molecules show good thermal properties and could be formed morphologically stable amorphous thin films with glass transition temperature over 198 °C for the device fabrication process. DFT calculations have been performed on the phosphorescence molecules, and the result show that electron distribution from the whole molecules to the accepting Ir(III) core moiety occurred during the HOMO-LUMO excitation.

## 1.7 References

Adachi, C., Baldo, M.A., Thompson, M.E. and Forrest, S.R. (2011). Nearly 100% internal phosphorescence efficiency in an organic light-emitting device. **Journal of Applied Physics**. 90: 5048-5051.

- Bae, H.J., Chung, J., Kim, H., Park, J., Lee, K.M., Koh, T.-W., Lee, Y.S., Yoo, S., Do, Y. and Lee, M.H. (2014). Deep red phosphorescence of cyclometalated iridium complexes by *o*-carborane substitution. **Inorganic Chemistry**. 53: 128-138.
- Baldo, M.A., O'Brien, D.F., You, Y., Shoustikov, A., Sibley, S., Thompson, M.E. and Forrest, S.R. (1998). Highly efficient phosphorescent emission from organic electroluminescent devices. **Nature**. 395: 151-154.
- Baldo, M.A., Lamansky, S., Burrows, P.E., Thompson, M.E. and Forrest, S.R. (1999). Very high-efficiency green organic light-emitting devices based on electro phosphorescence. **Applied Physics Letters**. 75: 4-6.
- Braun, D. and Heeger, A.J. (1991). Visible light emission from semiconducting polymer diodes. **Applied Physics Letters**. 58: 1982-1984.
- Burroughes, J.H., Bradley, D.D.C., Brown, A.R., Marks, R.N., Mackay, K., Friend, R.H., Burns, P.L. and Holmes, A.B. (1990). Light-emitting diodes based on conjugated polymers. **Nature**. 347: 539-541.
- Chang, Y.-J. and Chow, T.-J. (2011). Highly efficient red fluorescent dyes for organic light-emitting diodes. **Journal of Materials Chemistry**. 21: 3091-3099.
- Chi, Y. and Chou, P.-T. (2010). Transition-metal phosphors with cyclometalating ligands: fundamentals and applications. **Chemical Society Reviews**. 39: 638-655.
- Choi, W.H., Tam, H.L., Zhu, F., Ma, D., Sasabe, H. and Ki, J. (2013). High performance semitransparent phosphorescent white organic light emitting diodes with bi-directional and symmetrical illumination. **Applied Physics Letters**. 102: 153308.

- Cho, Y.J., Yook, K.S. and Lee, J.Y. (2014). A universal host material for high external quantum efficiency close to 25% and long lifetime in green fluorescent and phosphorescent OLEDs. **Advanced Materials**. 26: 4050-4055.
- Cui, R., Zhou, L., Jiang, Y., Li, Y., Zhao, X. and Zhang, H. (2015). High performance yellow organic electroluminescent devices by doping iridium(III) complex into host materials with stepwise energy levels. **Journal of Luminescence**. 166: 259-263.
- Ding, J., Gao, J., Cheng, Y., Xie, Z., Wang, L., Ma, D., Jing, X. and Wang, F. (2006). Highly efficient green-emitting phosphorescent iridium dendrimers based on carbazole dendrons. **Advanced Functional Materials**. 16: 575-581.
- Fei, T., Cheng, G., Hu, D., Dong, W., Lu, P. and Mai Y. (2010). Iridium complex grafted to 3,6-carbazole-alt-tetraphenylsilane copolymers for blue electrophosphorescence. **Journal of Polymer Science: Part A: Polymer Chemistry**. 48: 1859-1865.
- Graber, S., Doyle, K., Neuburger, M., Housecroft, C.E., Constable, E.C., Costa, R.D., Ortí, E., Repetto, D. and Bolink, H.J. (2008). A Supramolecularly-caged ionic iridium(III) complex yielding bright and very stable solid-state light-emitting electrochemical cells. **Journal of the American Chemical Society**. 130: 14944-14945.
- Guan, Y. and Niu, L. (2009). White organic light-emitting diodes with 9, 10-bis (2-naphthyl) anthracene. **Journal of Physics: Conference Series**. 152: 1-5.

- HO, C.-L., Li, H. and Wong, W.-Y. (2014). Red to near-infrared organometallic phosphorescent dyes for OLED applications. **Journal of Organometallic Chemistry**. 751: 261-285.
- Holmes, R.J., Forrest, S.R., Tung, Y.-J., Kwong, R.C., Brown, J.J., Garon, S. and Thompson, M.E. (2003). April blue organic electrophosphorescence using exothermic host-guest energy transfer. **Applied Physics Letters**. 82: 2422-2424.
- Jiang, X., Jen, A.K.-Y., Carlson, B. and Dalton, L.R. (2001). Red electrophosphorescence from osmium complexes. **Applied Physics Letters**. 80: 713-715.
- Jiang, H. (2010). Organic ambipolar conjugated molecules for electronics: synthesis and relationships structure-property. **Macromolecular Rapid Communications**. 31: 2007-2034.
- Jou, J.-H., Lin, Y.-X., Peng, S.-H., Li, C.-J., Yang, Y.-M., Chin, C.-L., Shyue, J.-J., Sun, S.-S., Lee, M., Chen, C.-T., Liu, M.-C., Chen, C.-C. Chen, G.-Y., Wu, J.-H., Li, C.-H., Sung, C.-F., Lee, M.-J. and Hu, J.-P. (2014). Highly efficient yellow organic light emitting diode with a novel wet- and dry-process feasible iridium complex emitter. **Advanced Functional Materials**. 24: 555-562.
- Kawamura, Y., Goushi, K., Brooks, J., Brown, J.J. and Sasabe, H. (2005). 100 % quantum efficiency of Ir(III) complexes in organic semiconductor films. **Applied Physics Letters**. 86: 71104-71106.
- Kim, J.H., Chen, Y., Liu, R. and So, F. (2014). Phosphorescent dye-doped hole transporting layer for organic light-emitting diodes. **Organic Electronics**. 15: 2381-2386.

- Kokde, M.M., Buechel, M., Vulto, S.I.E., Weijer, P., Meulen Kamp, E.A., Winter, S.H.P.M., Mank, A.J.G., Vorstenbosch, H.J.M., Weijtens, C.H.L. and Elsbergen, V. (2004). Modification of PEDOT:PSS as hole injection layer in polymer LEDs. **Physica Status Solidi**. 201: 1342-1359.
- Li, Y.-L., Cheng, Y.-S., Yeh, P.-N., Liao, S.-H. and Chen, S.-A. (2014). Structure tuning of crown ether grafted conjugated polymers as the electron transport layer in bulk-heterojunction polymer solar cells for high performance. **Advanced Functional Materials**. 24: 6811-6817.
- Li, X., Zhang, D., Chi, H., Xiao, G., Dong, Y., Wu, S., Su, Z., Zhang, Z., Lei, P., Hu, Z. and Li, W. (2010). Reduced efficiency roll-off in electrophosphorescent devices by a short-living rhenium emitter with well-matched energy levels. **Applied Physics Letters**. 97: 263301-263303.
- Li, Z. and Meng, H. (2006). Organic light-emitting materials and devices. **Optical Science and Engineering**. 1-672.
- Lo, S.-C., Namdas, E.B., Burn, P.L. and Samuel, I.D.W. (2003). Synthesis and properties of highly efficient electroluminescent green phosphorescent Iridium cored dendrimers. **Macromolecules**. 36: 9721-9730.
- Lo, S.-C., Richards, G.J., Markham, J.P.J., Namdas, E.B., Sharma, S., Burn, P.L. and Samuel, I.D.W. (2005). A light blue phosphorescent dendrimer for efficient solution-processed light-emitting diodes. **Advanced Functional Materials**. 15: 1451-1458.
- Lo, S.-C., Namdas, E.B., Shipley, C.P., Markham, J.P.J., Anthopolous, T.D., Burn, P.L. and Samuel, I.D.W. (2006). The synthesis and properties of iridium cored dendrimers with carbazole dendrons. **Organic Electronics**. 7: 85-98.

- Mahon, J.K., Zhou, T.X., Burrows, P.E., Forrest, S.R. and Thompson, M.E. (1998). Small-molecule organic light emitting devices in flat panel display applications, light-emitting diodes: research, manufacturing, and applications. **SPIE Proceedings**. 3279: 87-92.
- Steven, C.F.K., Chow, P.K., Cheng, G., Kwok, C.-C., Kwong, C.L., Low, K-H. and Che, C.-M. (2013). Robust phosphorescent platinum(II) complexes with tetradentate O<sup>N</sup>C<sup>N</sup> ligands: high efficiency OLEDs with excellent efficiency stability. **Chemical Communications**. 49: 1497-1499.
- Tang, C.W. and Vanslyke, S.A. (1987). Organic electroluminescent diodes. **Applied Physics Letters**. 51: 913-915.
- Thejokalyani, N. and Dhoble, S.J. (2014). Novel approaches for energy efficient solid state lighting by RGB organic light-emitting diodes. **Renewable and Sustainable Energy Reviews**. 32: 448-467.
- Wang, Y., Herron, N., Grushin, V.V., LeCloux, D. and Petrov, V. (2001). Highly efficient electroluminescent materials based on fluorinated organometallic iridium compounds. **Applied Physics Letters**. 79: 449-451.
- Wang, R., Liu, D., Ren, H., Zhang, T., Yin, H., Liu, G. and Li, J. (2011). Highly efficient orange and white organic light-emitting diodes based on new orange iridium complexes. **Advanced Materials**. 23: 2823-2827.
- Wang, X., Wang, S., Ma, Z., Ding, J., Wang, L., Jing, X. and Wang, F. (2014). Solution-processible 2,2'-dimethyl-biphenyl cored carbazole dendrimers as universal hosts for efficient blue, green, and red phosphorescent OLEDs. **Advanced Functional Materials**. 24: 3413-3421.

- Wang, Y., Wang, S., Zhao, N., Gao, B., Shao, S., Ding, J., Wang, L., Jina, X. and Wanga, F. (2015). Facile synthesis of self-host functional iridium dendrimers up to the fourth generation with *N*-phenylcarbazole-based polyether dendrons for non-doped phosphorescent organic light-emitting diodes. **Polymer Chemistry**. 6: 1180-1191.
- Wyckhoff, R. (1963). Crystalstructures. **NewYork:Wiley**. 1: 28.
- Xia, D., Wang, B., Chen, B., Wang, S., Zhang, B., Ding, J., Wang, L., Jing, X. and Wang, F. (2014). Self-host blue-emitting iridium dendrimer with carbazole dendrons: nondoped phosphorescent organic light-emitting diodes. **Angewandte Chemie International Edition**. 53: 1048-1052.
- Xu, H., Chen, R., Sun, Q., Lai, W., Su, Q., Huang, W. and Liu, X. (2014). Recent progress in metal-organic complexes for optoelectronic applications. **Chemical Society Reviews**. 43: 3259-3302.
- Xiao, L., Chen, Z., Qu, B., Luo, J., Kong, S., Gong, Q. and Kido, J. (2011). Recent progresses on materials for electrophosphorescent organic light-emitting devices. **Advanced Materials**. 23: 926-952.
- Yersin, H. (2004). Triplet emitters for OLED applications mechanisms of exciton trapping and control of emission properties. **Topics in Current Chemistry**. 241: 1-26.

# CHAPTER II

## SYNTHESIS AND CHARACTERIZATION OF BLUE THERMALLY ACTIVATED DELAYED FLUORESCENT EMITTERS

### 2.1 Introduction

Thermally Activated Delayed Fluorescent (TADF) emitters are the third generation of OLEDs. TADF are an attractive class of functional materials that have witnessed a booming development in recent years. Since Adachi et al. reported high performance TADF devices in 2012 (Uoyama et al., 2012), there have been many reports regarding the design and synthesis of new TADF emitters. TADF has high internal quantum efficiency of 100% because it can harvest both singlet and triplet excitons. In principle, when the energy difference ( $\Delta E_{ST}$ ) between the lowest singlet state ( $S_1$ ) and the lowest triplet state ( $T_1$ ) is small ( $< 1$  eV), reverse intersystem crossing (RISC) can take place even in pure aromatic organic compounds containing no heavy metals shown in Figure 2.1. To obtain a small  $\Delta E_{ST}$  for efficient TADF emitters, the molecular structure design strategy was present with a twisted electron donor-acceptor (D-A) structure. This structure designed resulted to the separation between the highest occupied (HOMO) and lowest unoccupied molecular orbitals (LUMO) which is considered to be an important factor in realization of the small  $\Delta E_{ST}$ . To date, several type of TADF emitters have been reported. Clearly the key

point of material development is identifying materials emitting pure red, green and blue colors with excellent emission efficiency.

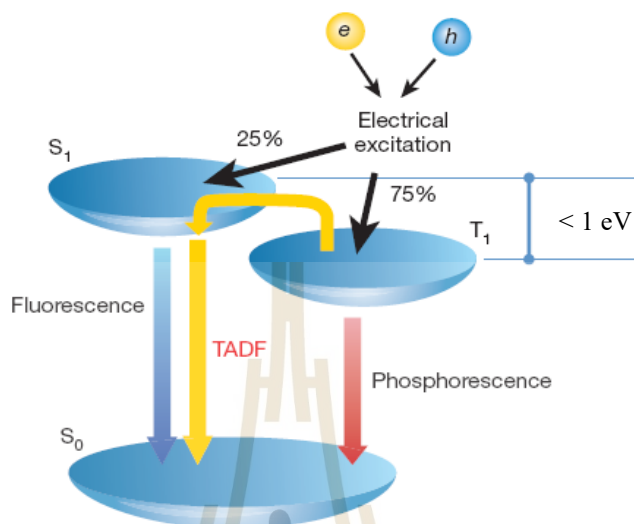


**Figure 2.1** Energy diagram of a conventional organic molecule.

### 2.1.1 Blue TADF emitters

Although many significant progresses in red and green emitters are reported, blue emitters need the further improvement due to their intrinsic wide energy band gap ( $E_g$ ). Moreover, efficient and stable deep blue TADF emitters are still difficult to obtain. Recently reported TADF emitters may provide an opportunity to solve the problem of blue OLEDs. **4TCzBN** and **t4CzIPN** are example of blue TADF molecules (Figure 2.2). Both compounds were synthesized to develop high-efficiency solution-processed TADF devices by modifying this compound with *tert*-butyl group to improve the solubility of the TADF dopant material in aromatic solvents (Cho et al., 2014).

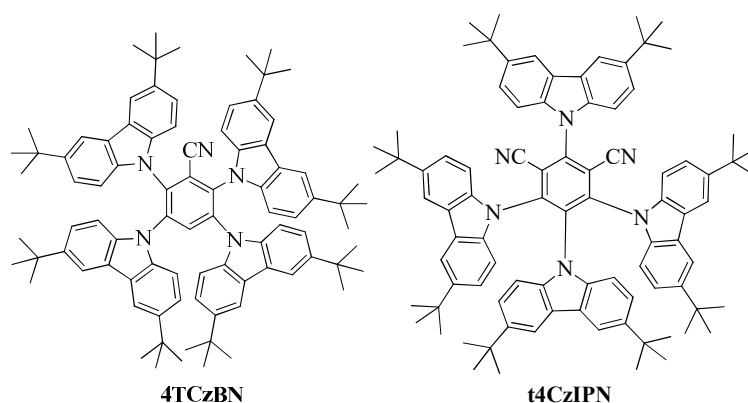


**Figure 2.2** Chemical structures of blue TADF emitters (4TCzBN and t4CzIPN).

### 2.1.2 Green TADF emitters

There has been much progress in the EQE of the red, green, blue TADF devices for recently year. The most significant advances were made in the green TADF devices because of the relatively easy molecular design of the green TADF emitters. Shuzu's group (Shuzu et al., 2015) developed green TADF emitters, **DACQ** and **PXZQ**, (Figure 2.3) with an electron donor containing carbazolyl and diphenylamino groups by carefully controlling its electron-donating ability. These molecules exhibit high photoluminescence and electroluminescence efficiencies, comparable to those of the highly twisted TADF emitters containing electron-accepting unit.

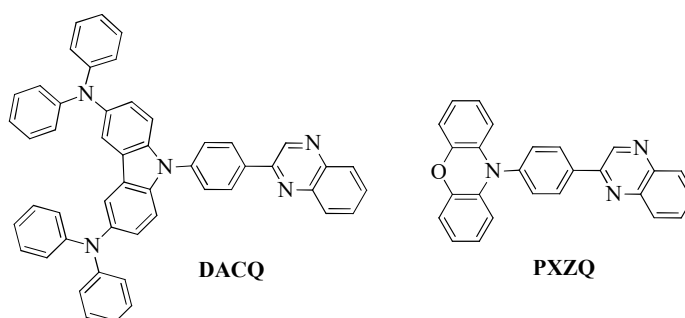


**Figure 2.3** Chemical structures of green TADF emitters.

### 2.1.3 Red TADF emitters

As you know, thermally activated delayed fluorescent (TADF) emitters can be a candidate as the pure organic based high efficiency emitters. The EQE of the red TADF device now is not as high as that of green or blue TADF devices due to lack of strong electron acceptor for the red TADF emitters. In addition, the development of the red TADF emitters was relatively difficult due to the exciton loss mechanism of the energy gap law. Therefore, many studies have demonstrated to synthesize new red TADF emitters. **6AcBIQ** (Yun and Lee, 2017) and **TPA-QCN** (Li et al., 2017) are the red TADF example. They have very low  $\Delta E_{ST}$  and show high quantum efficiency (Figure 2.4).

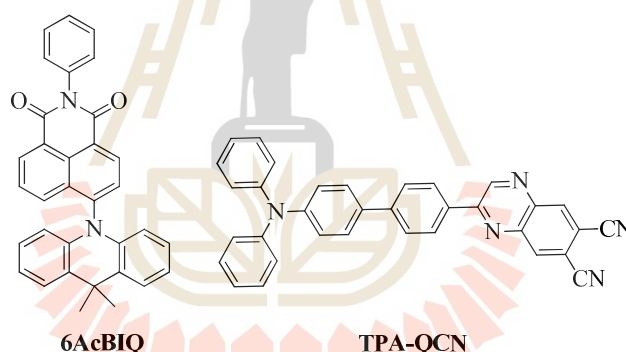


**Figure 2.4** Chemical structures of red TADF emitters.

## 2.2 Literature reviews of thermally activated delayed fluorescent (TADF) emitters

Theoretically, the internal quantum efficiency of thermally activated delay fluorescence (TADF) can approach 100% because of the contributions of both singlet and triplet excitons. Several excellent reviews on the TADF emitter molecules and devices have appeared during the past few years. Herein, we highlight the recent

advances in the development of high performance OLEDs using organic compounds as TADF emitters for multicolor displays over a wide range of wavelengths.

Zhang and co-workers (2012) reported a new blue carbazole/sulfone derivative based on TADF materials in both solutions and doped films. All molecules show very high external quantum efficiency (EQE) of nearly 10% at low current density.

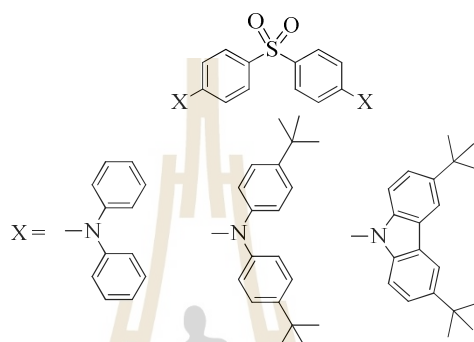


**Figure 2.5** The structure of carbazole/sulfone series based on TADF emitters.

Wu and co-workers (2014) designed a highly efficiency deep-blue TADF (DMOC-DPS). This molecule was introduced methoxy groups, which are electron-rich, into the carbazole units of a carbazole/sulfone derivative.  $\Delta E_{ST}$  was decreased to 0.21 eV with a relatively short lifetime 127  $\mu$ s in an organic thin film. OLED based on this deep blue TADF emitter exhibits a high EQE above 9% at a brightness of 100  $\text{cd}/\text{m}^2$ .

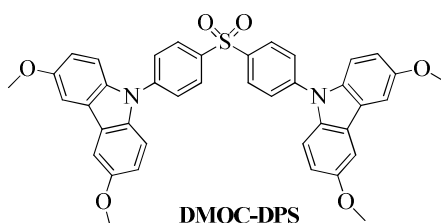


**Figure 2.6** The molecular structure of deep blue TADF emitters (DMOC-DPS).

Zhang and co-workers (2014) synthesized a blue OLED containing a 9,10 dihydrocridine/diphenylsulfone derivative that has a comparable performance to today's best phosphorescent OLEDs. The device offers an EQE of 19.5% and reduced efficiency roll-off characteristics at high luminance.

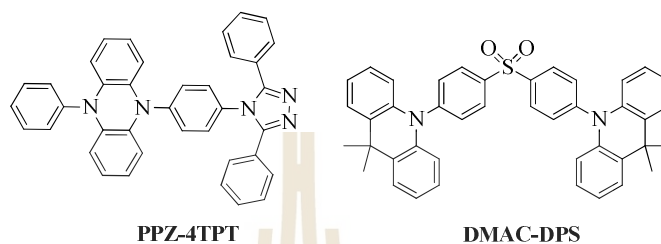


**Figure 2.7** The molecular structures of **PPZ-4TPT** and **DMAC-DPS** TADF emitters.

Moonsin and co-workers (2014) reported a series of bifunctional oligofluorene-cored carbazole dendrimers (**G<sub>n</sub>F<sub>m</sub>**,  $n = 1-3$ ,  $m = 2-3$ ) containing carbazole dendrons up to the third generation as end-caps. All non-doped solution-processed showed a blue-light emitter and hole transporter properties for organic light-emitting diodes (OLEDs). They found that **G3F2** exhibits highest EQE of 0.24% with a low turn on voltage of 2.4 V on blue light emitter and hole transport properties.

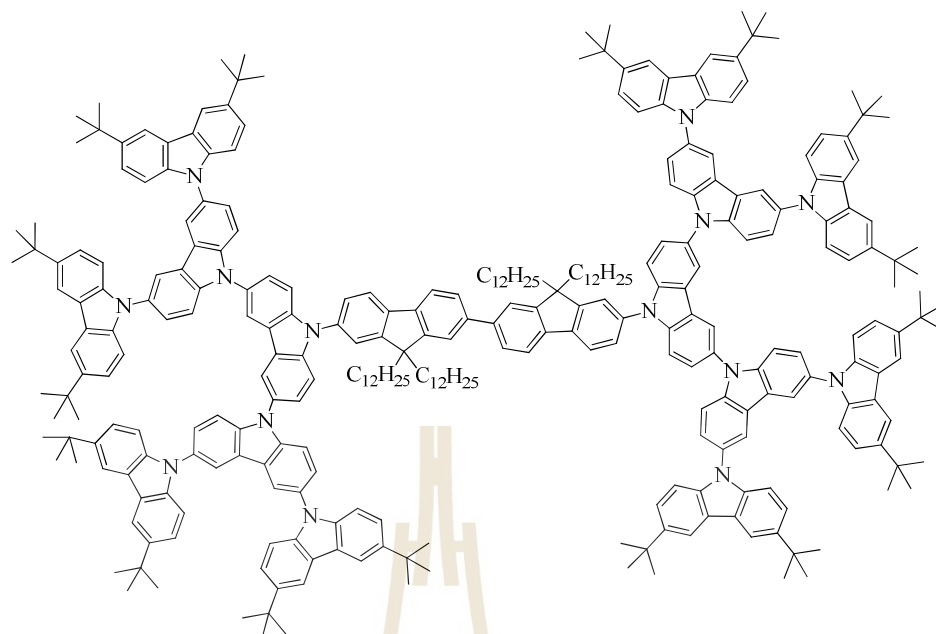


**Figure 2.8** The molecular structure of **G3F2** molecule.

Prachumrak and co-workers (2013) reported the synthesis of carbazole dendrons (**G1-G3**) of bis[5-(fluorene-2-yl)thiophen-2-yl]benzothiadiazole end-capped compound. They found that all compounds showed high glass transition temperature as high as 283 °C. In addition, these moieties were able to reduce the crystallization and retained the high emissive ability of a planar fluorescent core in the solid state as well as improve the thermal stability of the materials.

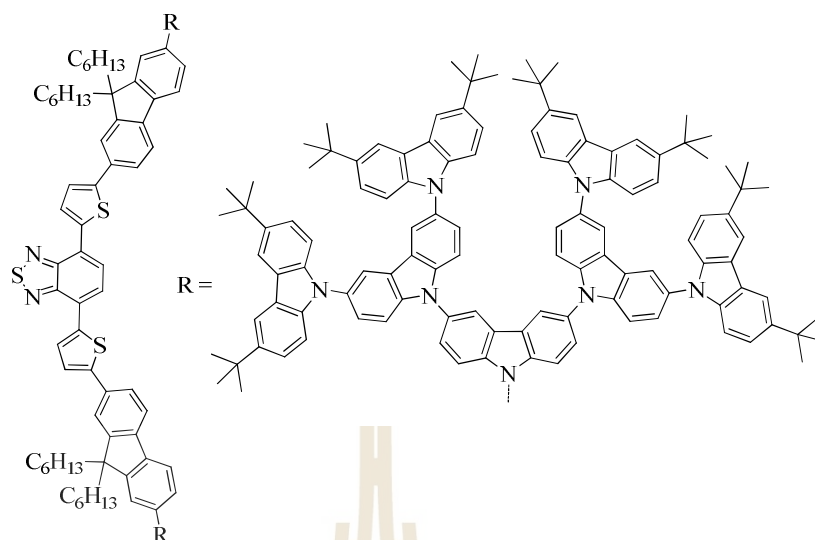


**Figure 2.9** The structure of the red-light emitting dendrimers (9C).

Li and co-worker (2017) reported the non-doped blue TADF emitters composed of diphenylsulfone core and oligo-carbazole dendrons. The compounds exhibited a reduced singlet triplet energy gap ( $\Delta E_{ST}$ ) with increasing the dendron generation. **G2** device achieved deep-blue light with emission peak at 428 nm, a CIE coordinate at (0.15, 0.12). All TADF molecules show high thermal and amorphous stabilities and good solution process ability.

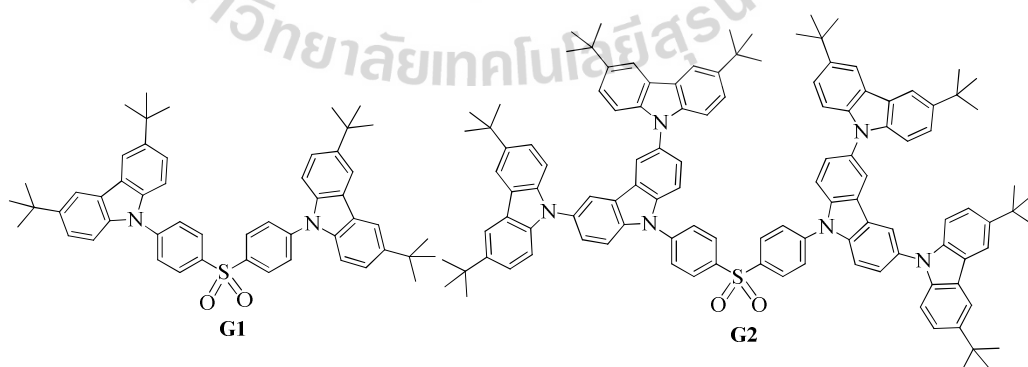


**Figure 2.10** The molecular structure of non-doped blue TADF dendrimers.

To date, several type of TADF (red, green and blue) light emitting dendrimers have been reported. Blue emitting TADF materials with carbazole dendron moieties has been investigated and synthesized (Li et al., 2017) because of their good thermal and photoluminescent (PL) properties. However, those have still some troubles due to their wide energy band gap ( $E_g$ ). it is very difficult to find good host materials.

In this chapter, we reported on three novel blue TADF materials (**FSG1-FSG3**). All materials were designed to allow the dopant materials to be soluble in aromatic solvents. The carbazole moiety of all TADF molecules was modified with *tert*-butyl units up to third generation. We also studied all novel blue TADF molecules on physical and electrochemical with increasing the number of carbazole dendrimers.

### 2.3 Aims of the study

Due to high molar extinction coefficients and to give better performance of new blue TADF emitters, we have designed the novel self-hosting blue TADF with diphenyl sulfone as an accepting blue emissive core. Molecule **2**, **6** and **8** carbazole dendrons are used to investigate the TADF and self-hosting effects acted as an electron donating and host moiety. Therefore, the objectives of this chapter are the following:

1. To synthesize new blue TADF materials containing carbazole dendrons up to three generations.
2. To characterize the synthesized target TADF emitters by NMR, IR, UV-Vis and photoluminescence spectroscopy techniques.

3. To study the effect of the number of carbazole dendritic generation on the physical and electronic optical properties of these novel TADF emitting materials, as well as their photovoltaic properties.

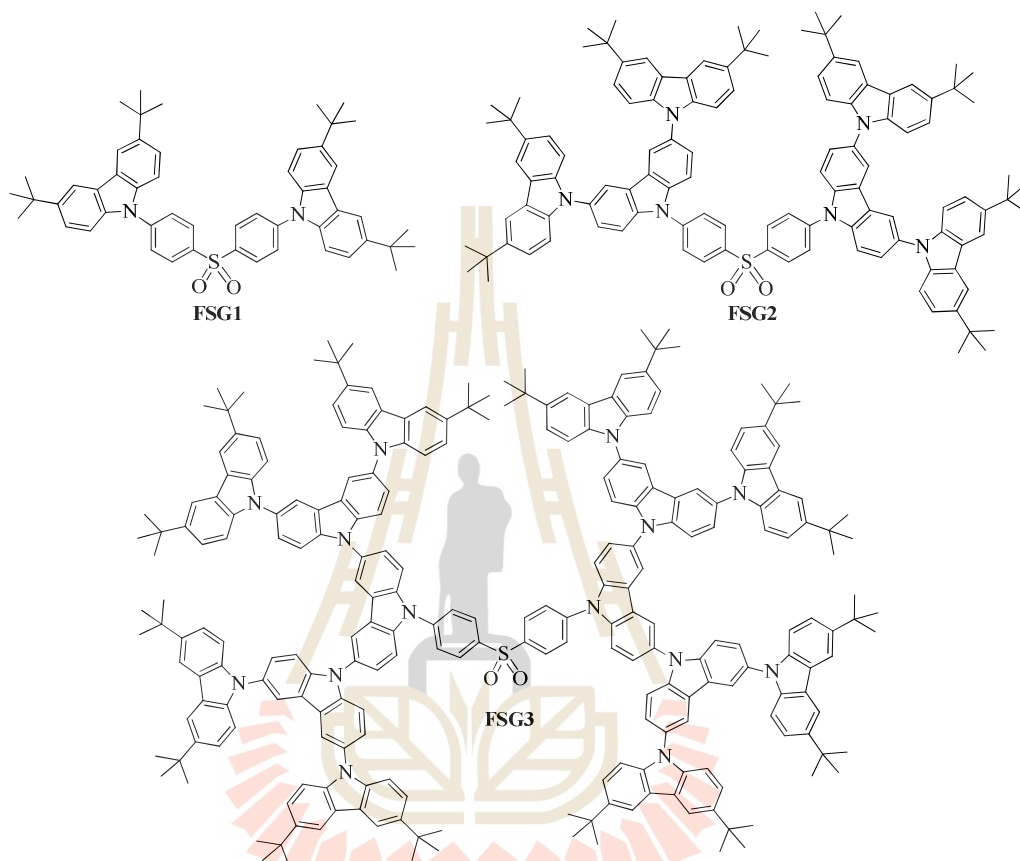


**Figure 2.11** The designed self-hosting TADF emitters (FSG1, FSG2 and FSG3).

## 2.4 Materials and methods

All reactions were performed under a nitrogen atmosphere and no special precautions were required during workup. All solvents were carefully dried and distilled from appropriate drying agents prior to use. Commercially available reagents were used without further purification unless otherwise stated. All reactions were monitored by thin-layer chromatography (TLC) with Silicycle pre-coated aluminum

plates. Flash column chromatography of all compounds was carried out using silica gel (230-400 mesh) as stationary phase and commercial organic solvents as eluent.

#### 2.4.1 Materials

All chemicals used in this chapter were analytical grade as shown in

Table 2.1

**Table 2.1** Chemicals of Chapter II.

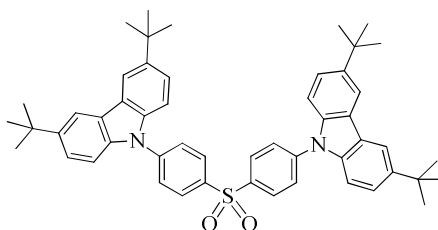
Chemicals	Formula	Grade	Manufacturer
Bis (4-fluorophenyl) sulfone	(FC <sub>6</sub> H <sub>4</sub> ) <sub>2</sub> SO <sub>2</sub>	99%	Acros
Calcium hydride	CaH <sub>2</sub>	93%	Acros
Dichloromethane	CH <sub>2</sub> Cl <sub>2</sub>	99.9%	CARLO ERBA
Dimethylformamide	C <sub>3</sub> H <sub>7</sub> NO	99.9%	CARLO ERBA
Magnesium sulfate	MgSO <sub>4</sub>	99%	Fluka
Methyl alcohol	CH <sub>4</sub> O	99.9%	CARLO ERBA
Sodium hydride	NaH	60%	Aldrich
Sodium sulfate	Na <sub>2</sub> SO <sub>4</sub>	99%	CARLO ERBA
Tetrahydrofuran	C <sub>4</sub> H <sub>8</sub> O	99.5%	CARLO ERBA
Toluene	C <sub>7</sub> H <sub>8</sub>	ISO for analysis	CARLO ERBA

#### 2.4.2 Characterization techniques

The structure of intermediate and TADF emitters were characterized by <sup>1</sup>H-NMR, <sup>13</sup>C-NMR, MALDI-TOF, melting point and FTIR techniques. The optical and electrical properties of all TADF emitters were characterized by UV-Visible spectroscopy, fluorescence spectroscopy, and cyclic voltammetry, respectively. The details of methods were presented as previous chapter

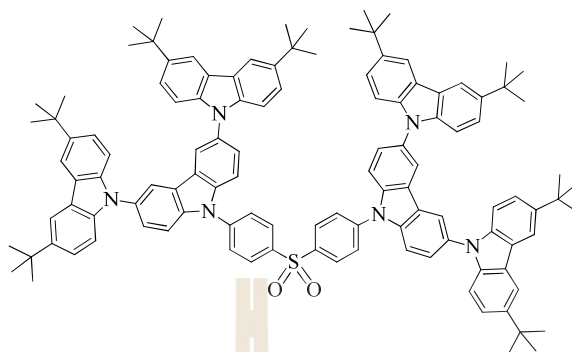
### 2.4.3 Synthesis methods

#### 9,9'-(Sulfonylbis(4,1-phenylene))bis(3,6-di-*tert*-butyl-carbazole) (FSG1)



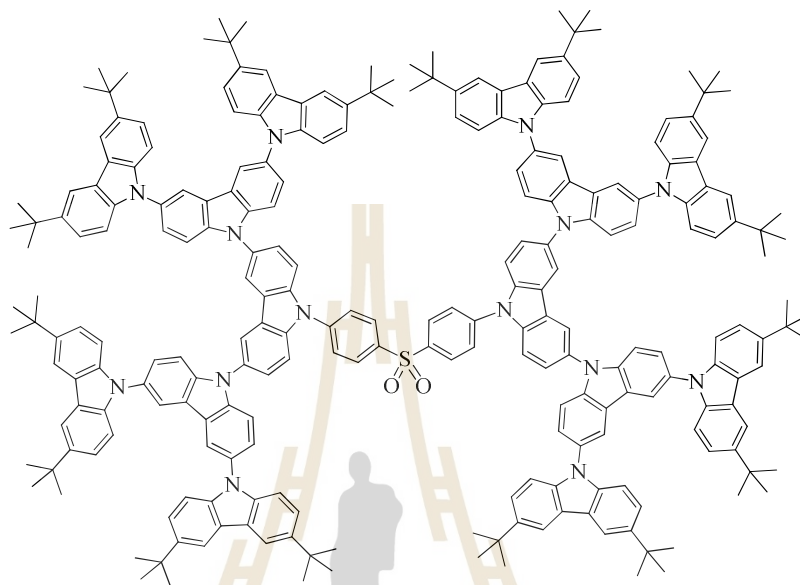
NaH (0.03 g, 1.41 mmol) was slowly added into a mixed solution of **2** (0.27 g, 0.97 mmol) in dehydrated DMF 20 ml. After the solution was stirred at room temperature for 1 h, bis(4-fluorophenyl) sulfone (0.12 g, 0.47 mmol) in dehydrated DMF was added, following which the mixture was stirred at 100 °C for 1 h. After cooling, the mixture was poured into 20 ml of water, and the white precipitate was filtered and dried. The crude product was recrystallized from dichloromethane-methanol to produce white solid compound (0.20 g, 67%); m.p. 273-275 °C; <sup>1</sup>H-NMR (600 MHz, CDCl<sub>3</sub>): δ 8.23 (d, *J* = 8.6 Hz, 4H), 8.12 (s, 4H), 7.81 (d, *J* = 8.6 Hz, 4H), 7.46 (d, *J* = 8.6 Hz, 4H), 7.43 (d, *J* = 8.6 Hz, 4H), 1.45 (s, 36H) ppm; <sup>13</sup>C-NMR (151 MHz, CDCl<sub>3</sub>): δ 144.12, 143.24, 138.82, 138.29, 129.61, 126.56, 124.12, 124.00, 116.51, 109.18, 34.79, 31.93 ppm; FTIR 3065, 2962, 2869, 1593, 1495, 1470, 1325, 1157, 1107 cm<sup>-1</sup>; MALDI-TOF (m/z) [M<sup>+</sup>] calcd for C<sub>52</sub>H<sub>56</sub>N<sub>2</sub>O<sub>2</sub>S: 772.4062, found: 772.1589.

9,9''''-(Sulfonylbis(4,1-phenylene))bis(3,3''',6,6''-tetra-*tert*-butyl-9,3':6',9''-tercarbazole) (**FSG2**)



NaH (0.01 g, 0.47 mmol) was slowly added to a solution of **6** (0.25 g, 0.35 mmol) in a mixture of dehydrated 1:2 THF-DMF 30 ml and stirred at room temperature for 30 min. The solution was heated up to 60 °C and bis(4-fluorophenyl)sulfone (0.12 g, 0.47 mmol) in dehydrated DMF was then added in the mixture under argon. The mixture was stirred at 60 °C for 3 h. After cooling, the mixture was poured into 20 ml of water, extracted with dichloromethane and dried with anhydrous sodium sulfate. The crude product was purified by column chromatography using dichloromethane-hexane as eluents. The product was recrystallized from dichloromethane-methanol to produce white solid compound (0.10 g, 38%); m.p. 293-295 °C;  $^1\text{H-NMR}$  (600 MHz,  $\text{CDCl}_3$ ):  $\delta$  8.43 (d,  $J = 8.6$  Hz, 4H), 8.24 (s, 4H), 8.15 (s, 8H), 8.03(d,  $J = 8.6$  Hz, 4H), 7.73 (d,  $J = 8.7$  Hz, 4H), 7.65(dd,  $J = 8.7, 1.9$  Hz, 4H), 7.43(dd,  $J = 8.7, 1.9$  Hz, 8H), 7.31 (d,  $J = 8.6$  Hz, 8H), 1.45 (s, 72) ppm;  $^{13}\text{C-NMR}$  (151 MHz,  $\text{CDCl}_3$ ):  $\delta$  142.80, 142.43, 140.10, 139.97, 139.42, 131.99, 130.15, 127.45, 126.30, 124.77, 123.64, 123.25, 119.53, 116.30, 110.98, 108.96, 34.74, 32.03 ppm; FTIR 3052, 2954, 2861, 1738, 1593, 1490, 1325, 1262, 1162, 1102  $\text{cm}^{-1}$ ; MALDI-TOF (m/z) [ $\text{M}^+$ ] calcd for  $\text{C}_{116}\text{H}_{116}\text{N}_6\text{O}_2\text{S}$ : 1657.8914, found: 1657.9654.

9,9''''-(Sulfonylbis(4,1-phenylene))bis(3,3''',6,6''''-tetra-*tert*-butyl-6'-(3-(*tert*-butyl)-6-isopropyl-carbazol-9-yl)-6''-(3,6-di-*tert*-butyl-carbazol-9-yl)-9,3':9',3'':6',9''':3''',9''''-quinquecarbazole) (**FSG3**)



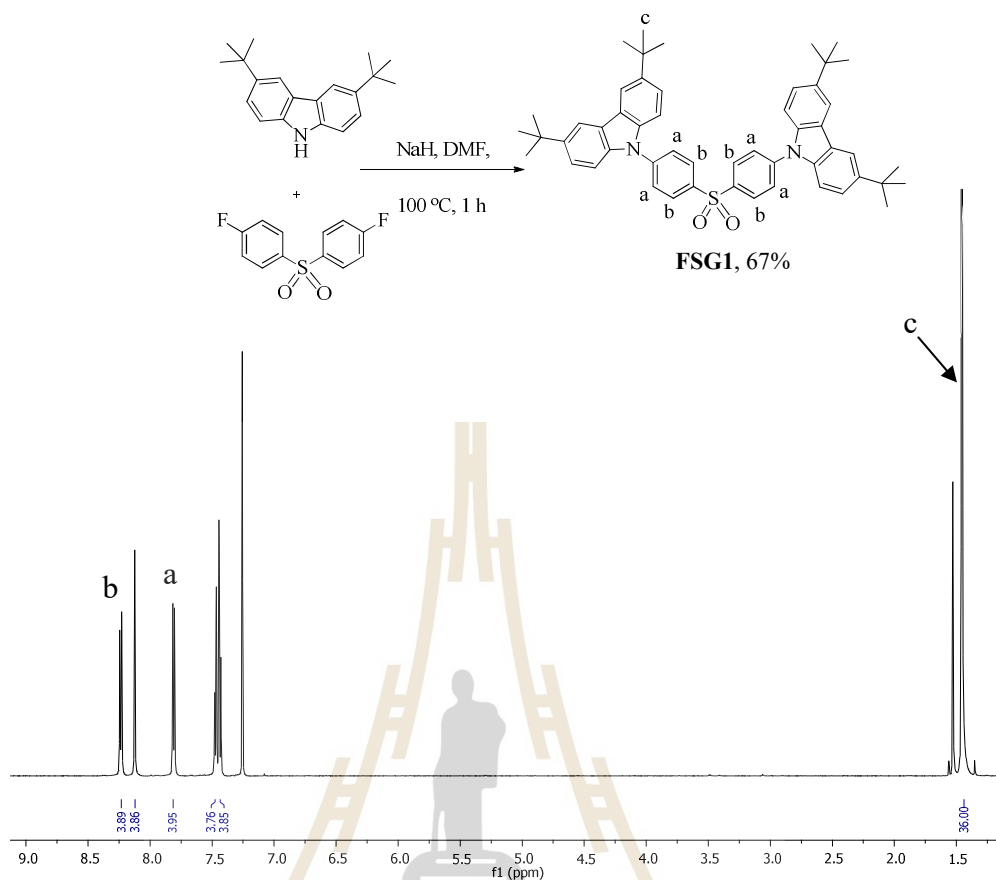
NaH (0.01 g, 0.33 mmol) was slowly added to a mixture of **8** (0.40 g, 0.23 mmol) in dehydrated 1:2 THF-DMF mixture 45 ml at room temperature. The solution was stirred and heated up to 60 °C and bis(4-fluorophenyl)sulfone (0.03 g, 0.11 mmol) in dehydrated DMF was then added under argon. The mixture was stirred at 60 °C for 2 days. After cooling, the mixture was poured into 20 ml of water, extracted with dichloromethane and dried with anhydrous sodium sulfate. The crude product was purified by column chromatography using dichloromethane-hexane as eluents. The product was recrystallized from dichloromethane-methanol to produce white solid compound (0.13 g, 34%); m.p. > 350 °C; <sup>1</sup>H-NMR (600 MHz, CDCl<sub>3</sub>): δ 8.56 (s, 4H), 8.54 (d, *J* = 8.4 Hz, 4H), 8.26 (d, *J* = 1.4 Hz, 8H), 8.14 (d, *J* = 3.6 Hz, 20H), 7.92-7.88 (m, 8H), 7.63-7.53 (m, 16H), 7.43 (d, *J* = 8.3 Hz, 16H), 7.31 (d, *J* = 6.6 Hz, 16H), 1.44 (s, 144H) ppm; <sup>13</sup>C-NMR (151 MHz, CDCl<sub>3</sub>): δ 142.61, 141.20, 140.17, 130.97, 126.09, 123.91, 123.56, 123.14, 119.50, 116.24, 110.91, 109.05, 34.72, 32.03

ppm; FTIR 3044, 2954, 2861, 1731, 1585, 1485, 1322, 1262, 1229, 1157, 1031  $\text{cm}^{-1}$ ;  
MALDI-TOF ( $m/z$ ) [ $M^+$ ] calcd for  $\text{C}_{244}\text{H}_{234}\text{N}_{14}\text{O}_2\text{S}$ : 3427.8584, found:3427.4359.

## 2.5 Results and discussion

### 2.5.1 Synthesis

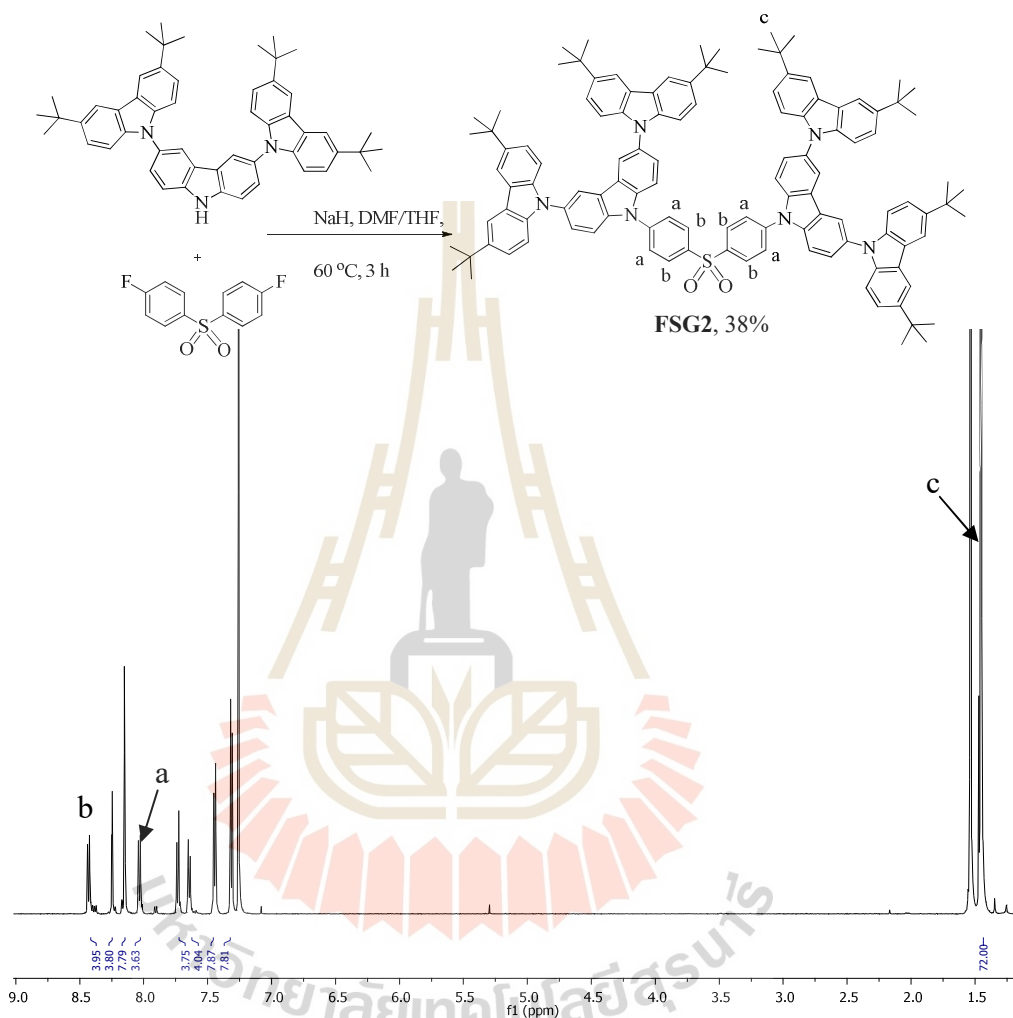
Figure 2.12 shows the synthesis of the first designed thermally activated delayed (TADF) emitters; **FSG1** and  $^1\text{H}$ -NMR spectrum. For the synthesis, **FSG1** was formed from the C-N coupling reaction between 4,4'-sulfonylbis (fluorobenzene) and **2** in the presence of sodium hydride (NaH) as base in dimethyl formamide as a solvent to give 9,9'-(sulfonylbis(4,1-phenylene))bis(3,6-di-*tert*-butyl-9H-carbazole) in 67% yield. The chemical structure of compound **FSG1** was confirmed by  $^1\text{H}$ -NMR, IR spectroscopy as well as MALDI-TOF MS. The  $^1\text{H}$ -NMR spectrum collected in  $\text{CDCl}_3$  show a singlet signal at 1.46 ppm (36H) assigned to two side of *tert*-butyl group substituent on **2** and the N-H proton signal of starting **2** at 7.84 ppm (1H) completely disappeared. Furthermore, the proton signal at aromatic region was found at chemical shift 8.23 ppm (4H) and 7.81 ppm (4H) resulting in the proton signal of diphenyl sulfone part. The number of proton between diphenyl sulfone and *tert*-butyl parts is 4:4:36 corresponding to two side of the dendron **2** substituent compared to one side 2:2:2:2:18 ratio. The IR spectrum of **FSG1** was observed the vibration around 1325 and 1157  $\text{cm}^{-1}$  due to 2 (S=O stretching) of diphenyl sulfone moieties. In addition, MALDI-TOF MS spectrum was used to confirm the structure and found to be 772.1589  $m/z$ , calculated for  $\text{C}_{52}\text{H}_{56}\text{N}_2\text{O}_2\text{S}$ : 772.4062.



**Figure 2.12** The synthesis and  $^1\text{H-NMR}$  spectrum in  $\text{CDCl}_3$  of **FSG1**.

The synthesis of **FSG2** and  $^1\text{H-NMR}$  spectra are shown in Figure 2.13. The synthesis of **FSG2** was used the similar condition reaction with the **FSG1** synthesis. Time to synthesize are increased from 1 h to 3 h and changed to DMF/THF mixed solvents based on the solubility of **6** to obtain **FSG2**; 9',9''-(sulfonylbis(4,1-phenylene))bis(3,3'',6,6''-tetra-*tert*-butyl-9,3':6',9''-tercarbazole) in 38% yield. The structure was confirmed clearly by  $^1\text{H-NMR}$ , IR spectroscopy as well as by MALDI-TOF MS. The  $^1\text{H-NMR}$  spectrum shows similar pattern with those of **FSG1** but the number of proton between diphenyl sulfone at chemical shift 8.43 and 8.03 ppm and *tert*-butyl part at chemical shift 1.45 ppm is to be 4:4:72 corresponding to two side of the dendron **6** substituent.

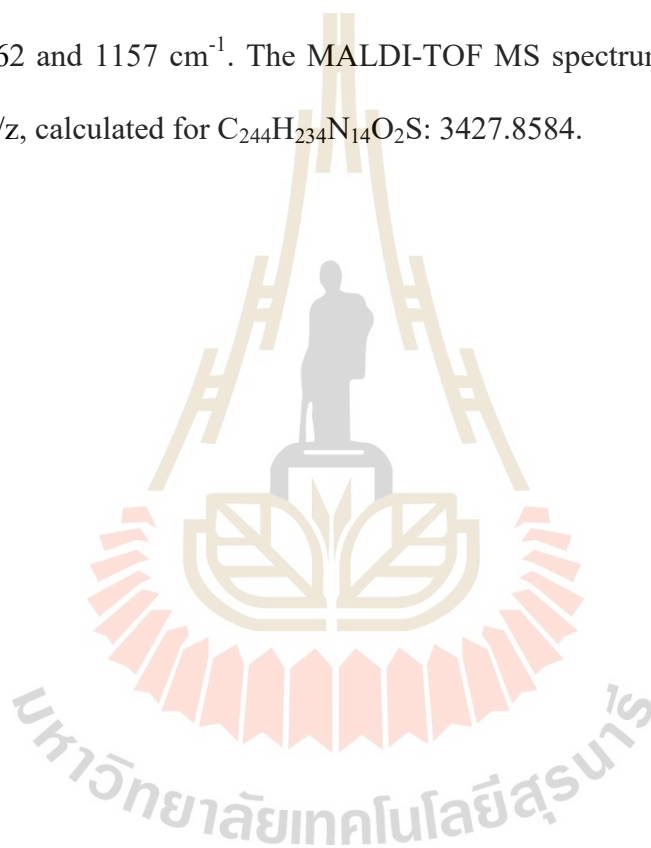
The IR spectrum result was observed the vibration of 2 (S=O stretching) of diphenyl sulfone moieties at around 1262 and 1162  $\text{cm}^{-1}$ . The MALDI-TOF MS spectrum was observed to be 1657.8914  $m/z$ , calculated for  $\text{C}_{116}\text{H}_{116}\text{N}_6\text{O}_2\text{S}$ : 1657.8914.



**Figure 2.13** The synthesis and  $^1\text{H-NMR}$  spectrum in  $\text{CDCl}_3$  of **FSG2**.

The synthesis of **FSG3** and  $^1\text{H-NMR}$  spectrum are showed in Figure 2.14. For the synthesis, the condition reaction is also similar condition with the **FSG1** synthesis, while time to synthesize are increased from 1 h to 2 days under  $\text{DMF/THF}$  mixed solvents to obtain **FSG3**; 9',9''''-(sulfonylbis(4,1-phenylene))bis(3,3''',6,6''''-tetra-*tert*-butyl-6',6''''-bis(3,6-di-*tert*-butyl-carbazol-9-yl)-9,3':9,3'':6',9''':3''',9''''-quinque

carbazole) in 34% yield. The structure was confirmed clearly by  $^1\text{H-NMR}$ , IR spectroscopy as well as MALDI-TOF MS. The  $^1\text{H-NMR}$  spectrum shows similar pattern with those of **FSG1** but the number of proton between diphenyl sulfone at chemical shift 8.54 and 8.15 ppm and *tert*-buthyl part at chemical shift 1.46 ppm is to be 4:4:144 corresponding to two side of the dendron **8** substituent. The IR spectrum result was observed the vibration of 2 (S=O stretching) of diphenyl sulfone moieties at around 1262 and 1157  $\text{cm}^{-1}$ . The MALDI-TOF MS spectrum was observed to be 3427.4359 m/z, calculated for  $\text{C}_{244}\text{H}_{234}\text{N}_{14}\text{O}_2\text{S}$ : 3427.8584.



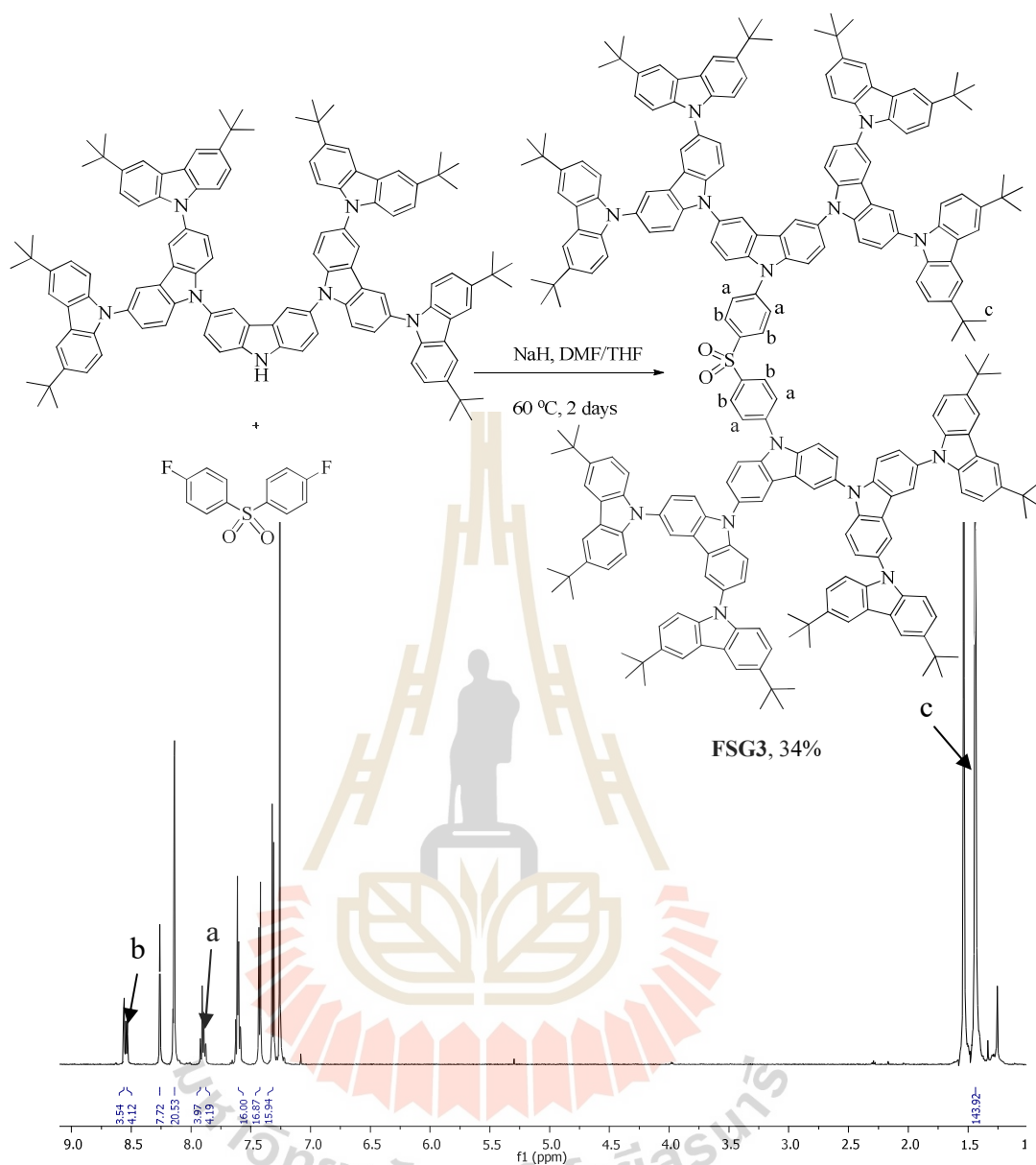


**Figure 2.14** The synthesis and <sup>1</sup>H-NMR spectrum in CDCl<sub>3</sub> of FSG3.

### 2.5.2 Optical properties

The photophysical properties of **FSG1**, **FSG2** and **FSG3** were firstly explored, and the corresponding data are summarized in Table 2.2. As depicted in Figure 2.15, all TADF emitters show similar absorbance result both thin film and under toluene solution. All molecules have intense absorption bands below  $\lambda_{\text{abs}} = 300$

nm, which are assigned to characteristic  $\pi$ - $\pi^*$  of the carbazole moiety in the dendrimers. The intensity of all TADF emitters was found to be strengthened after the introduction of increasing dendrimer size. The intramolecular charge transfer (ICT) absorption band of the molecules showed weaker intensity around 347 nm region. The ICT character remained with increasing of the dendrimer generation.

The photoluminescent (PL) spectra of **FSG1-FSG3** in toluene solution and in the solid state are shown in Figure 2.15. All molecules exhibited blue emission spectra ( $\lambda_{em} = 403$ -452 nm). The maxima PL wavelength in toluene solution showed a bathochromic shifted from **FSG1** at 403 nm to **FSG3** at 436 nm with the increase of the dendrimer generation. The PL spectra results of thin film are slightly red shifted comparing with the solution from **FSG1** at 423 nm, **FSG2** at 446 nm to **FSG3** at 452 nm, respectively. These materials show small red shifts (20 nm of **FSG1**, **FSG2** and 15 nm of **FSG3**), suggesting that the intermolecular  $\pi$ - $\pi$  interactions effect in the solid state are well prevent by the bulky molecular structure of rigid carbazole dendrons.

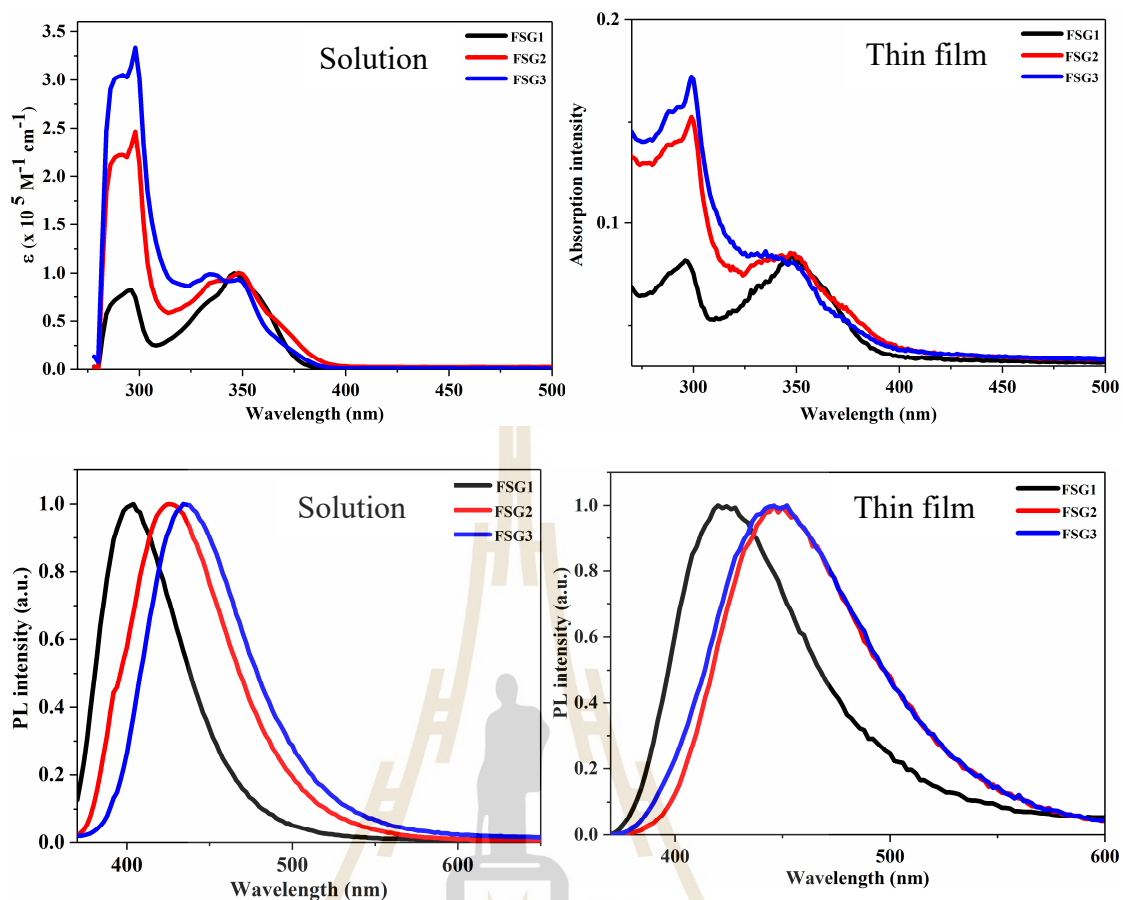


**Figure 2.15** UV-Vis absorption and PL spectra of all TADF emitters ( $\lambda_{\text{ex}} = 350 \text{ nm}$ ) in toluene solution and thin film.

Since most of the known TADF emitters are donor-acceptor molecules, the charge transfer (CT) excited state and its energy is of vital importance. The ICT characters of the dendrimers were further demonstrated by measurement of the PL and UV-Vis absorption spectroscopy in various solvents from less polar solvent toluene to more polar solvent 1,2-dichloro benzene (see Figure 2.16). The emission maxima are red-shifted from 404-436 nm, 427-510 nm and 433-510 nm for **FSG1**, **FSG2** and **FSG3**, respectively. Broad and unstructured emission band with the emission peak

shifted distinctly by changing the polarity of the solvent could be observed. This result indicated that all blue TADF molecules have the ICT behavior.

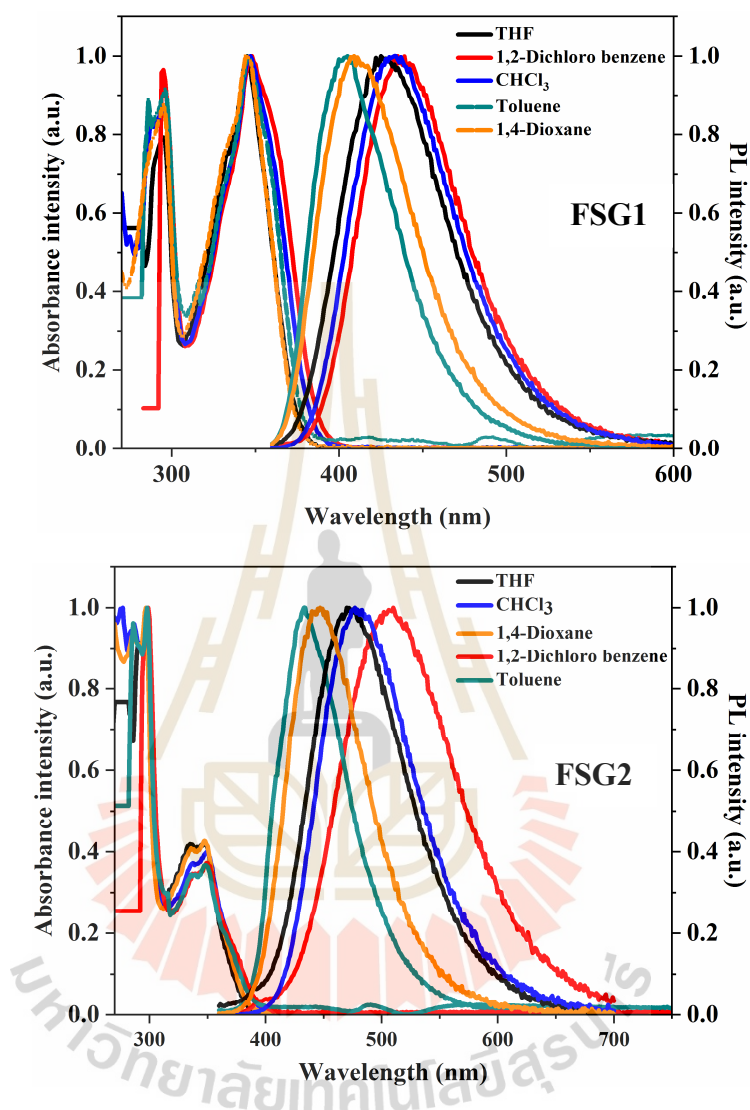


**Figure 2.16** UV-Vis absorption and PL spectra of FSG1-FSG2 in various solvents.

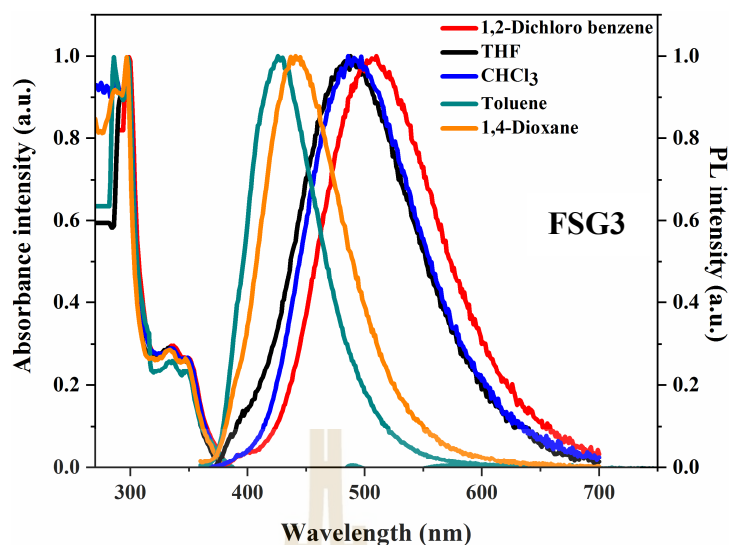


**Figure 2.16** UV-Vis absorption and PL spectra of **FSG3** in various solvents (Continued).

The  $O_2$  quenching experiments were used to study the ISC formation of all TADF molecules. The emission with this study showed that **FSG1-FSG3** have increasing phosphorescent character with decreasing  $O_2$  density in the toluene solution (see Figure 2.17). This is consistent with the efficiency ISC to the donor triplet state instead of CT formation. The  $O_2$  quenching study also concludes that all molecules have triplet characteristic under  $O_2$  and  $O_2$  free in toluene solvent study. This is the signature of TADF character.

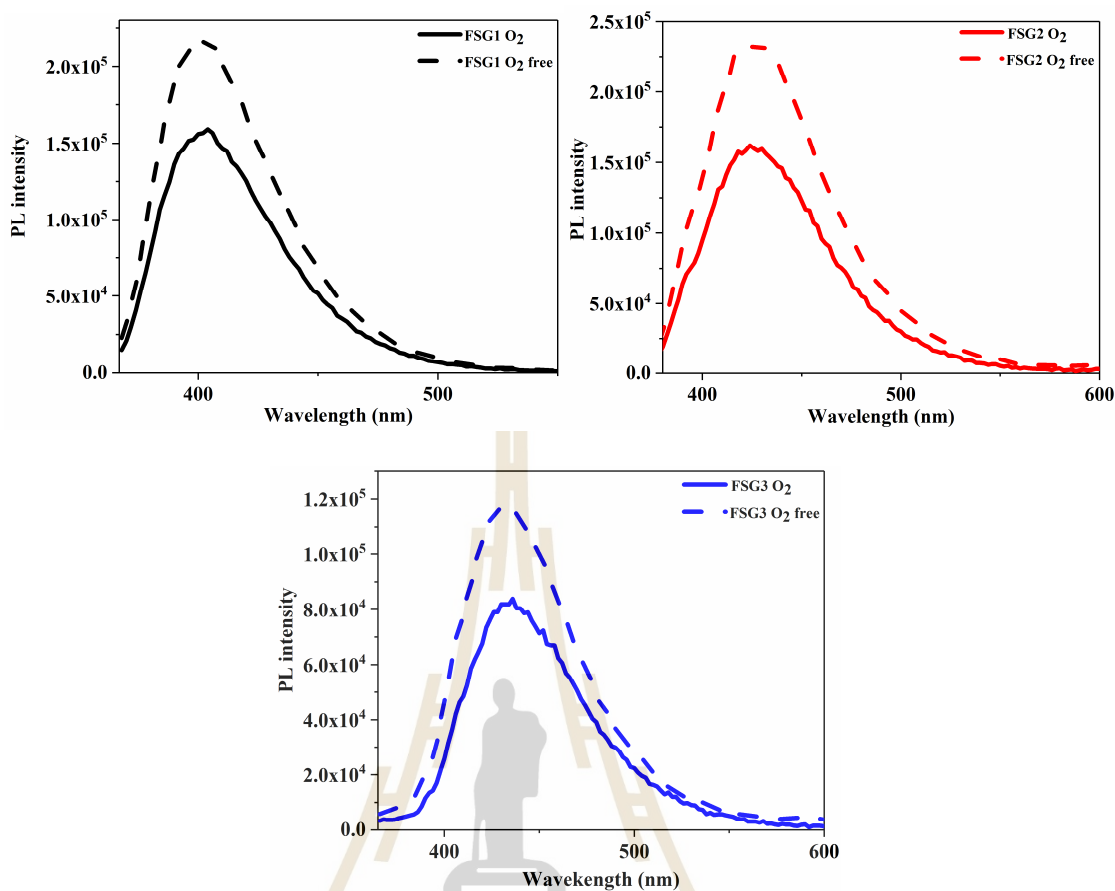


**Figure 2.17** The emission spectra of **FSG1-FSG3** in solution under  $O_2$  and  $O_2$  free.

### 2.5.3 Time-resolved fluorescence decay

The lifetimes of the slow decay in the thin film increased dramatically to 8.40, 11.35 and 13.69 ns (Figure 2.18) with increasing the number of carbazole dendrimer and also the same result under toluene solution as expected. To compare the effect of  $O_2$  quenching theory for TADF materials with this effect study, all TADF molecules were measured the emission lifetime into 2 conditions. First condition is the lifetime of **FSG1**, **FSG2** and **FSG3** in toluene solution under  $O_2$  atmosphere. They show the emission lifetime value of 5.26, 7.30, 8.98 ns, respectively. The data are summarized in Table 2.2. The second conditions, all molecules were also measured in toluene solution under argon atmosphere. The values are increased to

6.68, 9.82 and 12.68 ns for **FSG1**, **FSG2** and **FSG3**, respectively. The results concluded that all molecules have TADF characteristic causing from ISC characteristic studies

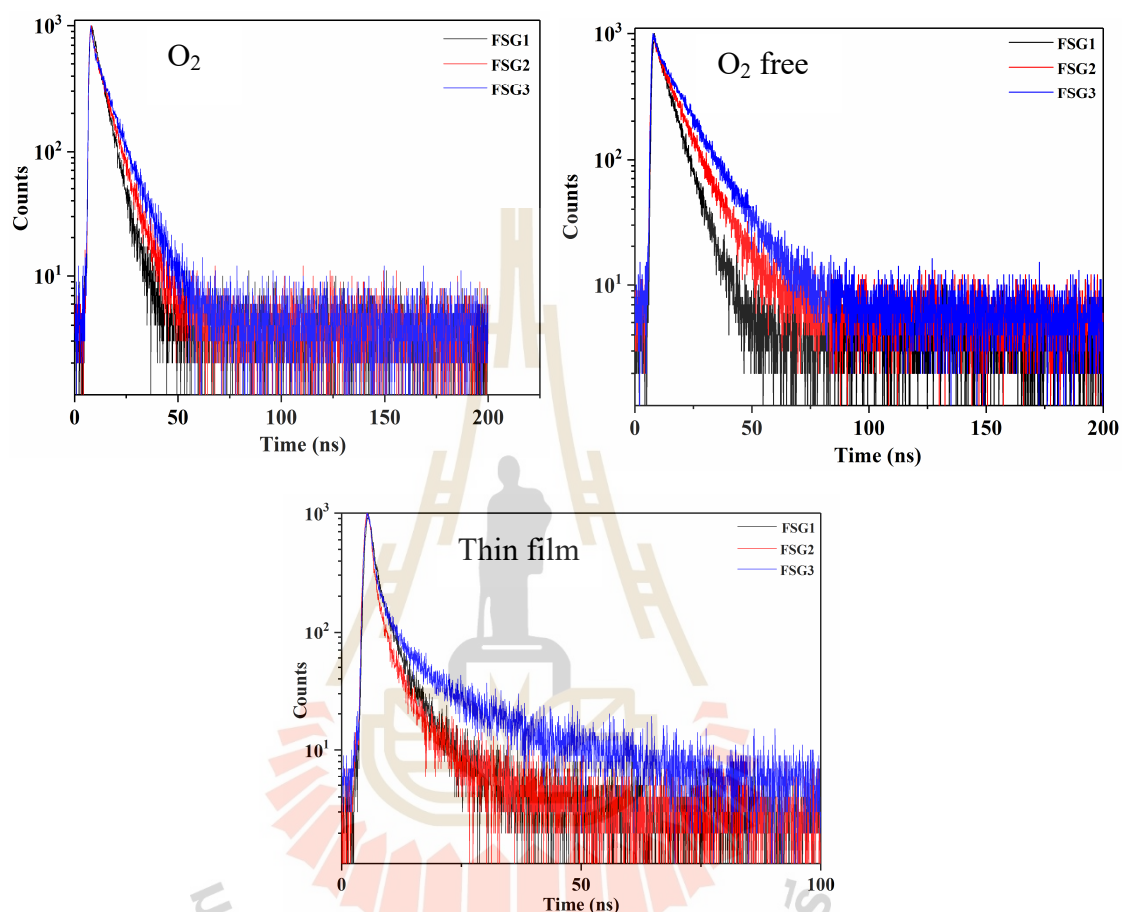


**Figure 2.18** Time-resolved fluorescence decay of all TADF emitters in toluene solution (O<sub>2</sub> and O<sub>2</sub> free) and thin film.

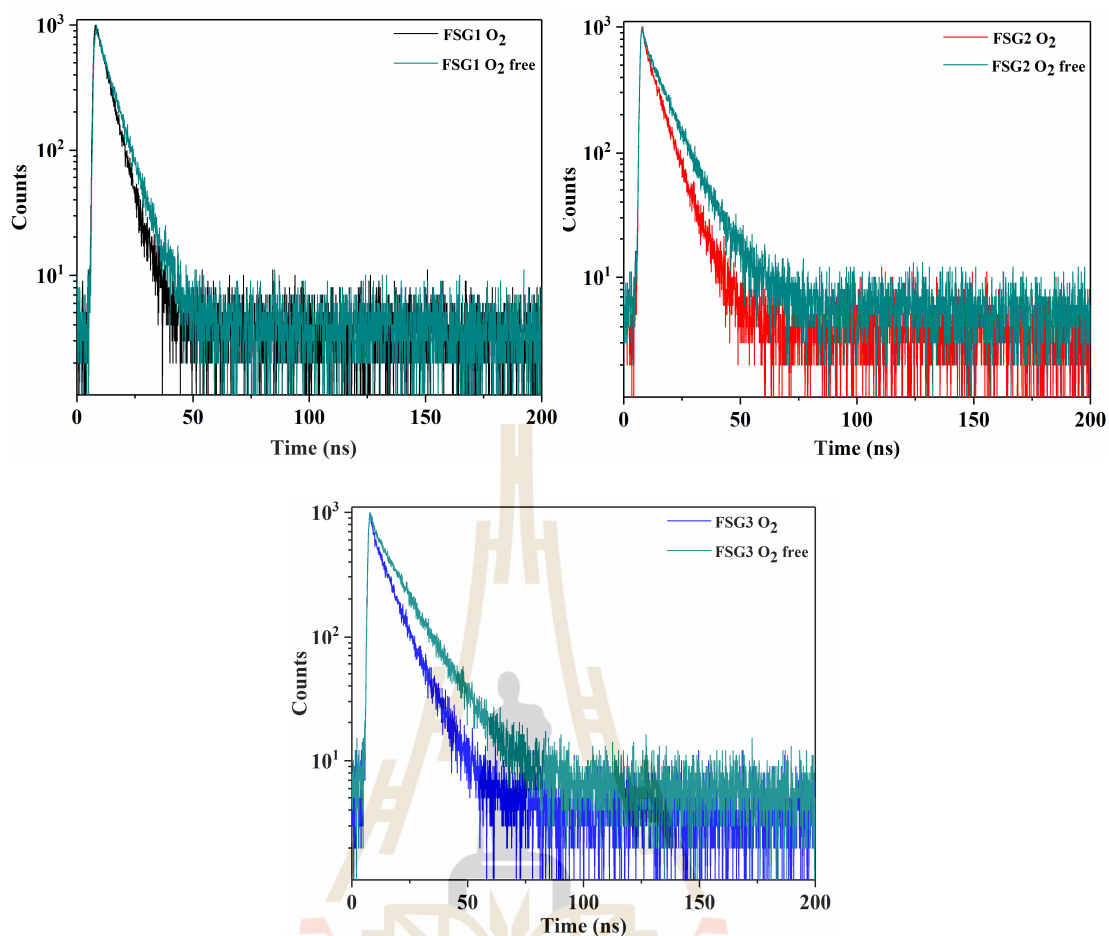


**Figure 2.19** Time-resolved fluorescence decay of all TADF emitters in toluene solution under O<sub>2</sub> and O<sub>2</sub> free.

**Table 2.2** Photophysical properties and emission lifetimes of FSG1-FSG3.

Comp.	$\lambda_{\text{abs}}^{\text{sol}} (\epsilon)$ (nm, M <sup>-1</sup> cm <sup>-1</sup> ) <sup>a</sup>	$\lambda_{\text{em}}^{\text{sol}}/\lambda_{\text{em}}^{\text{film}}$ (nm) <sup>b</sup>	$\tau_{\text{p}} (\text{ns})^{\text{c}}$		
			O <sub>2</sub>	O <sub>2</sub> free	film
<b>FSG1</b>	446 (9,798)	403/423	5.26	6.68	8.98
<b>FSG2</b>	349 (9,977)	426/446	7.30	9.82	12.68
<b>FSG3</b>	439 (9,260)	437/452	8.43	11.35	13.69

<sup>a</sup>Measured in Toluene (10<sup>-5</sup> M) at 298 K.

<sup>b</sup>Measured in Toluene (10<sup>-6</sup> M) and thin film at 298 K.

<sup>c</sup>Measured in CH<sub>2</sub>Cl<sub>2</sub> (10<sup>-6</sup> M) (O<sub>2</sub> and O<sub>2</sub> free) and thin film at 298 K

#### 2.5.4 Thermal properties

The thermal properties of all compounds were evaluated by differential scanning calorimetry (DSC) and thermogravimetric analysis (TGA) under N<sub>2</sub> atmosphere with a heating rate of 10 °C per minute. The DSC and TGA data revealed that the three thermally activated delayed molecules are thermally and morphologically stable materials as summarized in Table 2.3. From the onset of DSC curves **FSG1** has no observed with the T<sub>g</sub> value, whereas **FSG2** and **FSG3** exhibit evident glass transition temperature at 263 and 299 °C in the heating tests, respectively shown in Figure 2.20. The TADF dendrimers exhibited high thermal stability with decomposition temperatures (T<sub>d</sub>, corresponding to 5% weight loss) in the range of 285-394 °C (see Figure 2.21). Their thermal stability increased with increasing the carbazole generation, probably owing to the increased number of the thermal-stabilized carbazole groups. These suggest that all TADF molecules could form good quality thin films by vacuum deposition during device fabrication process. These result prove that the use of carbazole dendrimers as self-hosting and donor properties could increase the service time in device operation.

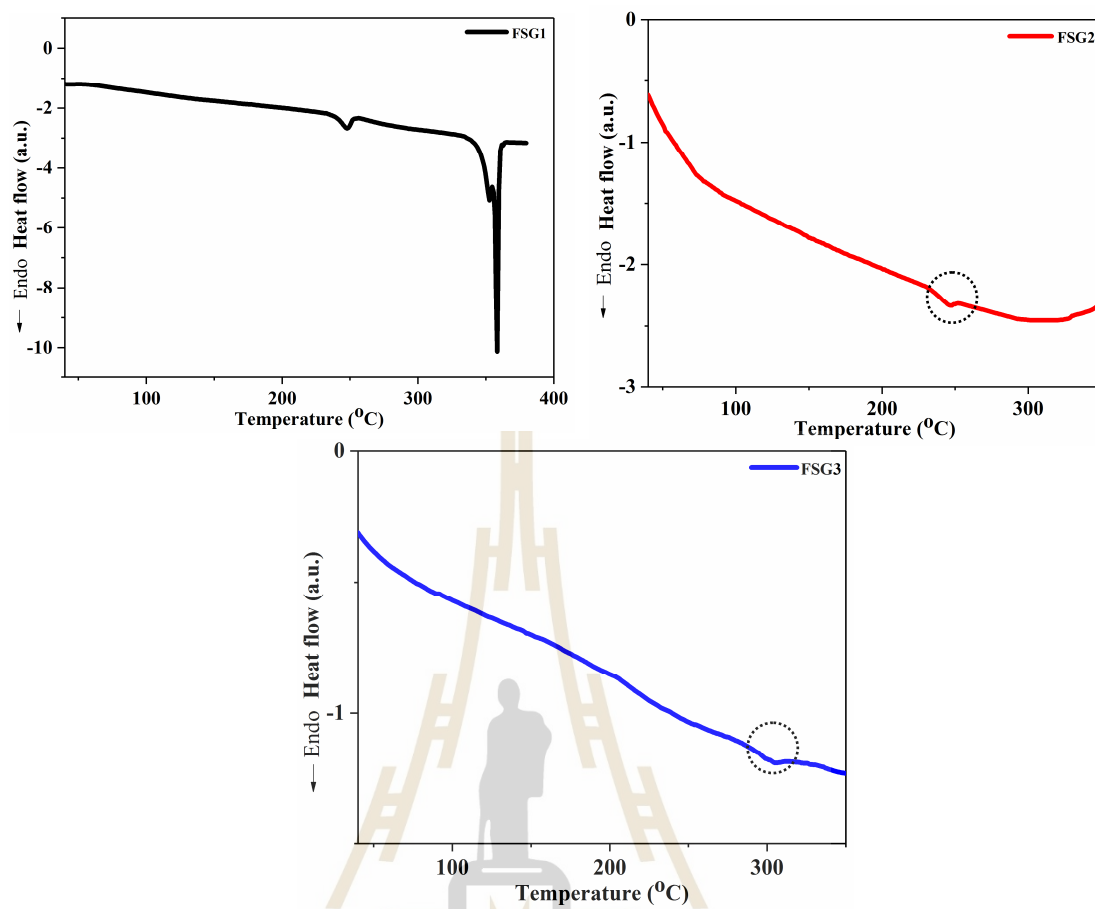


**Figure 2.20** DSC thermograms of novel blue TADF emitters measured at a heating rate of  $10\text{ }^{\circ}\text{Cmin}^{-1}$  under  $\text{N}_2$ .

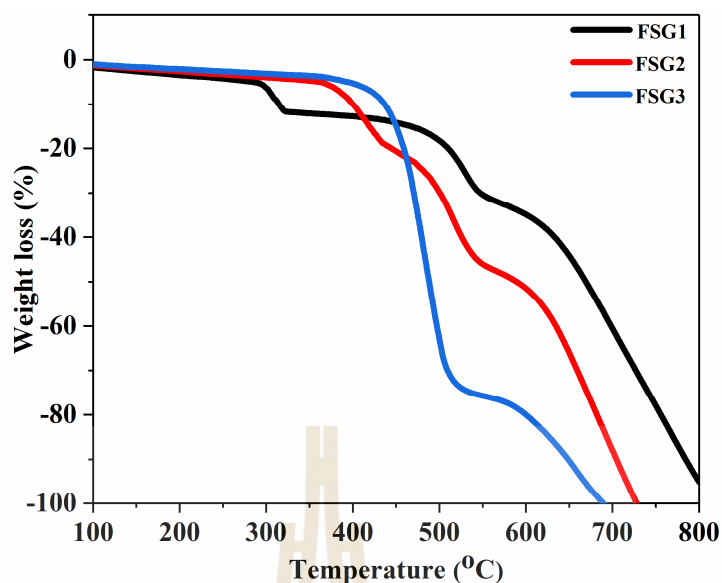


**Figure 2.21** TGA thermograms of new blue TADF emitters measured at a heating rate of  $10\text{ }^{\circ}\text{Cmin}^{-1}$  under  $\text{N}_2$ .

### 2.5.5 Electrochemical properties

We explained that the electrochemical characteristics of the dendrimers using cyclic voltammetry. Toluene solutions (0.1 M) of each compound were scanned in the potential range of  $-1.5$  to  $1.5$  V in a conventional 3-electrode voltammetry workstation. Figure 2.22 shows the cyclic voltammograms of all compounds. The cyclic voltammogram of **FSG1**, **FSG2** and **FSG3** showed the reversible oxidation peak assigned to carbazole dendrons oxidation process with the oxidation onset at  $1.25$ ,  $1.03$  and  $0.92$  V, respectively. The first oxidation wave of the dendrimers shifted to lower potentials with increasing the dendrimer generation, owing to the extended conjugation of the dendrons and the increased electron-donating ability with increasing the dendron generation. These observations were in agreement with the theoretical studies carried out on these molecules. Based on the oxidation onset the

values HOMOs of **FSG1** to **FSG3** were assessed at -5.69, -5.47 and -5.36 eV, respectively. Moreover, the reversible reduction peak was observed in the 0 to -1.5 V potential window assigned as diphenyl sulfone reduction process. The electronic band gap ( $E_g$ ) was calculated using UV-Vis absorption onset to be 3.16, 3.18 and 3.25 eV which provided LUMOs at -2.53, -2.29 and -2.11 eV for **FSG1**, **FSG2** and **FSG3**, respectively (Table 2.3).

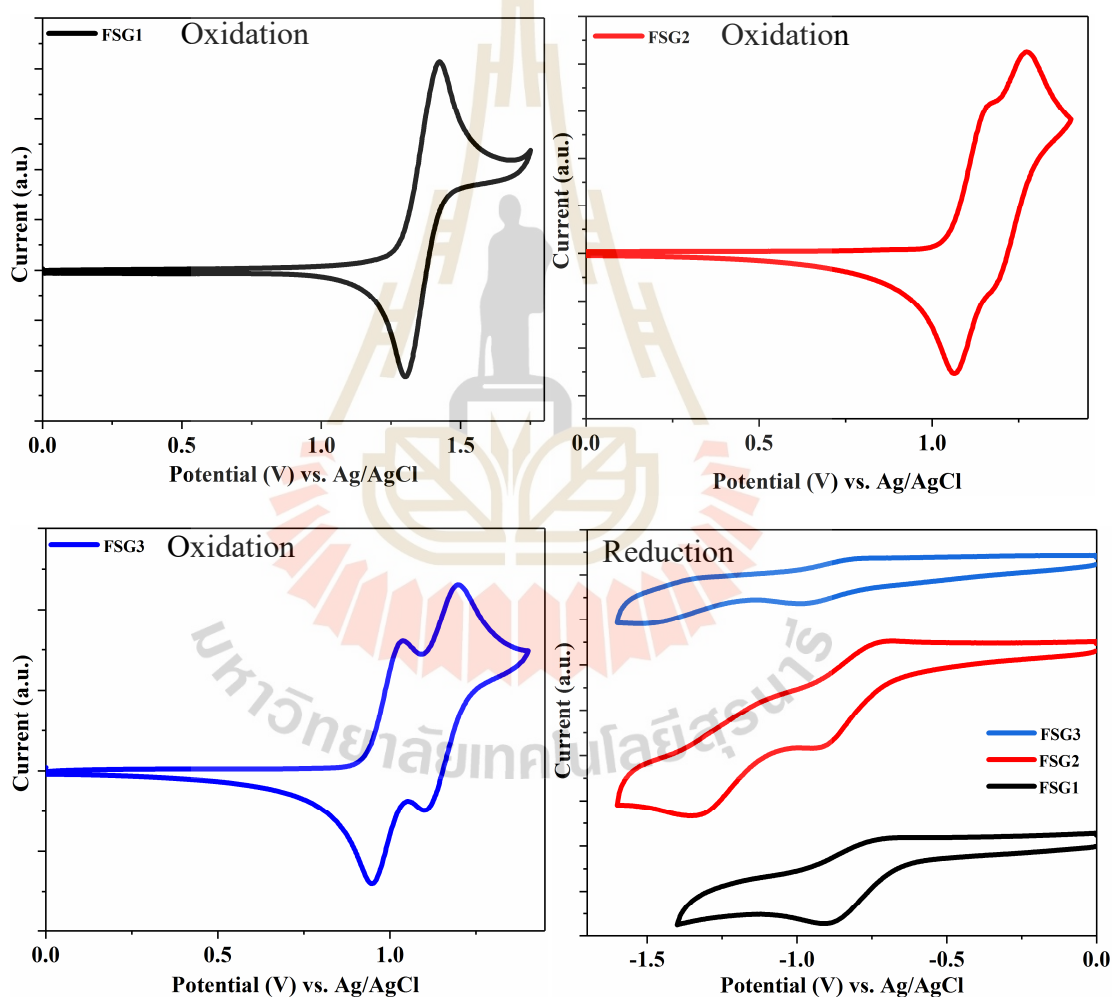


**Figure 2.22** CV curves of the dendrimers **FSG1-FSG3** in toluene solution using 0.1 M  $\text{Bu}_4\text{NPF}_6$  at a scan rate of 50 mV/s.

**Table 2.3** Thermal and electrochemical properties of **FSG1-FSG3**.

Comp.	T <sub>g</sub> /T <sub>d</sub> (°C) <sup>a</sup>	ΔE <sub>ST</sub> (eV) <sup>b</sup>	E <sup>ox</sup> <sub>onset</sub> (V) <sup>c</sup>	HOMO (eV) <sup>d</sup>	E <sub>g</sub> eV <sup>e</sup>	LUMO (eV) <sup>f</sup>
<b>FSG1</b>	-/285	0.41	1.25	-5.69	3.16	-2.53
<b>FSG2</b>	236/362	0.51	1.03	-5.47	3.18	-2.29
<b>FSG3</b>	299/394	0.61	0.92	-5.36	3.25	-2.11

<sup>a</sup> Corrected from DSC and TGA techniques at scan rate 10 °C/min.

<sup>b</sup> Calculated from TDA-M062X/6-31G(d) methods in CH<sub>2</sub>Cl<sub>2</sub> solvent.

<sup>c</sup> Measured by CV in CH<sub>2</sub>Cl<sub>2</sub> vs Ag/Ag<sup>+</sup> at a scan rate of 50 mV/s.

<sup>d</sup> Calculated from onset oxidation potential HOMO = -(E<sup>ox</sup><sub>onset</sub> + 4.44) eV

<sup>e</sup> Calculated from λ<sup>abs</sup><sub>onset</sub>; E<sub>g</sub> = 1240/λ<sup>abs</sup><sub>onset</sub>

<sup>f</sup> Calculated from LUMO = HOMO + E<sub>g</sub>

### 2.5.6 Quantum chemical calculation

The calculation results revealed that the molecules adopted nonplanar three-dimensional structures with carbazolyl dendrons arranging twisted around the diphenyl sulfone core (Figure 2.23). Their geometries and energies were optimized by density functional theory (DFT) calculations using B3LYP/6-31G(d) method. For dendrimers **FSG1-FSG3**, the HOMOs were mainly distributed over the outer carbazolyl units, whereas the LUMOs were mainly localized on the electron withdrawing diphenyl sulfone core. The twisted geometry, together with the effective spatial separation between the HOMO and LUMO, implied a small singlet-triplet splitting energy for the T<sub>1</sub>-to-S<sub>1</sub> transition of the molecules, which was considered to be beneficial for efficient reverse intersystem crossing (RISC). This is the designed property of the TADF emitters.

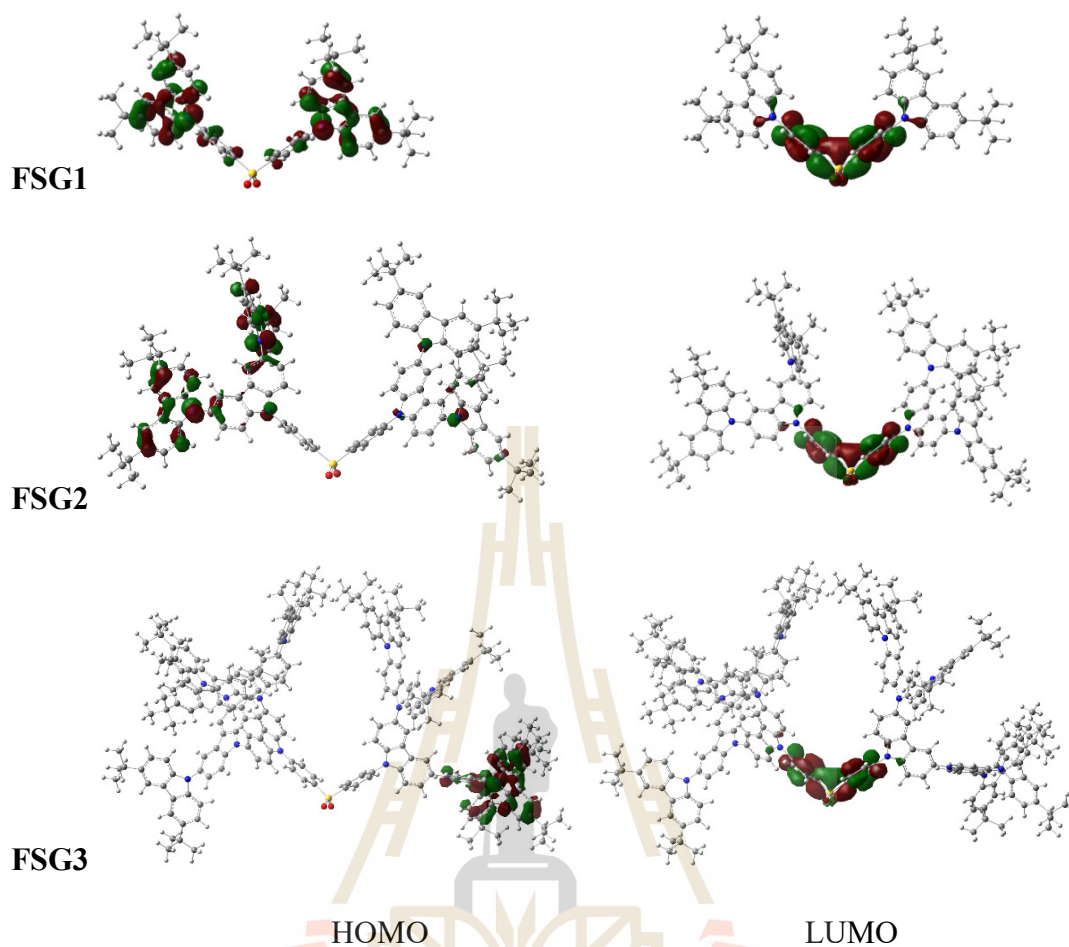


**Figure 2.23** the spatial distribution of HOMO (left) and LUMO (right) energy densities of FSG1-FSG3 by DFT B3LYP/6-31G(d) calculation.

## 2.6 Conclusions

To summarize, the three novel self-hosting blue TADF materials based on carbazole dendrimers up to the third generations, **FSG1**, **FSG2** and **FSG3**, were designed and synthesized for using as emitters in OLED devices. All blue TADF emitters were characterized using NMR, IR, MALDI-TOF MS, UV-Vis, DSC, TGA and photoluminescence techniques. They display red shifted photoluminescence emission spectra and negatively shifted oxidation potentials when the size or generation of the carbazole dendrimers are increased as expected. All molecules

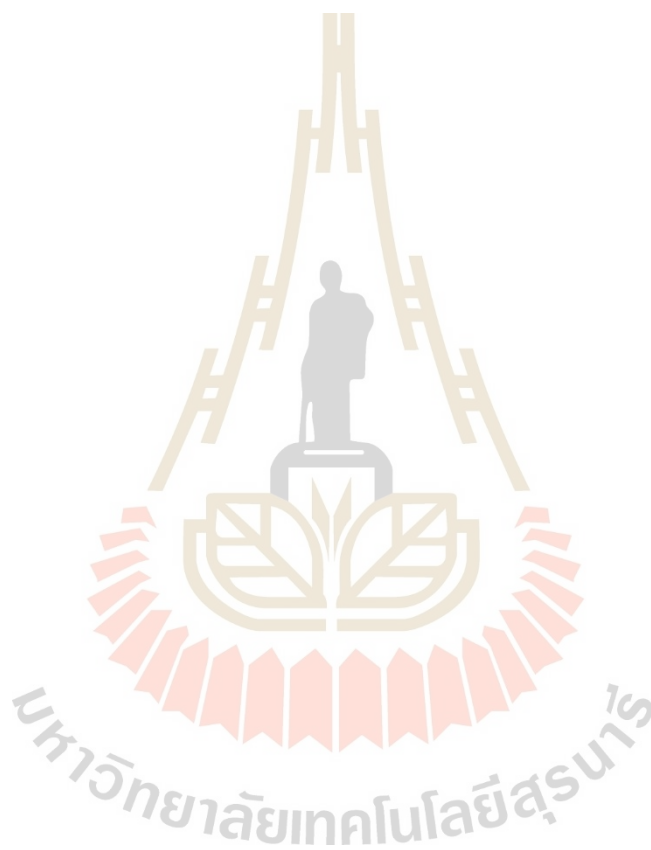
showed the TADF characteristics; red shifted emission spectra with various polarity solvents due to the ICT character, O<sub>2</sub> quenching effect with photoluminescence intensity and time-resolved fluorescence decay due to ISC formation and twisted donor-acceptor structure corresponding to obtain the separation HOMO-LUMO energy level as well as low  $\Delta E_{ST}$  less than 1 eV of all designed novel blue TADF molecules. Furthermore, all molecules show high thermal stability and could be formed morphologically stable amorphous thin film with T<sub>g</sub> value over 236 °C.

## 2.7 References

- Li, J., Liao, X., Xu, H., Li, L., Zhang, J., Wang, H. and Xu, B. (2017). Deep-blue thermally activated delayed fluorescence dendrimer with reduced singlet-triplet energy gap for low roll-off non-doped solution-processed organic light-emitting diodes. **Dyes and Pigments**. 140: 79-86.
- Moonsin, P., Prachumrak, N., Namuangruk, S., Jungstittiwong, S., Keawin, T., Sudyoadsuk, T. and Promarak, V. (2014). Bifunctional oligofluorene-cored carbazole dendrimers as solution-processed blue emitters and hole transporters for electroluminescent devices. **Journal of Materials Chemistry C**. 2: 5540-5552.
- Prachumrak, N., Pojanasopa, S., Namuangruk, S., Keawin, T., Jungstittiwong, S., Sudyoadsuk, T. and Promarak, V. (2013). Novel bis[5-(fluorene-2-yl)thiophen-2-yl]benzothiadiazole end-capped with carbazole dendrons as highly efficient solution-processed nondoped red emitters for organic light-emitting diodes. **ACS Applied Materials & Interfaces**. 5: 8694-8703.

- Uoyama, H., Goushi, K., Shizu, K., Nomura, H. and Adachi, C. (2012). Highly efficient organic light-emitting diodes from delayed fluorescence. **Nature**. 492: 234-240.
- Wang, C., Li, X., Pan, Y., Zhang, S., Yao, L., Bai, Q., Li, W. Lu, P., Yang, B. Su, S. and Ma, Y. (2016). Highly efficient nondoped green organic light-emitting diodes with combination of high photoluminescence and high exciton utilization. **Applied Materials & Interfaces**. 8: 3041-3049.
- Wu, T.-L., Chou, H.-H., Huang, P.-Y., Cheng, C.-H. and Liu, R.-S. (2014). 6,9,12-Tetrasubstituted chrysenes: synthesis, photophysical properties, and application as blue fluorescent OLED. **Journal of Organic Chemistry**. 79: 267-274.
- Wu, S., Aonuma, M., Zhang, Q., Huang, S., Nakagawa, T., Kuwabara, K. and Adachi, C. (2014). High-efficiency deep-blue organic light-emitting diodes based on a thermally activated delayed fluorescence emitter, **Journal of Materials Chemistry C**. 2: 421-424.
- Yun, J.H. and Lee, J.Y. (2017). Benzoisoquinoline-1,3-dione acceptor based red thermally activated delayed fluorescent emitters. **Dyes and Pigments**. 144: 212-217.
- Zhang, Q., Li, J., Shizu, K., Huang, S., Hirata, S., Miyazaki, H. and Adachi, C. (2012). Design of efficient thermally activated delayed fluorescence materials for pure blue organic light emitting diodes. **Journal of the American Chemical Society**. 134: 14706-14709.

Zhang, Q., Li, B., Huang, S., Nomura, H., Tanaka, H. and Adachi, C. (2014).  
Efficient blue organic light-emitting diodes employing thermally activated  
delayed fluorescence. **Nature Photonics**. 8: 326-332.



# **CHAPTER III**

## **SYNTHESIS AND CHARACTERIZATION OF A NEW CLASS OF ORGANIC SPIN FILTER FOR MAGNETORESISTANCE DEVICES**

### **3.1 Introduction**

Magnetoresistance (MR) is a phenomenon that reflects the resistance change of a material when an external magnetic field is applied to it. The interest in the MR effect is growing due to its applications in the magnetic recording system over the last few decades. Especially, the MR effect has made a great impact on the computer memory and storage technology. Generally, the MR effect can be classified into six distinct types including ordinary magnetoresistance (OMR), anisotropic magnetoresistance (AMR), giant magnetoresistance (GMR), tunneling magnetoresistance (TMR), colossal magnetoresistance (CMR) and organic magnetoresistance (OMAR). All of these types will be described below;

1. Ordinary magnetoresistance (OMR) is often observed in the non-magnetic metals. OMR is due to the electrons deviating from the electric field direction by the Lorentz force, which increases the resistivity with increasing magnetic field. Generally, the OMR is strongly dependent on the measured temperatures and becomes larger at lower temperature due to the decreased thermal phonon scattering.

2. Anisotropic magnetoresistance (AMR) is the effect defined as the difference

between  $\rho_{\parallel}$  (the resistivity when the magnetic moment  $M$  is parallel to the electrical current  $i$ ) and  $\rho_{\perp}$  (the resistivity when  $M$  is transverse to  $i$ ) shown in Figure 3.1. The AMR effect is often found in a number of thin films of FM metals and alloys of Fe, Co and Ni. At room temperature, the anisotropic resistance in alloys of Ni-Co and Ni-Fe can be better than 5% based on the orientation of magnetic moments with respect to the direction of electric current. It arises from the spin-orbit coupling and d band splitting.

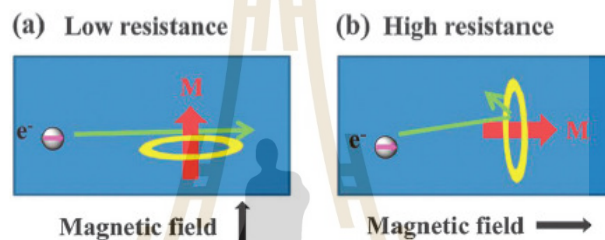


**Figure 3.1** Schematic of the AMR effect: (a)  $M$  is transverse to  $i$  and (b)  $M$  is parallel to  $i$ .

3. Giant magnetoresistance (GMR) is a quantum mechanical effect, which was first observed in a multilayered thin-film structural material composed of a couple of FM Fe layer separated by a non-magnetic Cr layer in 1988. GMR was defined as the ratio of  $(R_{AP}-R_P)/R_P$ , where  $R_P$  and  $R_{AP}$  are the resistance of the materials for parallel and antiparallel alignments of two magnetic electrodes, based on the magnetization state of the materials under an applied magnetic field.

4. Tunneling magnetoresistance (TMR) normally takes place in a magnetic tunnel junction. It is composed of two ferromagnets (electrodes) separated by a thin insulating layer (a tunnel barrier) and the resistance is different for the parallel and

antiparallel magnetic configurations of these two electrodes. The electrons travel from one FM layer to another FM layer by the tunnel effect.

5. Colossal magnetoresistance (CMR) is an extremely large resistivity change by orders of magnitude in the manganite perovskites  $T_{1-x}D_xMnO_3$  (where T is a trivalent lanthanide (La) cation, D is a divalent cation like Ca, Sr or Ba) by applying an external magnetic field. The mechanism of CMR is still not well understood. However, some researchers believed that the observed CMR is associated with the interplay between electron-phonon coupling and FM-to-paramagnetic phase transition.

6. Organic magnetoresistance (OMAR) effect was first observed in the metallic multi layers, achieving coherent spin transport over distance at the nanometer scale has proved to be difficult in the normal metals or semiconductors. This challenge work was the development of new materials, in which both efficient spin injection and transport. Recently, they have also been considered by physical and chemical scientists as new spin transport materials which have weak spin-orbit coupling and hyperfine interaction.

The GMR effect is considered as the birth of spintronics. It is an emerging technology, where it is not the electron charge but the electron spin that carries information. Spintronics is associated with both intrinsic spin of electrons and their magnetic moment in a solid state system. Organic molecules were proposed for “molecular spintronics” in which they typically serve as a passive material, namely material through which the spin can be transported intact. In this regard, molecules have important advantages such as weak spin-orbit coupling and weak hyperfine interactions that allow relatively longer coherent spin lifetimes and spin transport

distances. Recently report, the chirality-induced spin selectivity (CISS) effect has been discovered in organic chiral molecules. CISS is the phenomenon of the electron transmission yield through chiral molecules depends on the electron spin orientation. Electron in the spin-up state preferentially traverses a chiral molecule in one direction, while electron in the spin-down state traverses the same chiral molecule easily in the reverse direction, shown in Figure 3.2.

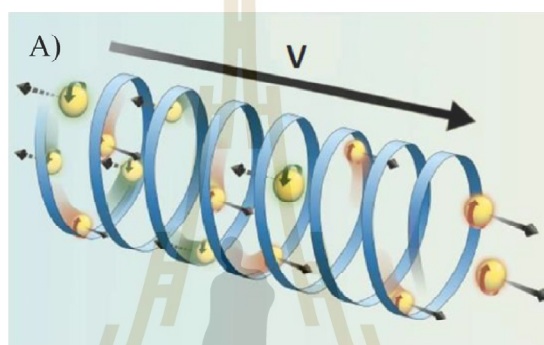


**Figure 3.2** Schematic illustration of the CISS effect (Waldeck and Naaman, 2012).

Chiral molecule is the definition of two different mirror-image (chiral) shapes, namely two enantiomers. The enantiomer are recognized by their ability to rotate the polarization of linear polarized light either to the left (L) or to the right (D). Determining the axial stereochemistry of biaryl atropisomers can be accomplished through the use of Newman projection along the axis of hindered rotation. Starting with the substituent of highest priority in the closest ring and moving along the shortest path to the substituent of highest priority in the other ring. The absolute configuration is assigned *P* for the clockwise and *M* for counterclockwise, presented in Figure 3.3.

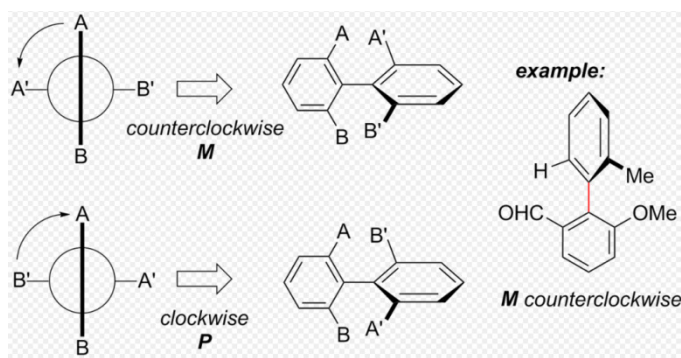


**Figure 3.3** The determining stereochemistry in atropisomers (<https://en.wikipedia.org/wiki/Atropisomer>).

Chemists now know that chiral molecules can act as electron spin filter in organic magnetoresistance devices, because of its chiral induced spin selectivity effect (CISS). In this new approach, the permanent magnetic layer is replaced by an organic chiral material that is nonmagnetic and acts as a spin filter to provide a spin-polarized electron tunneling current.

The common organic magnetoresistance device consists of Au act as bottom electrode/ chiral molecule acted as organic spin filter was coated on top of Au/  $\text{Al}_2\text{O}_3$  layer is deposited followed by a layer of Ni as top electrode, shown in Figure 3.4.

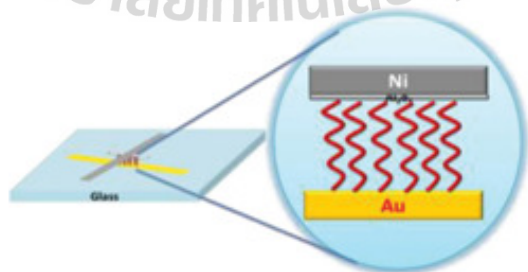


**Figure 3.4** Schematic diagram of the organic magnetoresistance device.

### 3.2 Literature reviews of organic spin filter materials

Organic chiral molecules can serve as non-magnetic spin filters in the organic magnetoresistance devices because the electron transmission probability through them strongly depends on the electron's helicity. Electrons of a certain spin can traverse the molecule more easily in one direction than in the other (depending on the handedness of the molecule). Several excellent reviews on the synthesis of organic spin filter molecules have appeared during the past few decades. Herein, we highlight recent advances in the development of molecular designed synthesis to obtain novel organic spin filter compounds.

Jaker and co-workers (1995) reported the synthesis method of a highly stereoselective optical switching process (**P3** and **M4**) based on donor-acceptor substituted dissymmetric alkenes. These chiral compounds will be suited as optical write-read-erase information storage systems. The results demonstrate that the photochemical isomerization of both **P3** and **M4** is stereospecific and also shows high wavelength-dependent diastereoselectivity.

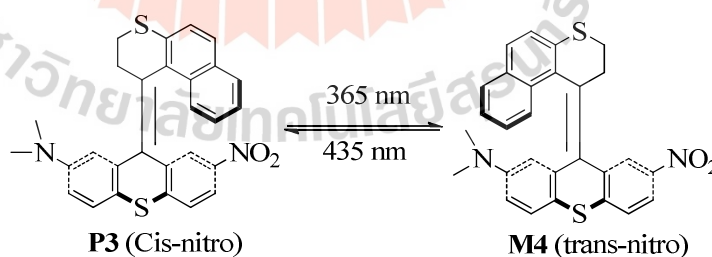


**Figure 3.5** Chiroptical molecular switch based on the photoisomerization (**P3**, **M4**).

Delden and Andreas (2002) improved the solubility of compound M (**cis-2.4**) and P (**Trans-2.4**) with *N*-hexyl group as donor moiety in organic solvents and compatibility in liquid crystalline matrices. The *n*-hexyl donor substituent also proved

to have an effect on the switching efficiency. The racemization barrier ( $\Delta G$ ) was determined for M-cis 2.4 of 124.6 kJ/mol and P-trans of 118.4 kJ/mol.

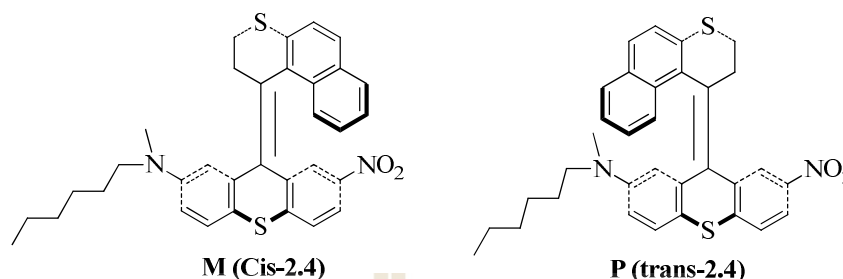


**Figure 3.6** *N*-Hexyl functionalized donor-acceptor target molecule 2.4.

Delden van and co-workers (2003) synthesized a new type of chiroptical molecular switch spin filter where irradiation with different wavelengths of light induces a reversible helix inversion. The additional stereogenic center in the chiral auxiliary group has a distinct influence on the switching selectivity of this system and greatly facilitates the resolution of the different diastereoisomers. In addition, they reported the possibility of synthesizing a variety of donor-acceptor systems in one step starting from a mutual bromo-substituted synthon.

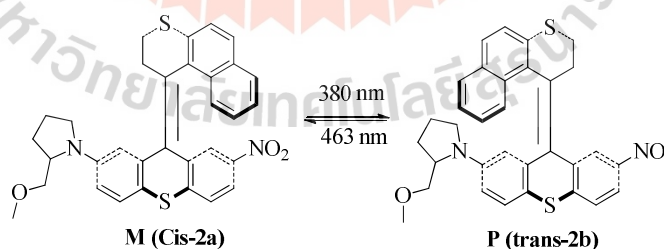


**Figure 3.7** Molecular structure of selective switching between two atropisomers.

Kiran and co-worker (2016) synthesized a new class of organic spin filter, called Helicenes. These molecules demonstrate high spin selectivity and have high configurationally stable helicenes due to the steric repulsion between the terminal

methoxy groups. They present a very high barrier of racemization ( $\Delta G \approx 172 \text{ KJ mol}^{-1}$  at  $200 \text{ }^\circ\text{C}$ ).

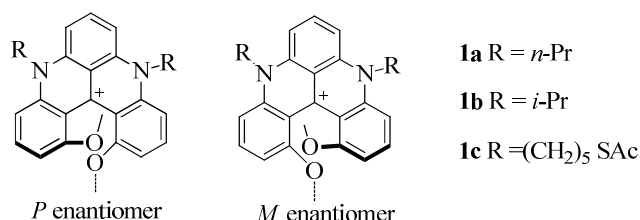


**Figure 3.8** Molecular structure of *P*- and *M*-helicenes.

Our study concentrated on the synthesis of novel chiral molecules acted as organic spin filters which have chiral induced spin selectivity (CISS) effect (Figure 3.9). It is the new technology for the injection of spin polarized current without the need for a permanent magnetic layer. Molecules that are chiral have two types of enantiomers that can be described as left-handed and right-handed species. It is one of the few types of chiral switches where the chirality itself is switched upon photoexcitation. Here, switching itself does not influence the chirality of the system but merely results in a geometrical change leading to a change in chiral properties, i.e. optical rotation, circular dichroism, or chiral perturbation by a given compound on its surroundings. When light is used as a stimulus for both to the forward and the reverse process, the totally different absorption spectra of the two isomers ensures high selectivity.

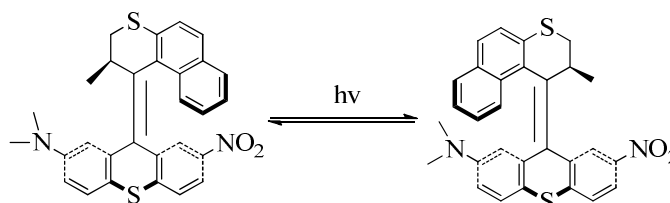


**Figure 3.9** Donor-acceptor substituted molecular organic spin filter **21**.

### 3.3 Aims of the study

Because a chiral molecule has a helical electrostatic potential, from a symmetry perspective, their electronic properties may be understood by studying an organic spin filter. This chapter deals with the designed and synthesis the chiroptical molecular switches based on donor-acceptor substitution resulted in improved switching efficiency and also showed in a red shift in UV-Vis absorption. Therefore, the objectives of this chapter are following:

1. To synthesize the novel organic spin filters composed of the dimethylamine as donor and nitro group as acceptor part based on over crowned alkenes.
2. To characterize the synthesized target organic spin filter materials by NMR and LCMS techniques.
3. To study the helix property of the synthesized target compound by circular dichroism (CD) technique.

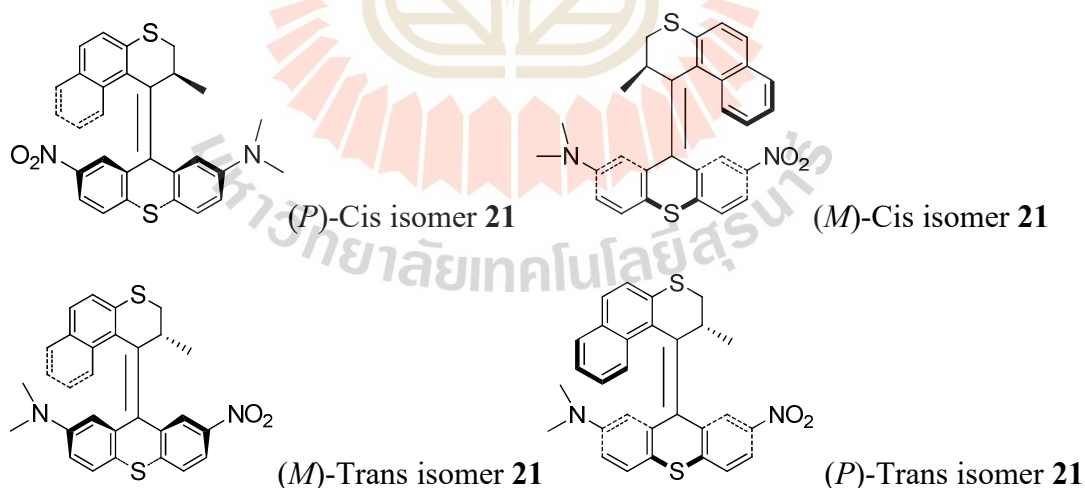


**Figure 3.10** The molecular designed structure of donor-acceptor motor **21**.

### 3.4 Materials and methods

All reactions were performed under a nitrogen atmosphere and no special precautions were required during workup. Commercially available reagents were used without further purification unless otherwise stated. All reactions were monitored by thin-layer chromatography (TLC) with Silicycle pre-coated aluminum plates. Flash column chromatography of all compounds was carried out using silica gel (230-400 mesh) as stationary phase and using commercial organic solvents as eluents.

#### 3.4.1 Materials

All the chemicals used in this thesis were analytical grade as shown in Table 3.1

**Table 3.1** Chemicals of Chapter III.

Chemicals	Formula	Grade	Manufacturer
Ammonium chloride	$\text{NH}_4\text{Cl}$	99.5%	CARLO ERBA
2-Chloro-5-nitro benzoic acid	$\text{ClC}_7\text{H}_4\text{NO}_4$	97%	Aldrich
Copper powder	Cu	99.5%	Aldrich
Dichloromethane	$\text{CH}_2\text{Cl}_2$	99.9%	CARLO ERBA
4-(Dimethylamine)-benzenethiol	$\text{C}_8\text{H}_{11}\text{NS}$	98%	TCI
Hexane	$\text{C}_6\text{H}_{14}$	96%	TCI
Hydrazine monohydrate	$\text{NH}_2\text{NH}_2 \cdot \text{H}_2\text{O}$	98%	Aldrich

**Table 3.1** Chemicals of Chapter III (Continued).

Chemicals	Formula	Grade	Manufacturer
Hydrochloric acid	HCl	37%, for analysis	CARLO ERBA
Magnesium sulfate	MgSO <sub>4</sub>	99%	Fluka
Methacrylonitrile	C <sub>4</sub> H <sub>5</sub> N	99%	Aldrich
Methyl alcohol	CH <sub>4</sub> O	99.9%	CARLO ERBA
Naphthalenethiol	C <sub>10</sub> H <sub>7</sub> HS	99%	Aldrich
Polyphosphoric acid	H <sub>n+2</sub> P <sub>n</sub> O <sub>3n+1</sub>	115% H <sub>3</sub> PO <sub>4</sub> basis	Aldrich
Potassium hydroxide	KOH	99.99%	Aldrich
Rawesson's reagent	C <sub>14</sub> H <sub>14</sub> O <sub>2</sub> P <sub>2</sub> S <sub>4</sub>	97%	Aldrich
Silver oxide	Ag <sub>2</sub> O	99.99%	TCI
Sodiumhydrogen carbonate	NaHCO <sub>3</sub>	99.7%	CARLO ERBA
Sodium carbonate	Na <sub>2</sub> CO <sub>3</sub>	99.5%	CARLO ERBA
Sodium sulfate	Na <sub>2</sub> SO <sub>4</sub>	99%	CARLO ERBA
<i>p</i> -Xylene	C <sub>8</sub> H <sub>10</sub>	98.5%	Aldrich
Tetrahydrofuran	C <sub>4</sub> H <sub>8</sub> O	99.5%	CARLO ERBA

**Table 3.1** Chemicals of Chapter III (Continued).

Chemicals	Formula	Grade	Manufacturer
<i>Tert</i> -butyl ethyl ether	C <sub>2</sub> H <sub>5</sub> OC(CH <sub>3</sub> ) <sub>3</sub>	97%	Aldrich
Triton B	C <sub>10</sub> H <sub>17</sub> NO	40 wt.% in MeOH	Aldrich
Triphenyl phosphine	C <sub>18</sub> H <sub>15</sub> P	99%	Aldrich
Toluene	C <sub>7</sub> H <sub>8</sub>	ISO for analysis	CARLO ERBA

### 3.4.2 Characterization techniques

The structure of intermediate and the target organic spin filter molecules were characterized by <sup>1</sup>H-NMR, <sup>13</sup>C-NMR and LCMS techniques. The optical properties of compound were characterized by Circular Dichroism (CD). The details of the methods are following.

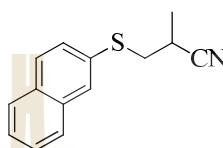
1. Nuclear magnetic resonance (NMR); <sup>1</sup>H-NMR and <sup>13</sup>C-NMR spectra were performed in CDCl<sub>3</sub> and recorded on JEOL JNM-ECS 400 MHz using TMS (0.00 ppm) as the internal reference. Data for NMR spectra are reported in the order of chemical shift ( $\delta$  ppm), multiplicity, coupling constant (*J*) and integration (Hz).

2. Mass spectroscopy; LCMS mass spectra were collected on mass spectrometry LC 908 using dried organic solvents. The data are reported as molecular weight (m/z).

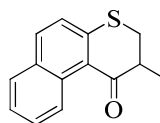
3. Circular Dichroism (CD); the optical property of chiral molecules were recorded on a JASCO J-720 WI spectropolarimeter in a 1.0 cm quartz cell,  $\lambda$  is given in nm and ellipticity (mdeg).

### 3.4.3 Synthesis methods

#### 2-Methyl-3-(naphthalen-2-ylthio) propanenitrile (14)

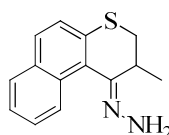


To methacrylonitrile (10 ml) cooled to  $-40\text{ }^{\circ}\text{C}$  was added dropwise of Triton B (0.02 ml). The mixture was stirred for an additional naphthalenethiol (0.5 g, 3.12 mmol) was added. The reaction mixture was allowed to reach gradually room temperature and was then heated at  $80\text{ }^{\circ}\text{C}$  overnight. After cooling at room temperature, the aq. sol. of  $\text{NH}_4\text{Cl}$  (20 ml) was then poured into the reaction and extracted with  $\text{CH}_2\text{Cl}_2$  (3 x 15 ml). The combined organic layers were washed with by brine (3 x 10 ml), dried with anhydrous  $\text{Na}_2\text{SO}_4$  and all volatiles were removed under reduced pressure giving yellow oil. The crude was purified by column chromatography using dichloromethane-hexane as eluent to yield the desired product (0.49 g, 71%);  $^1\text{H-NMR}$  (400 MHz,  $\text{CDCl}_3$ )  $\delta$  7.88 (s, 1H), 7.82-7.76 (m, 3H), 7.54-7.42 (m, 3H), 3.26 (dd,  $J = 13.8, 7.3$  Hz, 1H), 3.07 (dd,  $J = 13.8, 7.3$  Hz, 1H), 2.82-2.72 (m, 1H), 1.42 (d,  $J = 7.1$  Hz, 3H);  $^{13}\text{C-NMR}$  (101 MHz,  $\text{CDCl}_3$ )  $\delta$  133.74, 132.48, 131.21, 130.03, 129.18, 128.44, 127.86, 127.43, 126.96, 126.56, 121.64, 38.23, 26.21, 17.38; LCMS:  $m/z = 228$  ( $\text{M}^+$ ).

2-Methyl-2,3-dihydro-1H-benzo[f]thiochromen-1-one (**15**)

The nitrile **14** (0.20 g, 0.88 mmol) was added to PPA (5 ml) stirred at 70 °C. The temperature was then raised to 110 °C and stirring was continued for 3 h. The mixture was poured into ice (10 g) and allowed to hydrolyze overnight. The aqueous layer was extracted with CH<sub>2</sub>Cl<sub>2</sub> (3x15 ml), dried over anhydrous Na<sub>2</sub>SO<sub>4</sub>. After evaporation of the organic volatiles, the crude product was purified by column chromatography using dichloromethane-hexane as eluent to obtain the desired ketone (0.19 g, 95%); <sup>1</sup>H-NMR (400 MHz, CDCl<sub>3</sub>) δ 9.06 (d, *J* = 8.8 Hz, 1H), 7.76 (d, *J* = 8.5 Hz, 1H), 7.73 (dd, *J* = 8.1, 1.3 Hz, 1H), 7.57 (ddd, *J* = 8.7, 6.9, 1.5 Hz, 1H), 7.43 (ddd, *J* = 8.0, 6.9, 1.1 Hz, 1H), 7.23 (d, *J* = 8.7 Hz, 1H), 3.30-3.14 (m, 2H), 3.11 (dd, *J* = 6.3, 4.1 Hz, 1H), 1.39 (d, *J* = 6.6 Hz, 3H); <sup>13</sup>C-NMR (101 MHz, CDCl<sub>3</sub>) δ 199.34, 144.10, 133.39, 132.55, 131.77, 129.07, 128.53, 125.79, 125.64, 125.17, 42.96, 32.92, 15.44; LCMS: *m/z* = 229 (M<sup>+</sup>).

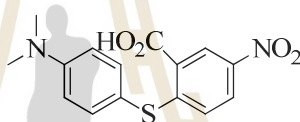
(*E*)-(2-Methyl-2,3-dihydro-1H-benzo[f]thiochromen-1-ylidene)hydrazine(**16**)



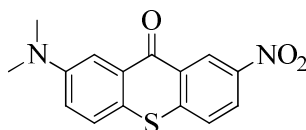
A mixture of ketone **15** (0.50 g, 2.19 mmol), hydrazine monohydrate (5 ml) and ethanol (5 ml) was heated at reflux overnight. After cooling at room temperature, water (10 ml) was then added into the reaction and the mixture was extracted with CH<sub>2</sub>Cl<sub>2</sub> (3 x 15 ml). The combined organic layer was washed with brine (3 x 15 ml),

dried over anhydrous  $\text{Na}_2\text{SO}_4$  and then all volatiles were removed to give a yellow solid. This solid was recrystallized from ether-ethyl acetate to give the hydrazone as yellow solid (0.16 g, 31%);  $^1\text{H-NMR}$  (400 MHz,  $\text{CDCl}_3$ )  $\delta$  8.41 (dd,  $J = 8.6, 1.0$  Hz, 1H), 7.75 (dd,  $J = 8.6, 1.0$  Hz, 1H), 7.63 (d,  $J = 8.5$  Hz, 1H), 7.47 (ddd,  $J = 8.5, 6.8, 1.4$  Hz, 1H), 7.39 (ddd,  $J = 8.0, 6.8, 1.4$  Hz, 1H), 7.33 (d,  $J = 8.5$  Hz, 1H), 3.60-3.46 (m, 1H), 3.19 (dd,  $J = 12.8, 6.0$  Hz, 1H), 2.70 (dd,  $J = 12.8, 9.8$  Hz, 1H), 1.32 (d,  $J = 6.8$  Hz, 3H);  $^{13}\text{C-NMR}$  (101 MHz,  $\text{CDCl}_3$ )  $\delta$  149.68, 135.94, 133.16, 132.28, 130.98, 128.17, 127.94, 126.90, 126.32, 126.02, 125.34, 36.65, 34.35, 14.95;  $m/z = 243$  ( $\text{M}^+$ ).

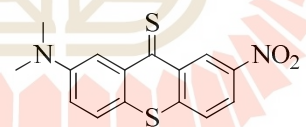
2-((4-(Dimethylamino)phenyl)thio)-5-nitrobenzoic acid (**17**)



4-(Dimethylamine)-benzenethiol (0.20 g, 1.30 mmol) was added to a solution of  $\text{NaHCO}_3$  (0.22 g, 2.60 mmol) in dry ethanol 10 ml. 2-Chloro-5-nitrobenzoic acid (0.26 g, 1.30 mmol) was then added into the mixture. The reaction mixture was heated under reflux for 24 h under nitrogen atmosphere. After cooling at room temperature, 10% aq. HCl solution (15 ml) was added after which a precipitate was collected by filtration, yielding crude (0.32 g, 77%);  $^1\text{H-NMR}$  (400 MHz,  $\text{CDCl}_3$ )  $\delta$  8.91 (d,  $J = 2.6$  Hz, 1H), 8.04 (dd,  $J = 9.1, 2.6$  Hz, 1H), 7.37 (d,  $J = 8.9$  Hz, 2H), 6.93 (d,  $J = 9.1$  Hz, 1H), 6.78 (d,  $J = 8.9$  Hz, 2H), 3.05 (s, 6H); no  $^{13}\text{C-NMR}$  data available due to low solubility; LCMS:  $m/z = 319$  ( $\text{M}^+$ ).

2-(Dimethylamino)-7-nitro-9H-thioxanthen-9-one (**18**)

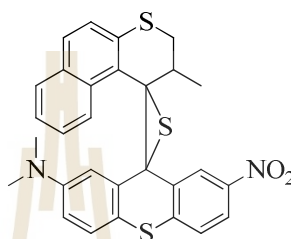
Compound **17** (0.20 g, 0.63 mmol) was added to PPA (5 ml) stirred at 70 °C. The temperature was then raised to 110 °C and stirring was continued for 3 h. The mixture was poured onto ice (10 g) and allowed to hydrolyze overnight. Next the precipitate was filtered and washed with water (5 ml), concentrated NaHCO<sub>3</sub> (5 ml) and ethanol (10 ml). The red solid was dried under vacuum, yielding **18** (0.18 g, 96%); <sup>1</sup>H-NMR (400 MHz, CDCl<sub>3</sub>) δ 9.52-9.40 (m, 1H), 8.34 (dd, *J* = 8.9, 3.0 Hz, 1H), 7.83 (d, *J* = 3.0 Hz, 1H), 7.74-7.64 (m, 1H), 7.47 (d, *J* = 8.9 Hz, 1H), 7.16 (dd, *J* = 8.9, 3.0 Hz, 1H), 3.09 (s, 6H); no <sup>13</sup>C-NMR data available due to low solubility; LCMS: *m/z* = 301 (M<sup>+</sup>).

2-(Dimethylamino)-7-nitro-9H-thioxanthene-9-thione (**19**)

Under nitrogen atmosphere, the starting material **18** (0.10 g, 0.33 mmol) was placed in a three neck round bottom flask and the compound dissolved in dehydrated toluene (10 ml). Lawesson's reagent (0.27 g, 0.66 mmol) was previously dried in additional funnel for 1 h and then the reaction mixture was stirred at room temperature for 15 min and then for 4 h at 90 °C. The deep green reaction mixture was filtered, and the residues were washed with CH<sub>2</sub>Cl<sub>2</sub> until the solvent was no longer green. The crude product obtained after evaporation of all volatiles and finally recrystallized from dichloromethane-methanol to yield dark green solid of the

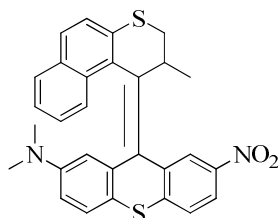
thioketone **19** (0.08 g, 79%);  $^1\text{H-NMR}$  (400 MHz,  $\text{CDCl}_3$ )  $\delta$  9.90-9.73 (m, 1H), 8.30 (dd,  $J = 8.9, 2.5$  Hz, 1H), 8.24 (d,  $J = 2.9$  Hz, 1H), 7.69 (dd,  $J = 8.9, 0.4$  Hz, 1H), 7.49 (d,  $J = 8.9$  Hz, 1H), 7.30-7.25 (m, 1H), 3.11 (s, 6H); no  $^{13}\text{C-NMR}$  data available due to low solubility; LCMS:  $m/z = 317$  ( $\text{M}^+$ ).

#### Episulfide (**20**)



Under nitrogen atmosphere, a stirred solution of hydrazone **16** (0.50 g, 0.82 mmol) in dry  $\text{CH}_2\text{Cl}_2$  (15 ml) was cooled to  $-20$  °C, were upon  $\text{MgSO}_4$  (0.35 g),  $\text{Ag}_2\text{O}$  (0.38 g, 1.64 mmol) and saturated solution of  $\text{KOH}$  in  $\text{MeOH}$  (1 ml). After the solution turned deep red stirring for 1 h at  $0$  °C, it was filtered into another ice cooled bulb ( $-20$  °C) and the remaining residue was washed by cold  $\text{CH}_2\text{Cl}_2$ . To the deep red solution was added with a solution of thioketone **19** (0.26 g, 0.82 mmol) in  $\text{CH}_2\text{Cl}_2$  solution. Nitrogen evolution was observed and the red color of the solution slowly disappeared. The reaction mixture was stirred at  $-20$  °C for 3 h and then allowed to room temperature overnight. All volatiles were removed under reduced pressure to obtain the crude product. The episulfide **20** was obtained without further purification (0.23 g).

(*E*),(*Z*)-*N,N*-Dimethyl-9-(2-methyl-2,3-dihydro-1H-benzo[*f*]thiochromen-1-ylidene)-7-nitro-9H-thioxanthen-2-amine (**21**)



Copper powder (approx. 0.30 g) and triphenylphosphine 0.30 g was added to a stirred solution of episulfide **20** (0.23 g, 0.44 mmol) in 30 ml *p*-xylene under nitrogen atmosphere. The mixture was heated at reflux for 3 days and then allowed to cool to room temperature. The brown copper residue was removed by silica gel filtration and washed with CH<sub>2</sub>Cl<sub>2</sub>. After removed all volatile solvents under reduced pressure, the crude was purified by column chromatography using dichloromethane-hexane as eluent to obtain the desired product (0.14 g, overall yield 32%); Cis-isomer **21**: <sup>1</sup>H-NMR (400 MHz, CDCl<sub>3</sub>) δ 8.43 (d, *J* = 2.4 Hz, 1H), 8.12 (dd, *J* = 8.6, 2.4 Hz, 1H), 7.70 (d, *J* = 8.6 Hz, 1H), 7.61 (d, *J* = 8.6 Hz, 1H), 7.55 (d, *J* = 7.8 Hz, 1H), 7.49 (d, *J* = 8.3 Hz, 1H), 7.40 (d, *J* = 8.6 Hz, 1H), 7.13 (t, *J* = 7.4 Hz, 1H), 7.08 (d, *J* = 8.7 Hz, 1H), 7.01 (d, *J* = 8.3 Hz, 1H), 6.19 (dd, *J* = 8.7, 2.8 Hz, 1H), 5.78 (d, *J* = 2.7 Hz, 1H), 4.03-3.92 (m, 1H), 3.76 (dd, *J* = 11.4, 7.4 Hz, 1H), 3.10 (dd, *J* = 11.0, 3.8 Hz, 1H), 2.26 (s, 6H), 0.80 (d, *J* = 6.7 Hz, 3H); Trans-isomer **21**: <sup>1</sup>H-NMR (400 MHz, CDCl<sub>3</sub>) δ 7.74-7.68 (m, 3H), 7.58 (d, *J* = 8.6 Hz, 1H), 7.55-7.45 (m, 3H), 7.14 (d, *J* = 2.4 Hz, 1H), 7.06 (t, *J* = 7.1 Hz, 1H), 7.04 (s, 1H), 6.97 (d, *J* = 2.7 Hz, 1H), 6.72 (dd, *J* = 8.7, 2.7 Hz, 1H), 4.30 (td, *J* = 7.1, 3.2 Hz, 1H), 3.70 (dd, *J* = 11.3, 7.4 Hz, 1H), 3.11 (dd, *J* = 11.3, 3.1 Hz, 1H), 3.03 (s, 6H), 0.84 (d, *J* = 6.8 Hz, 3H); LCMS: *m/z* = 528 (M<sup>+</sup>).

### 3.5 Results and Discussion

#### 3.5.1 Synthesis

The synthesis of the upper part of the target molecule, with the hydrazone functionality needed for the Barton-Kellogg reaction, has been performed using a three step sequence as shown followed. The first is a Michael addition of the naphthalenethiol with methacrylonitrile in the present of Triton B as base to obtain 2-methyl-3-(naphthalen-2-ylthio)propanenitrile (**14**) in 71% yield (Figure 3.11). The compound **14** is then allowed to react further with acidic condition of poly phosphoric acid (PPA) to obtain the ring-closed product 2-methyl-2,3-dihydro-1H-benzo[f]thiochromen-1-one (**15**) in 95% yield. The last step, hydrazone **16** was then synthesized from the ketone **15** by heating at reflux overnight in a mixture of hydrazine monohydrate ( $\text{NH}_2\text{NH}_2 \cdot \text{H}_2\text{O}$ ) as nucleophile in ethanol solution in 31% yield.

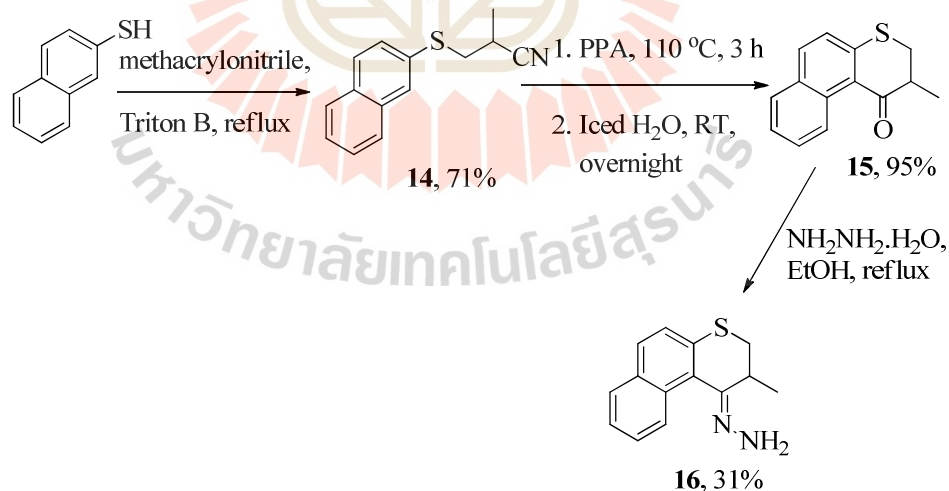


**Figure 3.11** The conditions and reagents to synthesize molecule **16**.

The chemical structure of hydrazone **16** was confirmed by  $^1\text{H-NMR}$  analysis (Figure 3.12). The  $^1\text{H-NMR}$  spectrum of intermediate **16** shows high field shifted at aromatic region comparing those with **15** and still have 6H at this region, corresponding to strong electron donating group of  $=\text{N-NH}_2$  substituted effect.

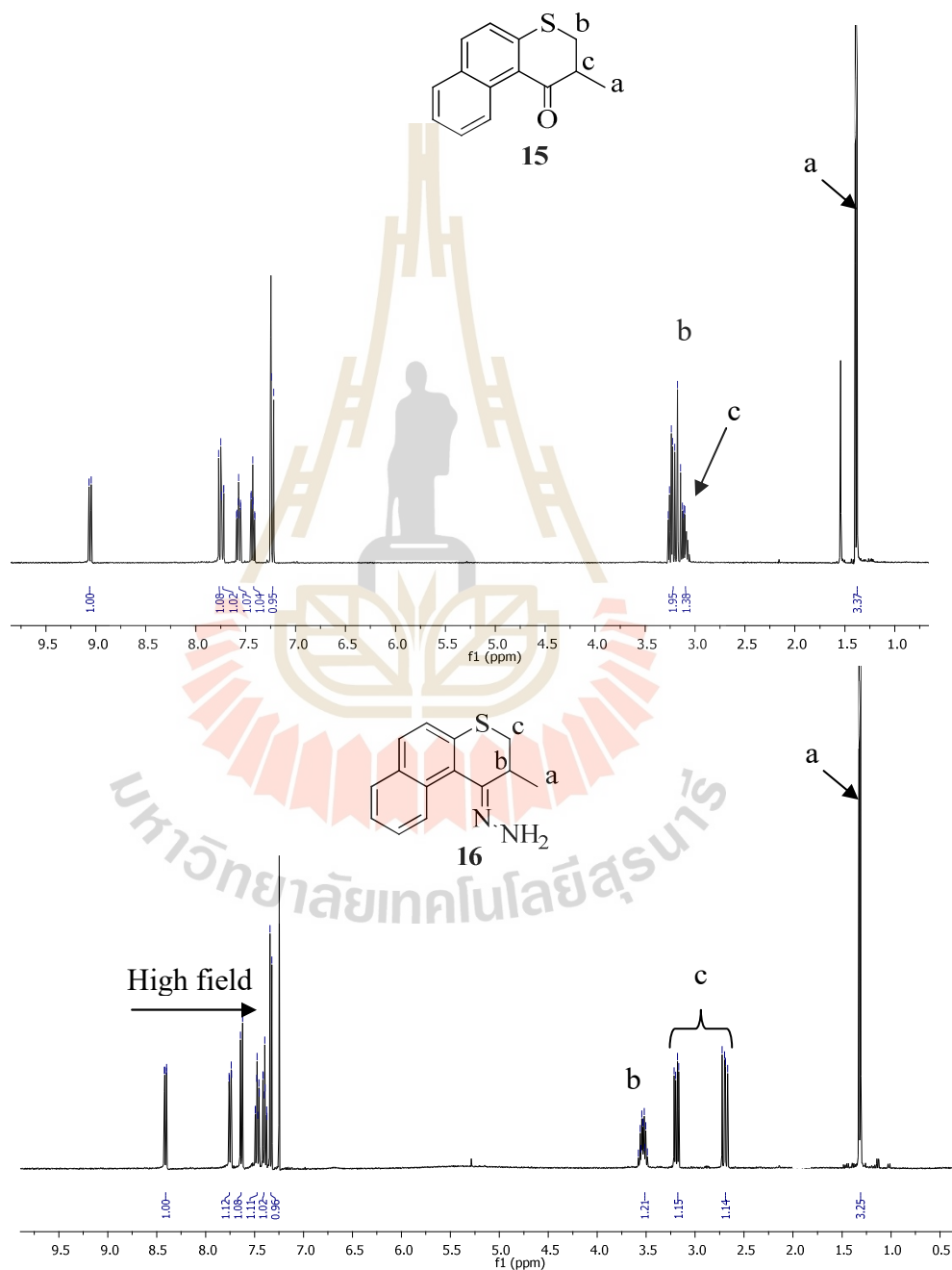


**Figure 3.12** The  $^1\text{H-NMR}$  spectra in  $\text{CDCl}_3$  of molecules **15** and **16**.

The synthesis of the thioketone **19** required for the lower half is quite complicated, in Figure 3.13. The initial synthesis of the molecule was started with 4-(dimethylamino) benzenethiol react with 2-chloro-5-nitro benzoic acid in the present of NaHCO<sub>3</sub> as base in ethanol as solvent under atmospheric nitrogen pressure to obtain 2-((4-(dimethylamino)phenyl)thio)-5-nitrobenzoic acid (**17**) in 77% yield. A ring closure to ketone **18** using a Friedel-Crafts reaction was performed by treating the acid **17** with PPA at 110 °C for 3 h to give 2-(dimethylamino)-7-nitro-9H-thioxanthen-9-one (**18**) in 96% yield. Finally, the ketone **18** was converted by reaction with Lawesson's reagent in refluxing toluene to give the thioketone, 2-(dimethylamino)-7-nitro-9H-thioxanthen-9-thione (**19**) in 79% yield.

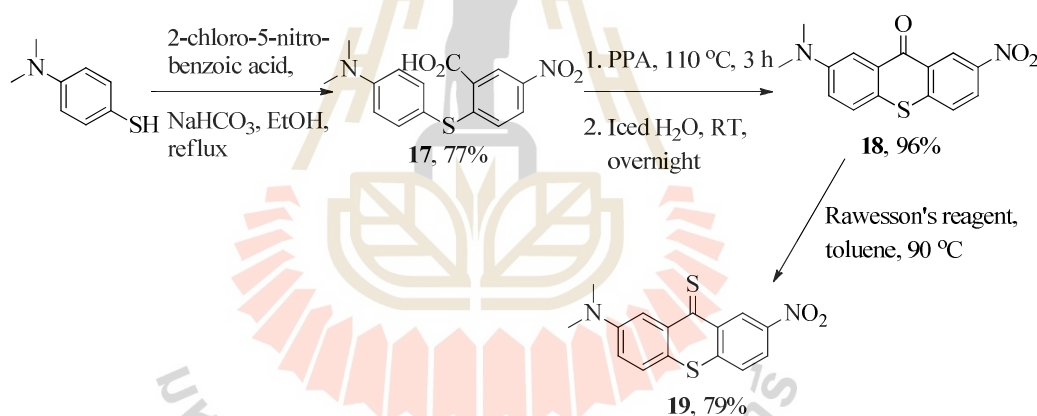


**Figure 3.13** The synthesis of lower half thioketone **19**.

The molecular structure of **19** was confirmed with <sup>1</sup>H-NMR analysis and LCMS. The <sup>1</sup>H-NMR spectrum (Figure 3.14) shows a singlet signal at 3.05 ppm (6H) assigning as dimethylamine substituent and singlet signal at 9.90 ppm (1H) and 8.24 (1H) assigning as proton **c** and **b** proton positions. The <sup>1</sup>H-NMR spectrum of **19** was observed 6H at aromatic region which are similar <sup>1</sup>H-NMR signal to **18**. However, the

proton signals are lower field shifted causing from stronger electron withdrawing group of sulfur substituted of **19**.

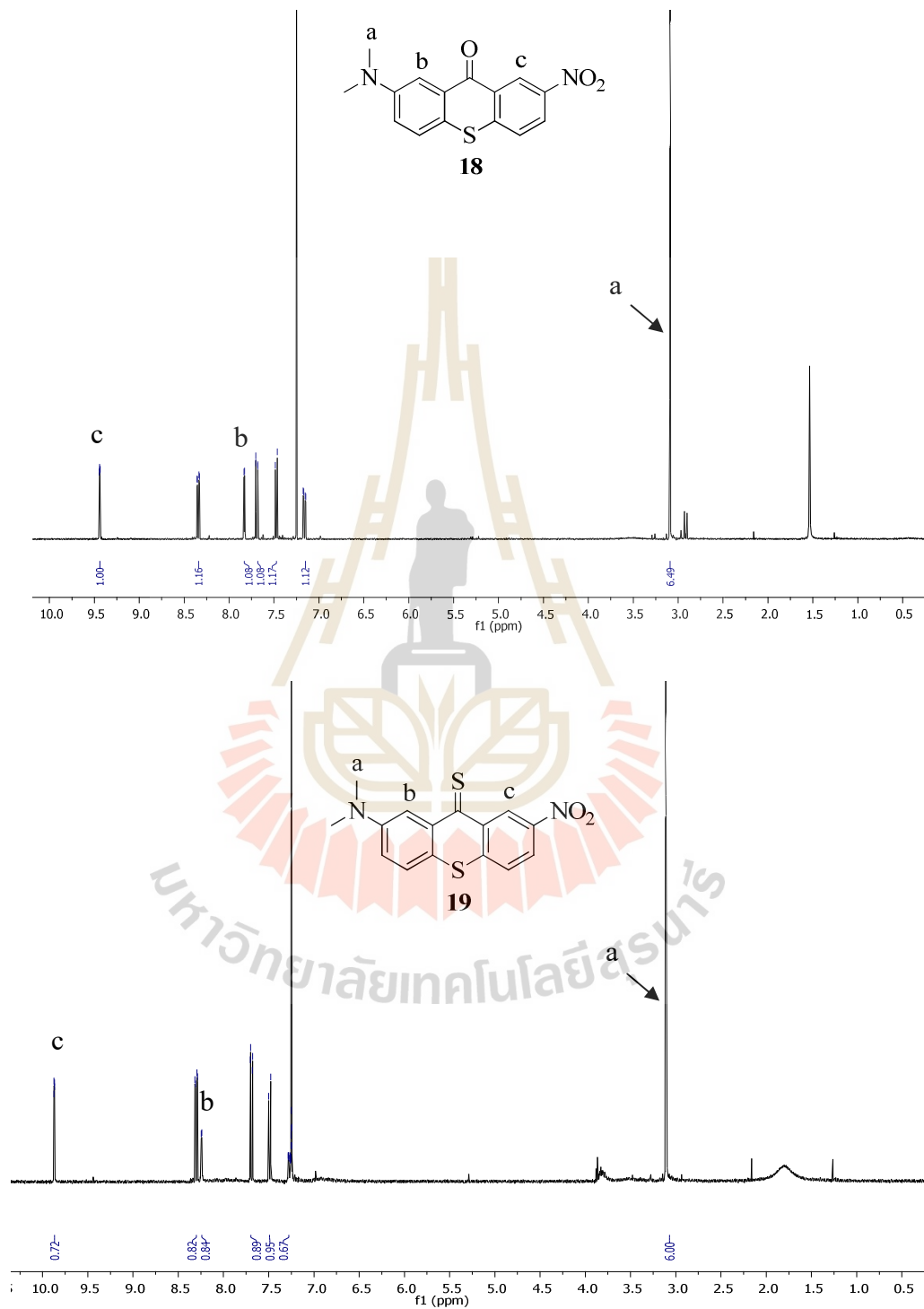


**Figure 3.14** The <sup>1</sup>H-NMR spectra in CDCl<sub>3</sub> of molecules **18** and **19**.

With efficient methodology to synthesize both the upper half **16** and lower half **19**, both fragments are coupled using the Barton-Kellogg reaction (Figure 3.15). The hydrazone **16** was oxidized using  $\text{Ag}_2\text{O}$  in combination with  $\text{anh. MgSO}_4$  and a saturated solution of  $\text{KOH}$  as base in methanol. It has to be mentioned that the outcome of this reaction from many researchers is highly unpredictable and often proceeds poorly. The deeply-red colored solution of the diazo compound was allowed to react in situ with the thioketone **19**. The intermediate thiadiazoline was not observed as product, undoubtedly because during the reaction nitrogen evolution can be observed leading to the episulfide **20** in 23% yield. The episulfide can then easily be converted by reaction with triphenyl phosphine (TPP) and copper powder to afford the alkene **21** in an isolated overall yield of 32%.

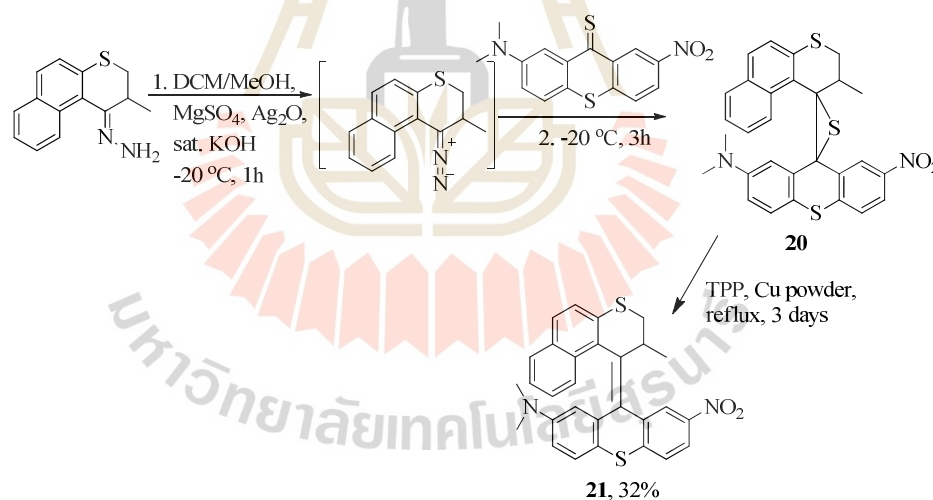


**Figure 3.15** Formation of the central double bond and the synthesis of **21**.

The reaction mechanism of Barton-Kellogg reaction was presented in Figure 3.16. The diazo compound **16** reacts with the thioketone **19** in a 1,3-dipolar cycloaddition to a thiadiazine. This intermediate is unstable and though nitrogen gas expulsion and formation of an intermediate thiocarbonyl ylide it forms a stable

episulfide. Triphenylphosphine opens the three-member ring and then forms a sulfaphosphatane in a manner similar to the Wittig reaction. In the final step, triphenylphosphine sulfide is expelled liberating the alkene.

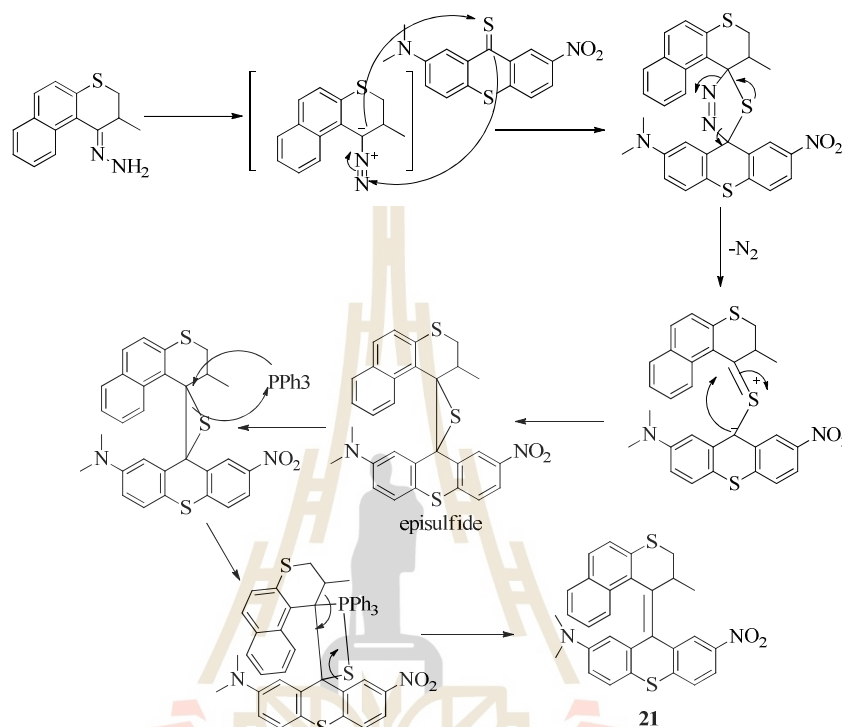


**Figure 3.16** The propose mechanism of Barton-Kellogg reaction of **21**.

The  $^1H$ -NMR spectra of Cis and Trans-isomers **21** shows a similar signal except proton signal of *N*-methyl substituent, shown in Figure 3.17. The singlet peak at chemical shift 3.49 ppm (6H) assigned as protons of dimethylamine moiety for Cis-isomer **21**, whereas the trans-isomer **21** shows chemical shifted 2.36 ppm (6H), due to shielding by naphthyl moiety in the upper half of the molecule. The doublet observed for the methyl substituent in the upper half of the molecule was shifted down-field from 0.85 ppm for Trans **21** to 0.80 ppm for Cis **21** which is caused be deshielding effect of the lower half aryl moiety, indicating an equatorial orientation.

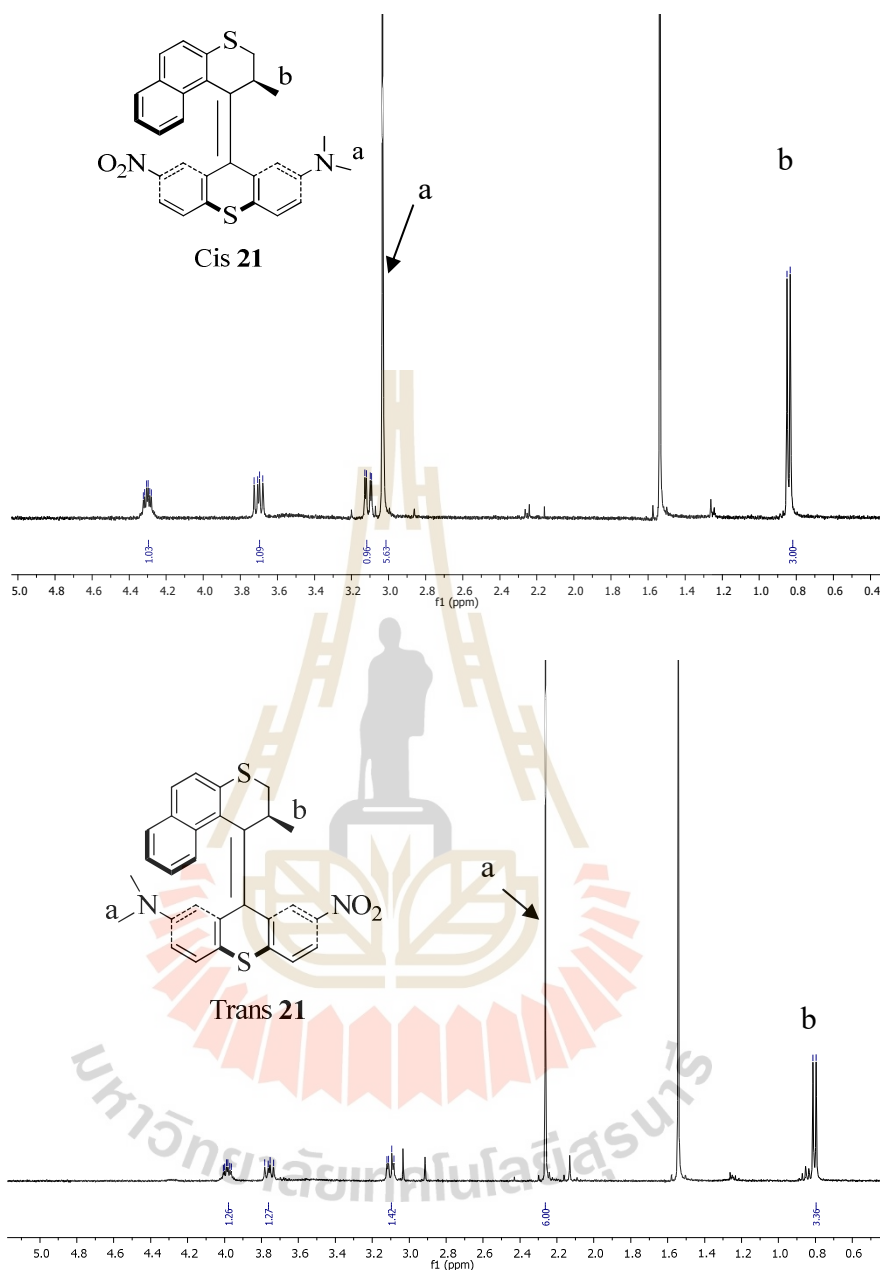


**Figure 3.18**  $^1\text{H-NMR}$  compared between *Cis* (top) and *Trans* isomer **21** (bottom).

After separation process of *Cis*- and *Trans*-isomers **21** using silica gel column chromatography techniques, the mixed (*P*), (*M*)-*Cis* and (*P*), (*M*)-*Trans* were also separated with high performance liquid chromatography (HPLC) technique.

Resolution was performed on a Chiralcel OD-H HPLC column ( $5\mu\text{m}$ ;  $20\text{ mm}\phi\times 250\text{ mm}$ ) for preparative separation using n-hexane : *tert*-butyl ethyl ether (65 : 35 ratios) for Cis-**21** (elution times: 24.62 min for (*M*)-Cis **21** and 25.65 min for (*P*)-Cis **21**). For Trans-**21** was used as the same eluent on the same chiral column to give (*M*)-Trans-**21** after 2.73 min and (*P*)-Trans **21** (again not used for the experiments) after 3.06 min (Figure 3.18).

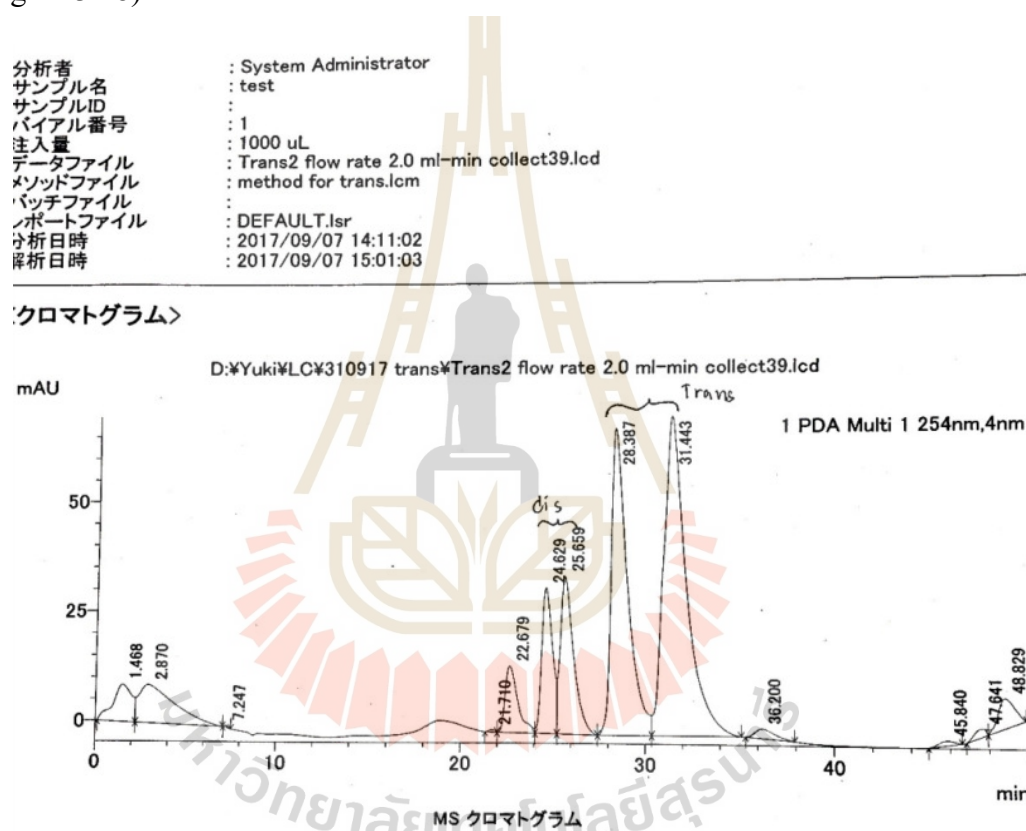


**Figure 3.18** The HPLC spectra of Cis- and Trans-isomers **21**.

### 3.5.2 Optical properties

The (*M*) to (*P*) reversal of helicity is readily observed using CD spectroscopy. A photostationary state with *M*, *P*-Trans was also investigated the helical structure in chloroform solution of the switching system (Figure 3.19). As

expected the spectral features of stable *M*-Trans **21** are similar to those of *P*-Trans **21** isomers, a clear helix inversion of both compounds was visible in the CD spectrum.

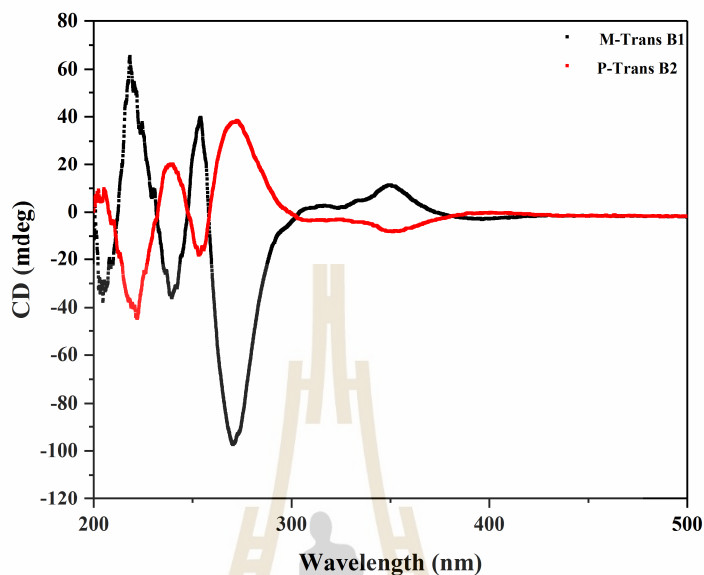


**Figure 3.19** CD spectra of *M*-Trans and *P*-Trans **21** in  $\text{CHCl}_3$  solution.

### 3.6 Conclusions

The newly designed donor-acceptor based on over crowned alkenes (*P*, *M*-Cis and *P*, *M*-Trans **21**) applied as organic spin filter for the magnetoresistance devices were successfully synthesized. The target molecules were also characterized by  $^1\text{H}$ -NMR,  $^{13}\text{C}$ -NMR as well as LCMS techniques. The helical character of chiral molecule, (*P*), (*M*)-Trans **21**, was also confirmed using circular dichroism (CD) technique. Moreover, the designed molecules exhibited an absorption band cover UV and visible region as expected. This is the initially proved to be the most efficient molecular switch based on the donor-acceptor sterically over crowned alkenes.

### 3.7 References

- Andrés, A., Poeylout, P. and Ernesto, G.M. (2005). Thionation of bicyclic  $\beta$ -lactam compounds by Lawesson's reagent. **ARKIVOC (xii)**. 282-294.
- Ben, L.F., Richard, A., Delden, V., Nagatoshi, K. and Edzard, M.G. (2000). Chiroptical molecular switches. **Chemistry Review**. 100: 1789-1816.
- Braun, D. and Heeger, A.J. (1991). Visible light emission from semiconducting polymer diodes. **Applied Physics Letters**. 58: 1982-1984.
- Delden, V. and Andreas, R. (2002). A donor-acceptor substituted molecular motor: unidirectional rotation driven by visible light. **Controlling Molecular Chirality and Motion Groningen: s.n.** 157-178.
- Delden, V., Andreas, R. and Delden, R.A. (2002). Controlling molecular chirality and motion. **Groningen: s.n.** 1: 46-80.
- Delden, V., Richard A.V., Hurenkamp, J.H. and Feringa, B.L. (2003). Photochemical and thermal isomerization processes of a chiral auxiliary based donor-acceptor substituted chiroptical molecular switch: convergent synthesis, improved resolution and switching properties. **European Journal of Chemistry**. 9: 2845-2853.
- Dor, O.B., Yochelis, S., Mathew, P.S., Naaman, R. and Paltiel, Y. (2013). A chiral-based magnetic memory device without a permanent magnet. **Nature communications**. 4: 1-6.
- Jager, F.W., Johannes, C., Ben, D.J., Lange, D., Huck, N.P.M., Meetsma, A. and Ben, L.F. (1995). A highly stereoselective optical switching process based on donor-acceptor substituted dissymmetric alkenes. **Angewandte Chemie International Edition**. 34: 348-350.

- Kiran, V., Mathew, S.P., Cohen, S.R., Delgado, I.H., Lacour, J. and Naaman, R. (2016). Helicenes-a new class of organic spin filter. **Advanced Materials**. 28: 1957-1962.
- Koumura, N., Geertsema, E.M., Marc, B., Gelder, V., Meetsma, A. and Feringa, B.L. (2002). Second generation light-driven molecular motors. unidirectional rotation controlled by a single stereogenic center with near-perfect photoequilibria and acceleration of the speed of rotation by structural modification. **Journal American Chemistry Society**. 124: 5037-5051.
- Leeuwen, V.T., Pol, J., Roke, D., Wezenberg, J.S. and Feringa, L.B. (2017). Visible-light excitation of a molecular motor with an extended aromatic core. **Organic Letters**. 19: 1402-1405.
- Michaeli, K., Varade, V., Naaman, R. and Waldeck, H.D. (2017). A new approach towards spintronics-spintronics with no magnets. **Journal of Physics: Condensed Matter**. 29: 103002.
- Varade, V., Markus, T., Vankayala, K., Friedman, N. Sheves, M. Waldeck, H.D. and Naaman, R. (2018). Bacteriorhodopsin based non-magnetic spin filters for biomolecular spintronics. **Physical Chemistry Chemical Physics**. 20: 1091-1097.
- Waser, R. (2003). Nanoelectronics and information technology-advanced electronic materials and novel devices. **Wiley-VCH; Weinheim**. 917.
- Wiel, T. and Matthijs, D. (2004). Surface-bound molecular motors. **Basic Molecular Devices Groningen: s.n.** 240-299.

## CURRICULUM VITAE

<b>Name</b>	Miss Yuranan Thathong
<b>Date of birth</b>	11 september 1988,
<b>Place of birth</b>	Amnatcharoen province, Thailand
<b>Education</b>	2007 - 2011, Bachelor of Science Chemistry, Ubon Ratchathani University 2011 - 2013, Master of Science Chemistry, Ubon Ratchathani University 2013-2017, Ph.D. student of Science Chemistry, Suranaree University of Technology
<b>Grants and Fellowships</b>	Science Achievement Scholarship of- Thailand, M.Sc.-Ph.D. programs.
<b>Presentations</b>	The 12 <sup>th</sup> Science and Technology Conference for Youths, "Synthesis and characterization of self-hosting blue emitting TADF materials based on carbazole dendronized diphenylsulfone for organic light emitting diode", BITEC, Bangkok, Thailand.